# A Cryogenic Trap for Neutral Atoms

Thesis by

Richard A. Boyd

In Partial Fulfillment of the Requirements
for the Degree of
Doctor of Philosophy

California Institute of Technology
Pasadena, California

1997
(Submitted May 28, 1997)

# Acknowledgements

I would like to thank my advisor, Ken Libbrecht, for the confidence he has shown in me over the years and for giving me the chance to work on such an interesting and unique project. The two other members of our group deserve special mention. First, Phil Willems was instrumental in the development of cryotrapping and in the equipping of our laboratory. Most of what I know about experimental technique I learned from Phil. Josh Bliss provided invaluable lab assistance during the evaporative cooling and cross section experiments. Most of what I know about blasting monsters in Duke Nukem I learned from Josh. Even though he is an unreformable, die-hard C apologist, Josh still managed to teach me a great deal about computers. Thanks, guys, for everything.

Much of the machining for this project was expertly done by Richard Borup of Caltech; Richard taught me the fine art of machining as well. Jeff Kimble and his research group provided many loans of equipment that helped make these experiments a success. Also, a generous gift by Millard Jacobs of Pasadena made much of this research possible.

I have encountered a great many people during my years at Caltech, people who have made my time here interesting and enjoyable. Special thanks to John Arrington for all the Monty Python videos; Chris Bond for the impromptu lectures on aerodynamics and nearly every other topic; John Kitching for expert instruction on semiconductor lasers; John Iannelli and Randy Salvatore for Wall Street advice (whatever happened to dig pd?); Nick Glumac, Pradeep Guduru, Rajesh Kedia, Tasso Lappas, Aseem Mehta, and Joe Sivo for making MJ House so much fun; and to Sima Setayeshgar for all the conversations on physics and everything else.

Finally, I would like to dedicate this thesis to my mother, who has always been there for me, no matter what.

# Abstract

A cryogenic system for the trapping and cooling of neutral atoms is described. The system uses superconducting coils inside a trapping chamber cooled to liquid helium temperatures. The cryogenic nature of the system allows the production of extremely long-lived traps at high field gradients and curvatures. At the highest field gradients, evidence for discrete jumps in the trap fluorescence is presented; these jumps are shown to be due to single atoms entering and leaving the trap. The stability of high field gradient traps is studied, and a newly identified loss mechanism, stochastic diffusion, is shown to be the dominant loss mechanism for such traps. Finally, evidence for evaporative cooling of cesium is presented, and an upper bound to a cross section critical to the evaporation process is obtained.

# Contents

# List of Figures

# Chapter 1 General Introduction

## 1.1 Introduction

This thesis describes a new system for the trapping and cooling of neutral atoms. The critical components of this system are cryogenic, and its atom traps are formed in a chamber cooled to liquid helium temperatures. The cryogenic environment allows the production of an excellent vacuum via cryopumping and the generation of high field gradients with superconducting coils. These two facts alone give it a power and flexibility unavailable to other conventional, room-temperature trapping systems.

This apparatus is only a few years old, but already it has amassed an impressive list of achievements. It has demonstrated the longest-lived magnetostatic traps to date, the lowest background pressures ($\approx 10^{-13}$ torr), and the highest field gradients (up to 3 kG $\text{cm}^{-1}$). It has allowed the direct, real-time observation of *single* cesium atoms moving around in a strong quadrupole field. Also, the definitive study of MOT stability at high field gradients has been performed with it, and a new trap loss mechanism for such traps has been identified and modeled. Finally, the process of evaporative cooling, which is required for attaining Bose-Einstein Condensation, has been demonstrated in this apparatus, and an upper bound to a critical collisional cross section has been obtained. This thesis will provide an overview of the apparatus and the details of these experiments.

The primary motivation for this undertaking has been the desire to have a system capable of achieving Bose-Einstein Condensation (BEC) in a gas of cesium. Even though BEC has been seen in rubidium [1] and sodium [2], a cesium condensate could provide an opportunity to observe new phenomena. The $|F = 4,\ m_F = 4\rangle$ state of cesium is believed to have a large, negative scattering length [3]. As will be discussed in chapter 7, there is currently no clear consensus on how a gas of negative scattering length atoms should behave under conditions of quantum degeneracy. Another state, $|F = 3,\ m_F = -3\rangle$, has been predicted to have a magnetically-tunable scattering length with a pronounced resonance structure [4]. One could thus imagine the possibility of producing a cesium condensate, varying the ambient field, and observing its behavior as the scattering length of its atoms changes magnitude and perhaps sign.

While the cryogenic aspects of this system provide many advantages in terms of vacuum quality and magnetic field strength, they also introduce a host of complications not found in other trapping systems. The major problems encountered during the course of this work will be described in detail in the pages that follow. It is believed that the major obstacles have been overcome, and that a next generation version of this apparatus should be capable of evaporative cooling well into the regime of quantum degeneracy.

## 1.2 Thesis Summary

The second chapter of this thesis provides an overview of the basics of laser cooling and trapping. Doppler cooling and the magneto-optical trap are discussed, and brief mention is made of two important sub-doppler cooling mechanisms. The chapter ends with a discussion of the two magnetic field configurations used for the experiments of this thesis.

The third chapter is an introduction to the field of cryotrapping. The major problems with room-temperature trapping systems are discussed, and it is shown how a cryogenic system offers distinct advantages with respect to these problems. The major design considerations for a cryogenic system are reviewed, and emphasis is given to the trade-offs made for the current system. The major components of the cryotrapping system are then discussed in detail.

Chapter four provides an overview of the laser and optical systems of our apparatus. A diagram of the main components of the optical layout is provided, and the critical laser systems are explained. At the end of the chapter, methods used for determining the atom number, density, and temperature of cesium traps are provided.

Chapter five gives an overview of several quadrupole trap experiments. Our lifetime data is presented, along with data confirming the existence of traps containing a single cesium atom. The text of a paper describing the results of our MOT stability work is included as an appendix to the chapter.

Chapter six describes our measurement of an upper bound to a particularly important cesium cross section. The theory behind the measurement is provided, and our experimental procedure is described in detail. The results of our measurement are presented, along with a discussion of evidence for a lack of higher-order partial waves in the scattering.

Chapter seven is an introduction to the theory of evaporative cooling. The major assumptions of the model are discussed first, and then a derivation of the major results is presented. Simulations are used to illustrate the major points of the theory.

The eighth and final chapter presents our experimental efforts in evaporative cooling. All steps in our evaporation procedure are discussed, and our reasons for choosing each different procedure are given, along with our results. The thesis concludes with thoughts on future directions and improvements for this apparatus.

# Chapter 2 Laser Cooling and Trapping

## 2.1 Introduction

A circularly polarized photon carries an amount of angular momentum equal to $\hbar$. In the late 1940's, Alfred Kastler showed that this angular momentum could be transferred to atoms in a gas, thereby causing the gas to become magnetized [5]. Kastler's investigations created the field of optical pumping, and he sparked a revolution in mankind's understanding of basic atom-photon interactions.

It was not fully recognized until the mid 1970's, though, that the *linear* momentum carried by photons could also be used to manipulate atoms. In 1975, Hänsch and Schawlow proposed the idea of *laser cooling*, or of using resonant momentum exchange between atoms and photons to control the kinetic temperatures of the atoms [6]. Unfortunately, their proposal fell on deaf ears, and it was a decade before laser cooling was first experimentally realized by Chu and co-workers, in 1985 [7]. In the years since then, laser cooling techniques have become the foundation for most experiments in low temperature atomic physics.

In this chapter, an overview of the basic aspects of laser cooling and trapping will be presented. There are many reviews of this subject in the literature [8], so only the main results will be mentioned here.

## 2.2 Doppler Cooling

The basic idea behind laser cooling is easy to understand. If a two-level atom, moving with velocity $\boldsymbol{v}$, is irradiated by a single travelling wave of wavevector $\mathbf{k}$, the wave exerts a force on the atom equal to [9]:

$$\mathbf{F} = \hbar\mathbf{k}\frac{\Gamma}{2}\frac{\Omega^2/2}{\Omega^2/2 + \Gamma^2/4 + (\delta - \mathbf{k}\cdot\boldsymbol{v})^2}.$$

In this expression, $\Gamma$ is the natural linewidth of the transition (for the $F = 4$ to $F' = 5$ transition in cesium, $\Gamma = 2\pi \times 5.22$ MHz), $\delta = \omega_L - \omega_0$ is the detuning of the wave of frequency $\omega_L$ from resonance $\omega_0$, and the symbol $\Omega$ is the Rabi frequency:

$$\Omega^2 = \frac{I}{2I_{sat}}\Gamma^2,$$

expressed in terms of the wave intensity $I$ and the saturation intensity $I_{sat}$ for the particular transition. This force is based on absorption and spontaneous emission of photons and is known as the "scattering force," to be contrasted with stimulated dipole forces, which will not be considered here. For general laser cooling, atoms are not irradiated by single travelling waves, but by standing waves. In such cases the atoms are subjected to a force equal to the sum of the forces exerted by the two counterpropagating waves:

$$F = \hbar k \frac{\Gamma}{2} \left\{ \frac{\Omega^2/2}{\Omega^2/2 + \Gamma^2/4 + (\delta - kv)^2} - \frac{\Omega^2/2}{\Omega^2/2 + \Gamma^2/4 + (\delta + kv)^2} \right\}.$$

If this expression is expanded in the limit of low velocities, it will be found that the force provides damping in proportion to the velocity, or $F = -\alpha v$.

If such a force is used to cool a gas of atoms, the ultimate temperature attainable is known as the *doppler limit.* It must be stressed that the doppler limit is not zero, since the atoms continually absorb and spontaneously re-emit photons. This continual spontaneous emission causes the atoms to perform a random walk in momentum space, leading to a minimum temperature of [9]:

$$T_D = \frac{\hbar\Gamma}{2k_B}. \tag{2.1}$$

With three pairs of mutually perpendicular laser beams, a doppler cooling configuration known as "optical molasses" is created. This configuration provides velocity damping in all three dimensions, and it can be used to produce tenuous gases of atoms at temperatures near the doppler limit.

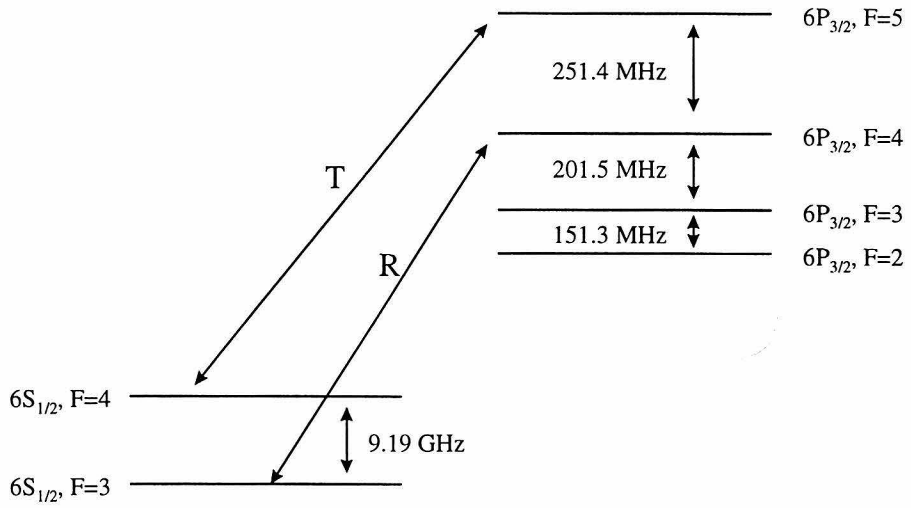

Figure 2.1: Hyperfine levels of cesium used for laser cooling.

### 2.2.1 Doppler Cooling of Cesium

To actually cool atoms by the method of Doppler cooling, some knowledge of the low-lying atomic energy levels is required. For the case of cesium, the hyperfine structure of the atom is of crucial importance. In figure 2.1 the level structure of some low-lying states of cesium is shown:

Cesium has a nuclear spin $I = 7/2$, giving rise to $F = 3$ and $F = 4$ ground state hyperfine levels. The transition usually used for cooling cesium is the $F = 4$ to $F^{'} = 5$ transition (denoted by T in the figure), since it is cycling and has the greatest oscillator strength of all the known Cesium lines. Even though the transition is cycling, there is a small amount of off-resonant excitation of the $4 \rightarrow 4^{'}$ transition. This creates an escape route for atoms to the lower $F = 3$ manifold. Once atoms land in the $F = 3$ manifold they are 9.2 GHz out of resonance with the cycling transition and experience no further excitation.

To prevent the off-resonant excitation from happening, an additional beam of "repumping" light is added to the standing wave configuration. The repumper is tuned to the $F = 3 \rightarrow F^{'} = 4$ transition, enabling decay to the $F = 4$ manifold and preventing further accumulation in $F = 3$.

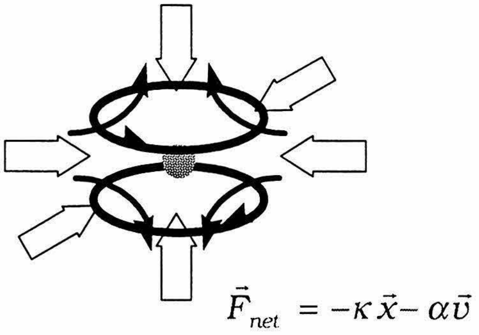

Figure 2.2: The magneto-optical trap.

## 2.3 The Magneto-Optical Trap

Optical molasses is effective for cooling small numbers of atoms. The lifetime of an optical molasses, though, is rather short, and is not really a trap at all, since it provides no restoring force to the atoms. Much stronger confinement can be provided if a restoring force is added to the trap. The most common restoring force results from the imposition of a quadrupole magnetic field in the molasses region. The combination of an optical molasses configuration of laser beams and a quadrupole field is known as a *magneto-optical trap.*

The magneto-optical trap (MOT) has been the workhorse of the laser cooling and atom trapping community. It was first suggested by Dalibard in 1987 [10] and experimentally realized by Raab *et al.* [11] a few months later. The MOT consists of a quadrupole magnetic field and 3 pairs of counterpropagating, mutually perpendicular, circularly polarized laser beams (figure 2.2). The field and the beams conspire to form a deep potential well, enabling large numbers of atoms ($10^8$ for 1 cm. beams) to be trapped at high densities ($10^{10}$ cm$^{-3}$) and low temperatures (125 $\mu$K for cesium). MOTs can be loaded either from beams, vapor cells, or other MOTs, giving the experimenter a wide range of flexibility and control over the trapping environment.

Even though the MOT has been in use for over a decade, many aspects of its behavior still evade precise theoretical description. MOTs are inherently many-body,

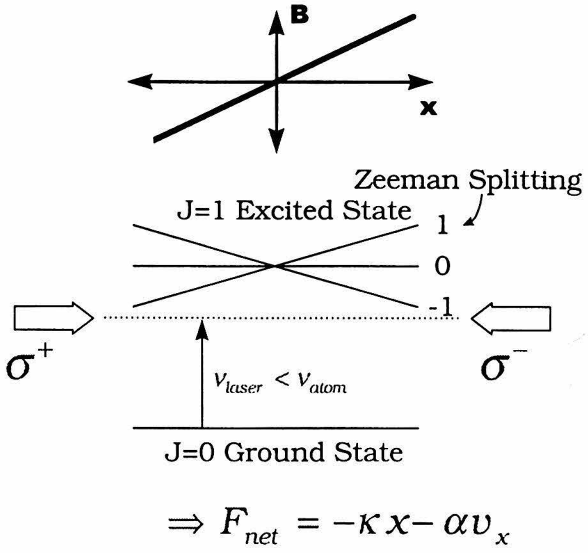

Figure 2.3: A one-dimensional MOT.

three-dimensional systems in which optical and interatomic forces are important. For typical atom numbers and densities, the MOT is not well-suited to any kind of perturbative treatment. Despite these difficulties, the basic forces at work in the MOT have been identified, and their effects on atoms have been studied in restricted one-dimensional models.

The most basic understanding of the MOT comes from the earliest models used to describe its behavior. At high atom numbers and densities, the Doppler model of the MOT provides a basic description. The simplest system to use for understanding this model of the MOT is that of a $J = 0$ to $J = 1$ transition, shown in figure 2.3. This figure depicts a one-dimensional model of the mot, with the symmetry axis of the quadrupole coils denoted by $z$, and with energy increasing towards the top of the figure. The lower line is the $J = 0$ level; it is horizontal since there is no Zeeman splitting for this level. The upper triplet of lines represent the energies of the three magnetic sublevels of the $J = 1$ state. The wavy lines represent the laser beams, which are detuned to the red of the zero-field $J = 1$ energy level by $\delta$.

In figure 2.3, the atom feels a force from both waves, resulting in a net force given by:

$$F = \hbar k \frac{\Gamma}{2} \left\{ \begin{array}{c} \frac{\Omega^2/2}{\Omega^2/2+\Gamma^2/4+(\delta-kv-g\mu B' z/\hbar)^2} - \\ \frac{\Omega^2/2}{\Omega^2/2+\Gamma^2/4+(\delta+kv+g\mu B' z/\hbar)^2} \end{array} \right\},$$

where the appropriate Zeeman shifts have been accounted for. If a small velocity, small Zeeman shift limit of this expression is taken, the resulting force can be expressed in the following form:

$$F \approx -\alpha v - \kappa z,$$

showing that the mot provides a restoring force, and that the atom undergoes damped harmonic motion. For typical MOTs, the motion is strongly overdamped.

Much has been learned about the venerable MOT in the decade since its discovery. Many different regimes of behavior have been mapped out, and it has been studied under wide and varied trapping conditions. For a good summary of state-of-the-art MOT research, see the excellent paper by Foot and his collaborators [12].

## 2.4 Sub-Doppler Cooling

The minimum temperature expected for atoms in a MOT, based on doppler cooling theory, is the doppler limit of equation 2.1. Soon after the first MOTs were formed, though, it became apparent that other cooling mechanisms were at work in the MOT, leading to temperatures much colder than what simple doppler theory would predict [13]. New theories were invented to describe the mysterious cooling mechanisms, with the major contributions coming from Chu and co-workers [14] and Dalibard and Cohen-Tannoudji [15]. Their theories all relied on the recognition that alkali atoms are not two-level systems, and that light shifts, optical pumping, and spatially varying polarization within traps play a major role. In this section, a brief summary of the main sub-Doppler mechanisms will be presented, since a successful sub-doppler cooling stage is essential for evaporative cooling. For more details on sub-doppler theory, consult the fundamental works of Cohen-Tannoudji [15, 16].

### 2.4.1 Sisyphyus Cooling

A generic example of this cooling mechanism is that of a $J = 1/2$ atom travelling in the field of two counterpropagating laser beams with orthogonal linear polarization. If the atom is assumed to have a $J = 3/2$ excited state (for simplicity), there are two magnetic sublevels in the ground state and four in the excited state. If there is a significant population in either of the ground state sublevels, then the external field could optically pump the atom in various ways depending on the field polarization.

The net polarization of the field in this configuration changes every 1/8 wavelength from linear, to $\sigma^-$, to linear, to $\sigma^+$, etc. This means that the ground state sublevels have populations that depend strongly on the location of the atom within the field. As the atom moves through the field, the populations in the ground state shift around according to the local polarization.

The key point to consider here is that there is a time $\tau_p$ between optical pumping cycles, which affects the optical pumping in the presence of atomic motion. These cycles occur at a rate that, at low laser intensity, is proportional to the intensity [15]. If the atom should be moving through the field at a speed such that it travels a distance $\lambda/4$ in the time $\tau_p$, then it could find itself in a situation of repeatedly climbing light-shift induced potential hills, even though it is being pumped from one ground state sublevel to another. The uphill struggle against the potential wells gives rise to an effective frictional force that cools the atoms far below the Doppler limit [15].

### 2.4.2 Induced Orientation

As an example of this cooling mechanism [15], consider an atom at rest in a standing wave formed by two counterpropagating laser beams, one with $\sigma^+$ polarization, and the other with $\sigma^-$ polarization (as would be the case in a MOT). The net polarization of the electric field in this case is linear, but it rotates along the axis of the beams, tracing out a helix in space. The pitch of the helix is equal to $\lambda$, the laser wavelength. The field intensity is constant for this configuration, precluding the existence of any dipole forces [15].

Suppose the atom to be at rest at a point where the polarization is entirely along the $y$ axis. This $\pi$ optical pumping will establish a symmetrical population distribution among the ground-state sublevels, which are eigenstates of $J_y$. In general, these sublevels will have unequal light shifts, but no net population imbalance along $z$ ( $< J_z >= 0$ ). If the atom is moved and placed at rest at another position, the same population distribution and light shifts will apply, but to states that are eigenstates of $\mathbf{J}$ projected along the local direction of the polarization. These states, when expanded in the original $J_y$ basis, introduce couplings amongst the various eigenstates of the original basis. If an expectation value of $J_z$ is taken, it is found that $\langle J_z \rangle$ is no longer zero, and that the populations of the ground state stretched states are unequal. This is a motion-induced atomic orientation in the ground state. The unequal populations cause imbalances in the rates of absorption from the laser beams, giving rise to a net frictional force. For further details, consult the fundamental paper of Dalibard and Cohen-Tannoudji [15].

## 2.5 Magnetic Field Configurations

In this section, an overview of the magnetic field configurations used for the experiments in this thesis will be given. First to be discussed will be the quadrupole field, which is the trapping field used in the MOT. After this, a discussion of our Yin-Yang trapping coils will be provided. The Yin-Yang trap is a variant of the Ioffe trap, a field configuration that provides radial and axial confinement with a nonzero bias at the center.

### 2.5.1 Quadrupole Field

The quadrupole field configuration is formed from two coils, separated by a distance A, carrying opposing currents. The $z$-component of the magnetic field can be easily calculated to be

$$B_z(0,0,z) = \frac{\mu_0 I R^2}{2}\left\{\frac{1}{\left[(A-z)^2+R^2\right]^{3/2}} - \frac{1}{\left[(A+z)^2+R^2\right]^{3/2}}\right\}. \tag{2.2}$$

If the field is expanded in powers of $z$, the lowest order terms in the expansion can be written as:

$$B_z(0,0,z) \approx c_1 z + c_3 z^3 + \cdots,$$

with

$$\begin{aligned} c_1 &= \frac{\mu_0 I R^2}{2}\frac{6A}{(A^2+R^2)^{5/2}}, \\ c_3 &= \frac{5(4A^2-3R^2)}{6(A^2+R^2)^2}c_1. \end{aligned}$$

The cubic term in the expansion can be made to vanish if the separation $A$ is chosen so that $A = 0.87R$. This leaves a field with a linear gradient, the slope being given by coefficient $c_1$.

With the $z$-component of the field known, the radial components can be obtained from Maxwell's equations. From $\nabla \cdot \mathbf{B} = \mathbf{0}$ and the symmetry requirement of equal gradients along $x$ and $y$, we see that

$$\frac{\partial B_x}{\partial x} = \frac{\partial B_y}{\partial y} = -\frac{1}{2}\frac{\partial B_z}{\partial z}.$$

Thus, the quadrupole field increases linearly from the zero-valued minimum in all directions, the rate of increase in the $z$ direction being twice that in the radial direction. This means that traps formed with this field will take the shape of oblate ellipsoids..

### Finite-Size Effects

The above calculations assume that the two coils consist of ideal, infinitesimally thin wires. In an actual experiment, many turns of wire will be used to supply the needed field gradients. In our system, we carry this to an extreme with our superconducting coils. Our quadrupole pair consists of two coils of 1000 turns of wire each. If the

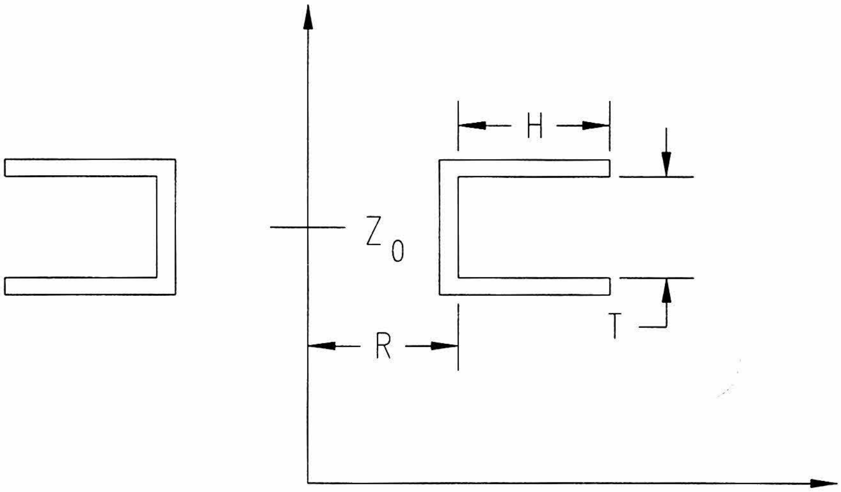

Figure 2.4: Thick coil parameters.

centroid of the windings is used for determining separations and radii, our coils have a radius $R$ of 0.955 cm and a separation $A$ equal to 0.827 cm. These values very nearly satisfy the $c_3 = 0$ condition mentioned above. The actual separation of these coils, though, was determined by considerations relevant to our Yin-Yang coil set, as will be discussed in the next section.

To investigate the influence of finite-size effects on our calculated fields, it is first necessary to find the field of a thick coil. Figure 2.4 depicts a thick coil with centroid at $z = z_0$, inner radius $R$, radial extent $H$, and thickness $T$. If the expression for $B_z(0,0,z)$ from equation 2.2 is integrated over $z$ and $r$, the following expression for the axial field due to a single thick coil is obtained [17]:

$$B_z(0,0,z) = \frac{\mu_0 NIR}{2TH}\left[x_2 \ln\left(\frac{x_2}{x_1}\frac{1+\sqrt{1+x_1^2}}{1+\sqrt{1+x_2^2}}\right) - x_4 \ln\left(\frac{x_4}{x_3}\frac{1+\sqrt{1+x_3^2}}{1+\sqrt{1+x_4^2}}\right)\right],$$

where $x_1 = (z-z_0+T/2)/(R+H)$, $x_2 = (z-z_0+T/2)/R$, $x_3 = (z-z_0-T/2)/(R+H)$, and $x_4 = (z-z_0-T/2)/R$. For our set of MOT coils, the parameters have the following values: $z_0 = 0.827$ cm, $R = 0.67$ cm, $H = T = 0.56$ cm.

If the thick coil formulas are used to compute the field gradient at the center of our coil set, we find that our superconducting MOT coils produce a gradient of

$$\text{Actual z-gradient: } \left.\frac{\partial B}{\partial z}\right|_{0,0,0} = 0.877 \text{ G cm}^{-1} \text{ mA}^{-1}.$$

If the thin coil formula is used instead, with the radius and separation measured from the centroid of the windings, the calculated gradient is 0.896 G $\text{cm}^{-1}$ $\text{mA}^{-1}$, which is off by only 2%. Evidently, the high degree of symmetry of this coil configuration tends to cancel out any differences caused by finite-size effects. Therefore, for future calculations with quadrupole traps, the following form for the magnetic field near the origin will be used:

$$\mathbf{B}(x,y,z) = \left(-\frac{B_z^{'}}{2}x\right)\mathbf{e}_x + \left(-\frac{B_z^{'}}{2}y\right)\mathbf{e}_y + \left(B_z^{'}z\right)\mathbf{e}_z$$

with $B_z^{'}$ given above.

### Spin Orientation

One further aspect of the quadrupole field deserves mention. In any magnetostatic trap, it is essential that the atoms maintain their spin alignment with the field in order to remain trapped. Maxwell's equations preclude the existence of a local maximum in the magnetic field in a source-free region of space (such as in a trap) [18]. This requires that atoms in a magnetostatic trap have their magnetic moments oriented antiparallel to the field, so that the magnetic potential energy $-\boldsymbol{\mu} \cdot \mathbf{B}$ can have a minimum at the trap center.

If one considers the field profile of a quadrupole trap, it is evident that the magnetic field lines curve in opposite directions above and below the plane passing through the trap center (see figure 2.2). If an atom in this field is to remain trapped, it must be able to keep its magnetic moment oriented antiparallel to the field over its entire orbital path. This requires that the atom not venture into regions near the trap center where the field magnitude is small. Stated somewhat more quantitatively, a general rule of thumb is that the Larmor precession frequency of the atom be much

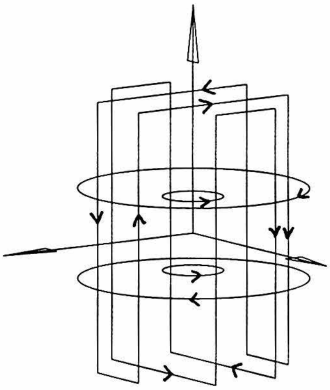

Figure 2.5: The Yin-Yang coil.

greater than the orbital frequency. If this condition is not met, the atom has a high probability of losing its spin orientation and of being ejected from the trap.

These spin-flips (Majorana transitions) are the primary reason for the inadequacy of the quadrupole trap for evaporative cooling. If a quadrupole trap is used in an evaporation experiment, the atoms tend to cluster near the field minimum as the trap cools. The field minimum is precisely the region the atoms need to avoid if they are to maintain their spin orientation and remain trapped. Experiments have shown [19] that the evaporation progresses until huge atom losses are encountered as the trap escapes through the "hole" in the center. Although it is possible to avoid the hole [20, 2], the quadrupole system is extremely difficult to use in evaporation experiments.

Fortunately, a field configuration with a nonzero field minimum exists; this is the subject of the next section.

### 2.5.2 Yin-Yang Field

Our Yin-Yang coil set is a variant of the standard Ioffe coil and is depicted in figure 2.5. There are three sets of coils in this configuration. There is an inner pair of circular coils, an outer pair of circular coils, and a pair of interlocking U-shaped coils. The inner pair is used to provide confinement along the z-axis and to provide a bias field. The U-coils are used for radial confinement, and the outer circular coils provide a means of fine-tuning the overall bias at the center. The currents in each inner coil flow in the same direction. The U-coil currents are such that putting the fingers of one's right hand along the top wires would tend to produce a field in the same direction as the inner coils. The bias coil currents flow in a direction opposite to that of the inner pair. Each pair of coils is separately controllable, providing great flexibility over the field profiles. All useful field configurations, though, have a *nonzero* field minimum at the center with a uniform bias, surrounded by ellipsoidal, constant-$\mathbf{B}$ contours.

The inner circular coils are the same as those described above for the quadrupole field. The coils have 1000 turns of wire each. The outer bias coils have 2000 turns each and have the following dimensions (measured from the centroids of the windings): $z_0 = 1.0$ cm, $R = 2.5$ cm, $H = 0.72$ cm, and $T = 0.72$ cm. The U-coils have 800 turns each with the following dimensions (measured from the centroids of the windings): $l = 3.9$ cm, $h = 6.0$ cm, and $w = 1.6$ cm. The U-coils produce a field perpendicular to the axis of the circular coils, providing radial confinement. The radial field strength increases linearly with distance from the axis.

The coil dimensions were chosen by considering the required field strengths and space constraints inside our trapping chamber. The spacing of the inner coils was made as small as possible (allowing space for 1 cm laser beams) in order to enhance the $z$-curvature of the field. The U-coils were chosen to be relatively tall in order to maximize the radial confinement. In general, the taller the U-coils are, the more uniform is the radial field along the z-axis. Since the atom traps produced with this coil set are long and cylindrical, uniformity of the radial field along the axis is an important consideration.

Figure 2.6 shows a drawing of the forms used for winding the actual Yin-Yang set. The central cage-like structure is the frame for the U-coils, and the symmetric E-shaped figures are the forms for the circular MOT and bias coils. The prong in the center of the circular coil forms marks the centroid of the windings. The forms are machined from free-machining brass in order to minimize eddy currents.

Also shown in the figure is the support structure for the coil forms. The supporting pieces and anchors are made from OFHC copper for purposes of efficient heat transfer.

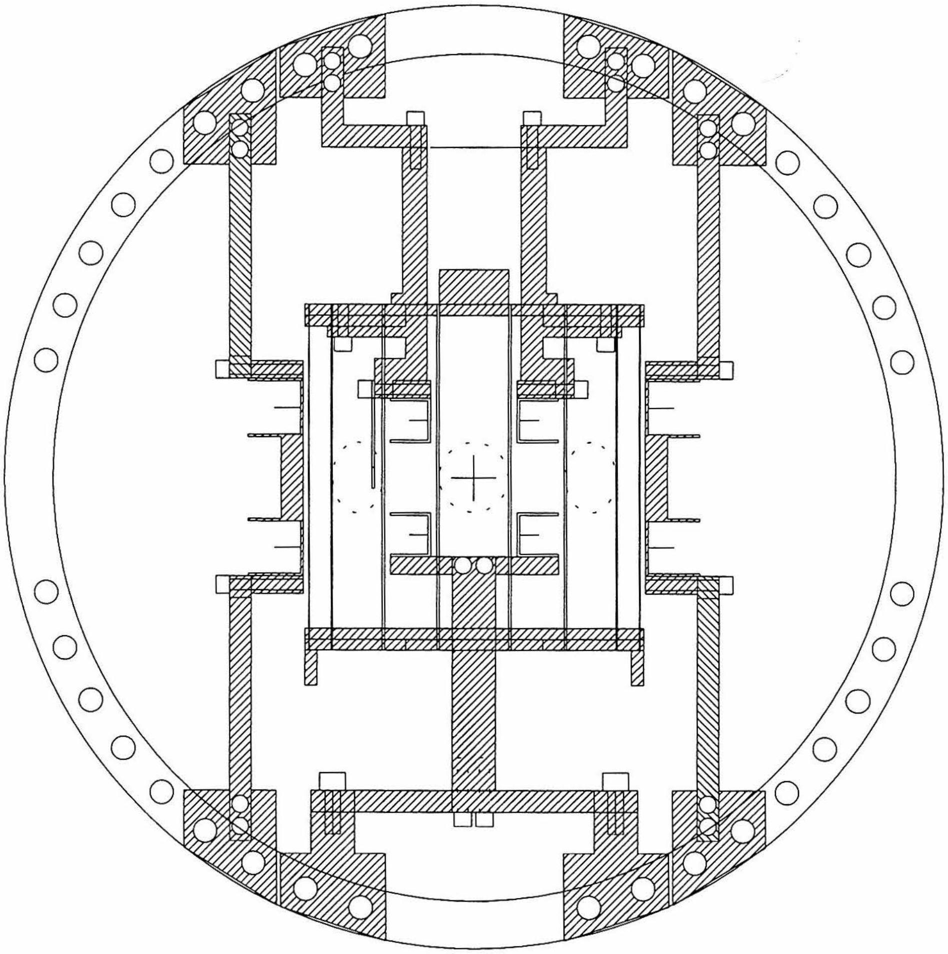

Figure 2.6: Schematic of the actual Yin-Yang coil set.

Heat load considerations will be presented in the next chapter.

## Calculation of the Fields

The geometry of the Yin-Yang set is complicated, making calculation of the fields difficult. To simplify the calculations, idealized, thin-coil expressions were used, since the thin coil approximation is valid to a high degree of accuracy for circular coils (see the quadrupole section above). For the multi-segmented U-coils, the field from each individual segment was calculated in turn. In all instances, the thin coils were taken to be at the centroid of the windings of the actual coil set. The calculated expressions for the fields were then compared with RF probing of actual traps for the needed corrections (this procedure will be described later).

For a circular coil of radius R, at $z = A$, oriented perpendicular to the $z$-axis, the field components at any point in space are [21]:

$$\begin{aligned} B_z(\rho, z) &= \frac{\mu_0 I}{2\pi} \frac{1}{[(R+\rho)^2 + (z-A)^2]^{1/2}} \left\{ K(k^2) + E(k^2) \frac{R^2 - \rho^2 - (z-A)^2}{(R-\rho)^2 + (z-A)^2} \right\} \\ B_\rho(\rho, z) &= \frac{\mu_0 I}{2\pi\rho} \frac{z - A}{[(R+\rho)^2 + (z-A)^2]^{1/2}} \left\{ -K(k^2) + E(k^2) \frac{R^2 + \rho^2 + (z-A)^2}{(R-\rho)^2 + (z-A)^2} \right\}, \end{aligned}$$

where $K$ denotes the complete elliptic integral of the first kind:

$$K(\xi) = \int_0^{\pi/2} \frac{d\theta}{\sqrt{1 + \xi^2 \sin^2\theta}},$$

$E$ denotes the complete elliptic integral of the second kind:

$$E(\xi) = \int_0^{\pi/2} \sqrt{1 - \xi^2 \sin^2\theta}\, d\theta,$$

and the argument $k^2$ equals:

$$k^2 = \frac{4R\rho}{(R+\rho)^2 + (z-A)^2}.$$

For the U-coils, the field from each segment can be computed directly from the

Biot-Savart law. If $\mathbf{r}$ is any point in space, then the field at $\mathbf{r}$ from a current-carrying segment along $d\mathbf{s}$ can be expressed as [22]:

$$\mathbf{B}(\mathbf{r}) = \frac{\mu_0 I}{4\pi} \int \frac{d\mathbf{s} \times \left(\mathbf{r} - \mathbf{r}'\right)}{\left|\mathbf{r} - \mathbf{r}'\right|^3}.$$

For instance, assuming the forwardmost horizontal segment in figure 2.5 to lie between the points $(-l/2, -w/2, z_0)$ and $(l/2, -w/2, z_0)$, its contribution to the Yin-Yang field is:

$$\begin{aligned} \mathbf{B}_1(\mathbf{r}) \; = \; & \frac{\mu_0 I}{4\pi} \left[ \frac{(z+z_0)\mathbf{e}_x - (x - w/2)\mathbf{e}_z}{(x-w/2)^2 + (z+z_0)^2} \right] \left[ \frac{l/2 - y}{\sqrt{(x-w/2)^2 + (y-l/2)^2 + (z+z_0)^2}} \right] \times \\ & \left[ \frac{l/2 + y}{\sqrt{(x-w/2)^2 + (y-l/2)^2 + (z+z_0)^2}} \right]. \end{aligned}$$

All sixteen segments contribute a term similar in form to this one.

From expansions of the field in spherical harmonics [21], general expressions for the field components of an Ioffe trap have been calculated. An generic expression for the field magnitude valid for all of our trapping conditions can be derived [17]:

$$B(\rho, \phi, z) = \sqrt{(\alpha^2 - \beta B_0)\rho^2 + (B_0 + \beta z^2)^2}. \tag{2.3}$$

In this expression, $\alpha$ is the radial field gradient, $\beta$ is the axial field curvature, and $B_0$ is the bias field. These are the parameters necessary for an accurate description of the magnetic field. Near the origin, this expression can be expanded to lowest order, yielding

$$B(\rho, z) = B_0 + \beta z^2 + \frac{1}{2}\left(\frac{\alpha^2}{B_0} - \beta\right)\rho^2. \tag{2.4}$$

The numerical calculations of the fields can be used to find the contribution of each coil set to these parameters. This information is useful for designing trapping configurations, for conducting experiments, and for interpreting trap images. From extensive numerical calculation and from multiple comparisons with actual traps, we have determined the relationship between the coil currents and the Yin-Yang trap parameters to be as follows:

$$\begin{aligned}\alpha &= 0.21 I_U \text{ G cm}^{-1}\\ \beta &= (0.02 I_U + 0.60 I_{Inner} - 0.055 I_{Bias}) \text{ G cm}^{-2}\\ B_0 &= (0.055 I_U + 0.28 I_{Inner} - 0.706 I_{Bias}) \text{ G.}\end{aligned}$$

Here all currents are in milliamps, with $I_U$ the current in the U-coils, $I_{Inner}$ the current in the inner circular coils, and $I_{Bias}$ the current in the outer bias coils. This set of equations has proven exceedingly useful in the design of field configurations for experiments.

# Chapter 3 Introduction to Cryotrapping

## 3.1 Introduction

This chapter describes the cryogenic trapping system in detail. Prior to the work of this thesis, the only other cryogenic systems used for atom trapping were those of the spin-polarized hydrogen groups [23] and an early effort in sodium by Pritchard [24]. The hydrogen traps are formed in a tiny cell buried deep inside a dilution refrigerator. These systems do not use laser cooling and hence cannot be directly compared with the present system. Pritchard's trap used single retroreflected beams for slowing atoms and performing 1-D laser cooling. His system had no MOT capability and it used only fixed-current fields.

The system described in this chapter is the first to merge the benefits of a cryogenic environment with the advantages of 3-D laser cooling. The trapping fields are extremely flexible, as the previous chapter demonstrated, and a wide range of field configurations is possible. The system has full 3-D MOT capability, which is an essential requirement for evaporative cooling experiments. Before describing the system components, though, it is helpful to first review the major disadvantages of room-temperature trapping systems.

## 3.2 Conventional Traps

### 3.2.1 Problems with Trap Lifetimes

The lifetime of a gas of trapped atoms depends critically on the characteristics of the surrounding vacuum. If the vacuum is poor (less than $10^{-10}$ torr), the lifetime of an alkali trap will generally be on the order of a few seconds. Here the term "lifetime" is taken to mean the time required for the number of atoms in the trap to decrease by a factor of $1/e$. For better vacuums, the lifetime increases correspondingly. Since background gas collisions cause the trap to decay exponentially with time, it is evident that careful attention must be paid to the vacuum system.

A vacuum of $10^{-10}$ torr or better is extremely difficult to achieve in a room-temperature vacuum system. Such low pressures require that the surfaces of the vacuum vessel (generally stainless steel or glass) be absolutely clean. The surfaces must be free of all oxides and water, and they must be handled and assembled with the utmost care to ensure cleanliness. A high-temperature vacuum bakeout over the course of several days is required in order to expel contaminants dissolved within the bulk of the vacuum vessel. Even if these procedures are followed, such a vacuum system normally requires several months of continuous pumping to reach pressures into the low $10^{-11}$ torr range. These pressures are so difficult to achieve that only two experimental groups have reported pressures this low [25, 26].

Given the difficulties in achieving such low pressures, one is naturally led to view a cryogenic system as an attractive alternative to room-temperature systems. In general, the vapor pressures of the elements decrease exponentially with inverse temperature [27]. If the walls of a trapping chamber could be cooled to 4K or lower, cryopumping would remove all contaminants from the vacuum except Helium, which is only a trace constituent of air. Indeed, this is exactly the course that has been followed in this thesis. Our apparatus uses a trapping chamber cooled to liquid Helium temperatures. Trap lifetimes up to 4000 seconds have been measured in this system, which, according to the analysis presented in [28], implies an upper bound to the pressure in the trapping chamber of approx. $2 \times 10^{-13}$ torr. This is the lowest pressure ever recorded in an alkali trapping system.

### 3.2.2 Power Dissipation in Trapping Coils

Another difficulty with conventional trapping systems is the need to use extremely high currents to generate even modest magnetic field gradients. Most conventional traps use water-cooled copper tubing for the trapping coils. High currents (sometimes hundreds of amps) are then forced through the copper tubing to generate the necessary magnetic fields. Most conventional systems use currents of $50 - 100$ amps to generate field gradients in the low tens of Gauss/cm range. At the extreme end of conventional systems, Ketterle's group at MIT uses high-pressure chilled water flowing through 21 separately energizable coils. This apparatus uses currents of up to 300A and dissipates 10 *kilowatts* of power!

Because of the high power requirements, another problem with room-temperature coils comes to light: the coils outgass when heated by high currents. If the trapping coils happen to be mounted inside the trapping chamber, the impact of outgassing on the trap lifetime is dramatic. The general solution to this problem has been to mount the trapping coils outside of the vacuum chamber. External mounting solves the outgassing problem (heating of the outer walls of the chamber usually has little effect on the pressure inside), but it does not address the need for high currents and high power. An interesting alternative solution has been put forward by Hulet, who uses a permanent magnet trap [29]. His trap dissipates no power at all, but it comes at the expense of having a trap with non-adjustable magnetic fields.

Our solution to the high-power/outgassing problem has been to take advantage of our cryogenic system and to use superconducting coils mounted inside the vacuum chamber. Superconducting coils produce no heat and hence do not outgass. The coils can generate enormous field gradients: our initial coil set was capable of producing field gradients of 1.5 kG/cm. These are the highest field gradients ever used in alkali trapping experiments, and they provided us a unique opportunity to study the properties of atom traps in high magnetic fields [28].

## 3.3 The Cryogenic System

Before beginning the detailed description of the cryogenic components it is necessary to discuss the overall cryogenic design principles. In any cryogenic system, the primary goal of the design is to shield the coldest cryogen from all possible heat sources in order that it be preserved as long as possible. Sources of heat include thermal radiation from all surrounding surfaces; conduction along wires, contacts, or support structures; and heat transfer through gases surrounding the cooled surfaces.

### 3.3.1 Gaseous Conduction

The gaseous heat transfer problem is minimized by keeping the cryogenic surfaces under high vacuum. According to White [30], the heat transferred through the air between one surface at temperature $T_1$ and another at temperature $T_2$ is bounded above by:

$$\dot{Q}_{gas} = (0.016)P_{mm}(T_2 - T_1)\ \mathrm{W\ cm^{-2}}.$$

Our vacuum system, to be described later, is able to maintain a pressure of approx. $10^{-8}$ torr around the system components for which this equation is relevant (the outer vacuum chamber and the nitrogen-cooled radiation shield). By the above formula, the thermal load due to gaseous conduction is limited to 36 nW cm$^{-2}$, a negligible value.

### 3.3.2 Thermal Radiation

Thermal radiation is a major problem for any cryostat. By the Stefan-Boltzmann law, a blackbody at temperature $T$ emits a radiative power equal to [30]

$$\dot{Q}_{rad} = \sigma T^4 = \left(5.67 \times 10^{-12}\ \mathrm{W\ cm^{-2}\ K^{-4}}\right) T^4.$$

For a surface at room temperature this translates to approx. 46 mW cm$^{-2}$. Without some form of shielding, this constitutes an unacceptable heat load for nearly all helium cryostats. (Of course, no actual blackbodies exist in any real experiment, but, with cryogenic design, it is best to assume worst-case scenarios).

The radiative heat load can be reduced enormously by surrounding the helium-temperature surfaces with surfaces cooled to liquid nitrogen temperatures. This technique is known as *radiation shielding.* By doing so, the radiative heat load is reduced to a factor of $(77/300)^4 = 0.4\%$ of its previous value, which is much more manageable.

Also, modern cryostats and dewars surround all nitrogen surfaces with multiple layers of highly reflective, aluminized mylar film called superinsulation. Mylar has minimal conductive heat transfer through its bulk. The highly reflective surfaces of the multiple wraps reduce the radiative heat load in direct proportion to the number of layers, up to the point at which direct conduction through the layers becomes dominant.

### 3.3.3 Thermal Conduction Across Interfaces

Our cryogenic components are cooled by direct thermal conduction. We have a modular system in order to facilitate assembly and maintenance, so the question of how to best effect heat transfer between two surfaces in contact is of the utmost importance to us. That the system should be constructed from materials of high thermal conductivity is obvious; our critical thermal components are all made of oxygen-free, high-conductivity (OFHC) copper. This type of copper typically has a thermal conductivity of $10^3 - 10^4$ W $m^{-1}K^{-1}$ at 4 K, and it represents the highest thermal conductivity for any material readily available.

Further improvement in the heat transfer between two OFHC surfaces can be obtained by thoroughly cleaning the surfaces and coating them with gold [31]. We employ a multi-step cleaning procedure for our copper that consists of degreasing, deoxidation, surface etching, bright-dipping, and passivation. The detailed procedure is presented in appendix B. After cleaning the copper thoroughly, the thin layer of gold is applied. Coating the surfaces with gold improves the heat transfer, but the reasons for the improvement are not well understood [31]. The gold coating also raises the emissivity of the component surfaces, which helps to further reduce their radiative heat load.

Finally, to achieve superior heat transfer between our OFHC surfaces, thin strips of indium are sandwiched between the gold-coated copper, and the two surfaces are pressed together tightly. The indium flows under pressure, serving to fill in any deformities between the surfaces, even over very small distance scales. By using this indium-enhanced conduction technique, the thermal conductivity across two copper surfaces can be increased dramatically. In practice, we observe no significant temperature gradient across our 6-inch diameter trapping chamber when it is cooled to 4 K, and we observe only a 2 degree temperature gradient across a 1-ft. diameter radiation shield.

### 3.3.4 Thermal Conduction Through Wires

The wires leading into a cryostat are another major source of heat. Our wiring needs are extensive due to the complexity of the Yin-Yang coils and our need to know the temperature of the trapping chamber. In addition, if the wires carry several amps of current (as ours do), the Joule heat produced in the wiring can be another unacceptable source of heat.

The heat conducted down a wire of cross-sectional area $A$, length $l$, and thermal conductivity $\lambda(T)$, with ends at temperatures $T_1$ and $T_2$ is given by the following expression [30]:

$$\dot{Q} = \frac{A}{l}\tilde{\lambda},$$

where

$$\tilde{\lambda} = \int_{T_1}^{T_2} dT\ \lambda(T)$$

is the thermal conductivity integrated between the end temperatures. Obviously, by using material of low thermal conductivity, by making the wires as long and as skinny as possible, and by anchoring the wires at 77 K, the heat load due to the wiring can be minimized.

The joule heating, though, is another problem. We keep all joule heating to a minimum by firmly anchoring all system wires at 77 K and at 4 K. High-temperature superconducting leads are used in the region between 77 K and 4 K. These leads, provided by ZerRes Corp., remain superconducting as long as one end is at 77 K and the other is at or below 20 K. The leads generate no joule heat, and each has a bulk thermal conductive heat leak of 20 mW or less. By following all of the above procedures, our system has operated for several years without thermal failure.

## 3.4 System Overview

Figure 3.1 is a schematic of the cryotrapping system. The major components are a 50-liter liquid Helium storage dewar, an external vacuum chamber, a radiation shield (marked with 77 K in the figure), an internal vacuum chamber (cryosphere), an atomic beam source (not shown), and an interlock system connecting the cryosphere to the beam source. The cryosphere is connected to the dewar via a cold finger and a tetrahedral-shaped connector. In what follows, each individual component will be discussed in detail.

### 3.4.1 The Main Dewar

The main dewar for the system is a modified model 21CNDT research dewar, designed jointly with and constructed by Janis Research. The liquid Helium tank is a 50-liter cylindrical chamber with two exhaust ports and one combination fill/exhaust port. The tank is supported only by its exhaust ports to reduce the conductive heat load on the liquid Helium stored in it. At the base of the helium tank is a needle valve with a long stem controllable by a knob at the top of the dewar. When the valve is opened, liquid Helium flows out of the dewar into a tiny capillary tube at the base of the needle valve. The capillary tube empties into a small pot at the base of the central exhaust tube of the dewar. A piece of gold-plated, high thermal conductivity OFHC copper is silver-soldered to the base of the small pot, forming the cold finger of the dewar. The cold finger has eight #8-32 tapped helicoiled holes in it, onto which samples can be mounted and cooled by conduction. Our cryosphere is attached to this cold finger via a trapezoidal piece of copper, as will be described later.

Surrounding the central Helium tank is a 30-liter liquid nitrogen tank with three exhaust ports. The nitrogen tank serves as a radiation shield to the liquid Helium stored in the central tank. The presence of the nitrogen reduces the radiative thermal load on the Helium as discussed previously. To further reduce the heat load on the liquid Helium the outer nitrogen tank is wrapped in many layers of superinsulation.

To reduce the heat load on the liquid Helium even further, a superinsulation-

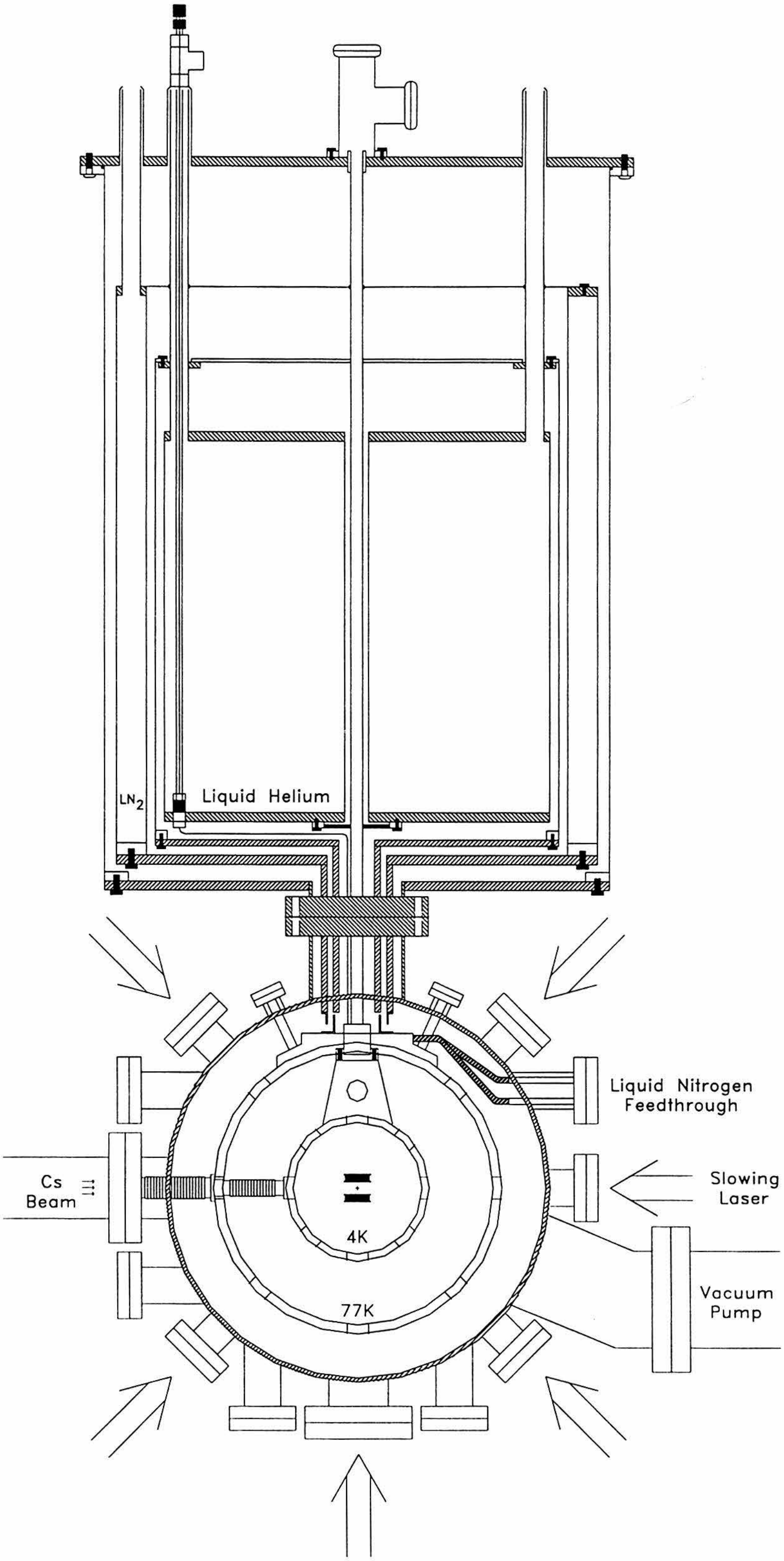

Figure 3.1: The cryotrapping system.

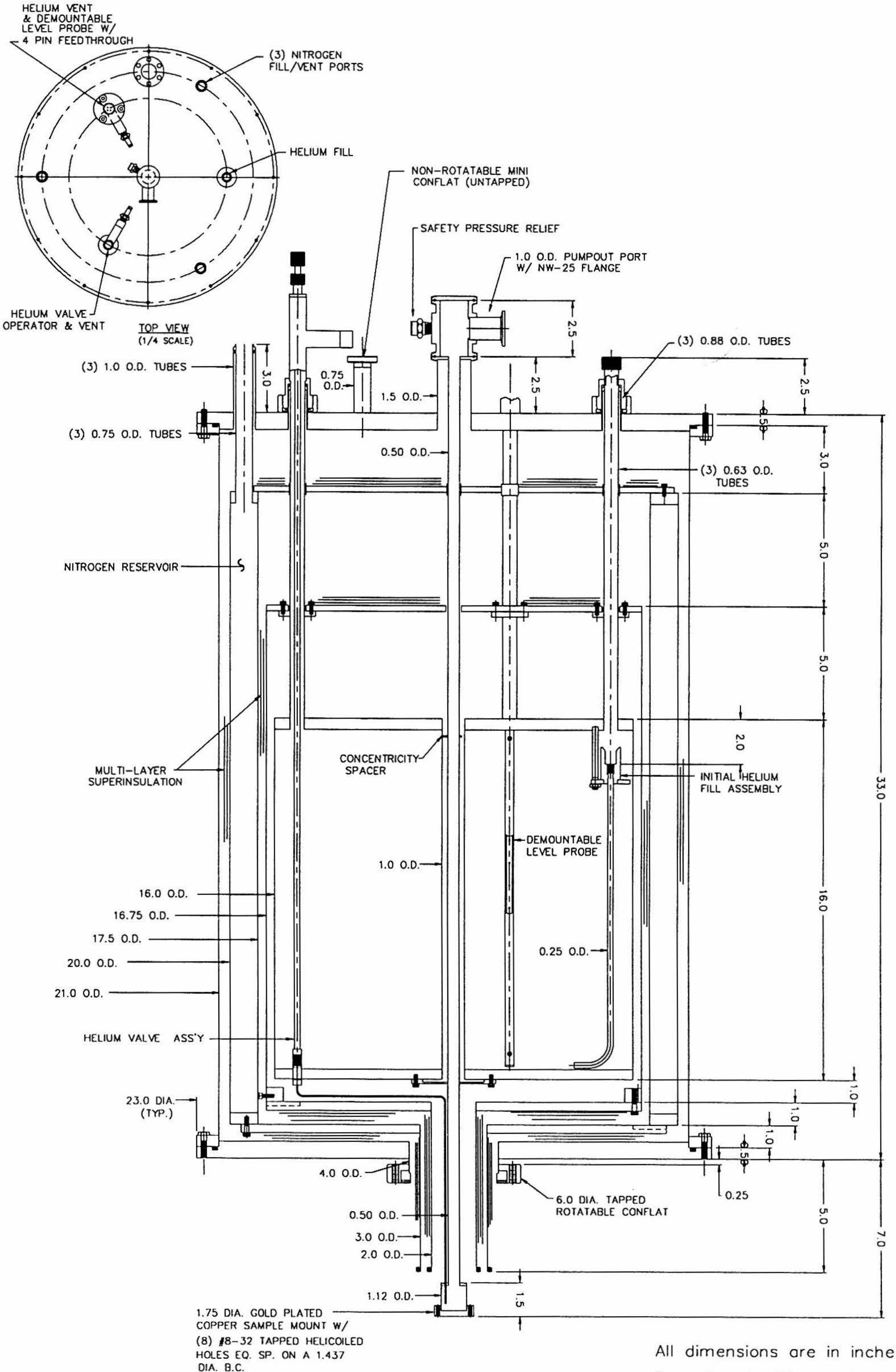

All dimensions are in inches

Reproduced with permission of the Janis Research Co.

Figure 3.2: The main dewar.

wrapped aluminum cylinder is mounted between the Helium tank and the outer Nitrogen tank. This aluminum cylinder is called a *floating shield*, and it reaches an equilibrium temperature between that of the inner helium tank and the outer nitrogen tank. This temperature has been measured to be approx. 60K. With the double radiation shielding and multiple superinsulation wraps, this dewar can store liquid helium for well over two weeks when exposed to the full thermal load of our trapping system.

The procedure for filling the dewar is complicated and is detailed in appendix A. The complication arises from the fact that water cannot be allowed to enter the central tank and collect in the thin capillary tube. If any water did manage to enter the capillary, it would freeze as the dewar cooled. The ice would most certainly clog the capillary, and the expansion of the ice could either pop a hole in the capillary or break one of its seals. In practice, we have not had any trouble with the capillary; we have been able to keep the dewar cold, without warmup, for periods of time exceeding one year.

### 3.4.2 Cold Finger Attachment

The cold finger attachment is a gold-plated, triangular-shaped block of OFHC copper. It has the primary function of providing a connection between the cryosphere and the cold finger of the dewar. It also serves as a z-beam mirror mount and as a heat sink for wires leading to the cryosphere. The piece is attached to the cold finger via eight #8-32 bolts. Twenty-four heat-sink holes for wiring are drilled immediately under the cold finger attachment surface in order to provide efficient heat-sinking of the wires leading to the cryosphere. The trapping coils usually require several amps of current, so their proximity to the cold finger assures that most of the wire-related heat load goes directly into the cold finger and not to the cryosphere.

The cryosphere is attached to the cold finger attachment via twelve #4-40 bolts whose heads rest against the slanted indentations in the attachment. The outer row of six holes has also been tapped with a #6-32 tap to enable breaking of the indium seals

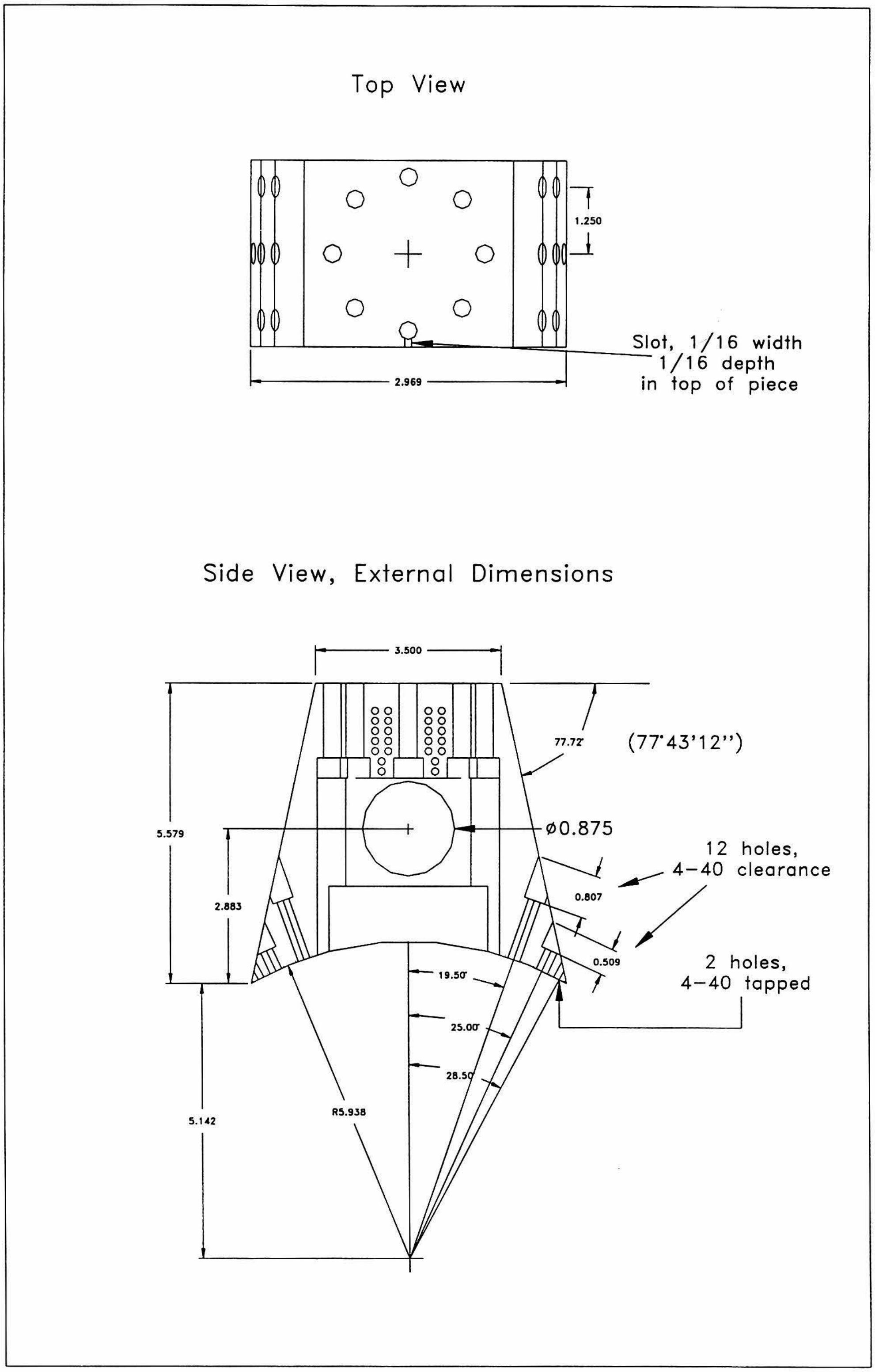

Figure 3.3: The cold finger attachment.

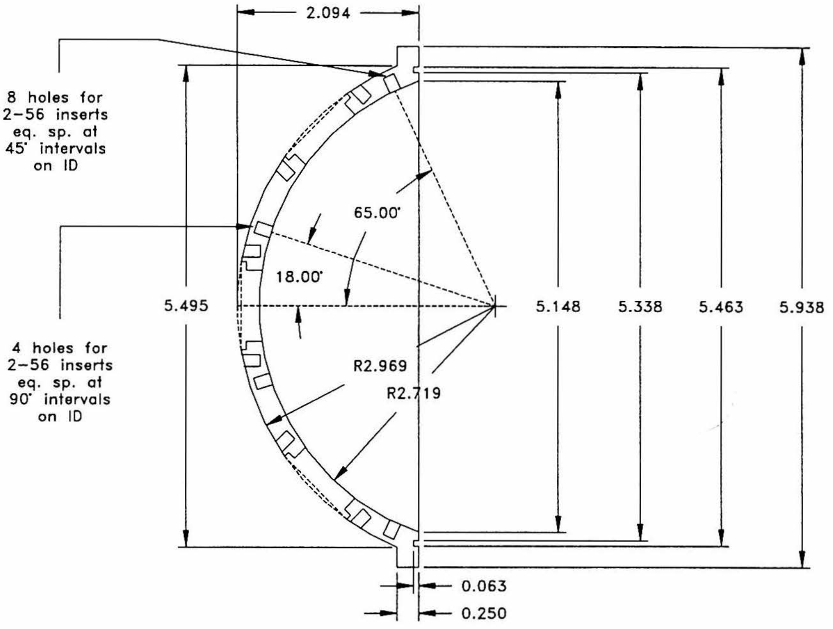

Figure 3.4: An endcap of the cryosphere.

joining the cryosphere and the attachment. The bottom surface of the attachment was cut with a computer-controlled mill to conform exactly to the surface of the cryosphere for maximum thermal transfer.

### 3.4.3 The Cryosphere

The cryosphere is the primary component of our trapping system. Inside the cryosphere the superconducting coils are mounted and the trap is formed. The cryosphere itself consists of three main components: two hemispherical endcaps and a central cylindrical ring. The entire chamber is made of gold-plated OFHC copper and is connected to the cold finger of the dewar via the cold finger attachment described previously.

#### The Endcaps

The endcaps are hemispherical pieces approx. 6 inches in diameter. The outer radius of a cap is approx. 3 inches, and the caps are 0.25 inches thick for mechanical stability and good thermal conduction. A small circular groove is cut into the outermost surface of the caps for mating with the central ring of the cryosphere.

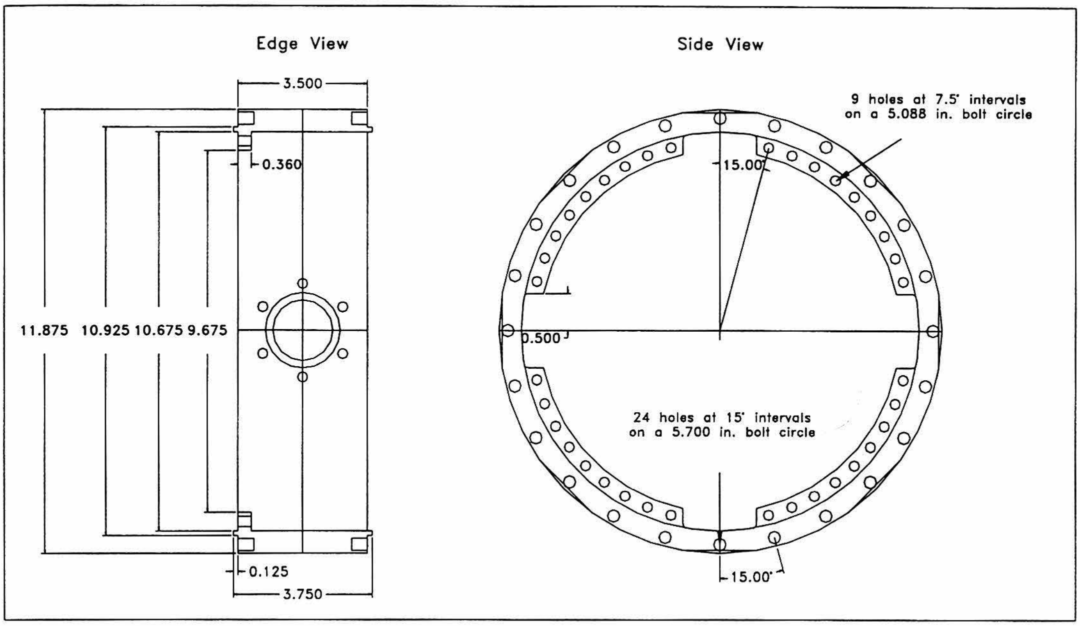

Figure 3.5: The central ring of the cryosphere.

The groove holds a ribbon of indium wire which, when mated with the central ring, expands outward into the groove making a vacuum seal.

The endcaps each contain holes for five windows. The windows are used for admitting laser beams into the cryosphere and for diagnostic purposes. The windows are Pyrex glass slabs 1.00 inches in diameter and 0.25 inches thick. Each window rests in a groove 1.010 inches in diameter and 0.063 inches deep in the surface of the cryosphere, held fast and vacuum tight by an indium seal. A clear aperture of 0.813 inches is cut through the cryosphere underneath the window. A cover plate of gold-plated aluminum rests on top of each window, which is also secured by an indium seal to relieve stress on the glass. Around the circumference of each window are six holes which contain self-tapping inserts [32] for anchoring the window cover plates to the body of the cryosphere.

## The Central Ring

The central ring of the cryosphere is used for supporting the endcaps and the trapping coils. A diagram of the central ring is shown in figure 3.4. The ring is a

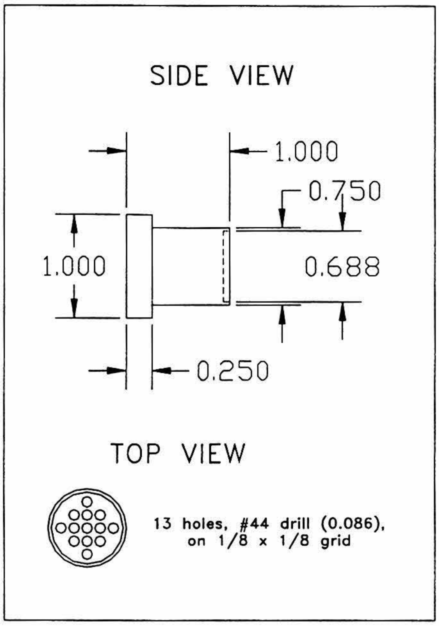

Figure 3.6: The wiring feedthrough.

cylindrical, gold-plated, OFHC copper cylinder 0.25 inches thick. The outer diameter matches that of the endcaps, and the width of the ring is 1.75 inches. On either side of the ring there is a male flange that mates with the groove in the endcaps for forming a vacuum seal. The ring has eight windows cut into it in the manner described above. Self-tapping inserts are placed around the circumference of the ring for anchoring of the endcaps. The inner surface of the central ring has a series of 24 holes, each containing self-tapping inserts for #4-40 screws. This ring of tapped holes provides anchors for the superconducting coil assembly and for the shutter assembly, to be described later.

### 3.4.4 The Wiring Feedthrough

Since our cryosphere is itself a vacuum vessel, the wires for the coils must enter through a feedthrough. We use a basic OFHC copper piece as a mount for several wiring lugs (see figure 3.5). The end of a lug inside the cryosphere is soldered to a superconducting wire, and the other end of the lug is soldered to one of the high-temperature superconducting leads. The wire lugs are 1.5 inch pieces of 2.0 mm diameter, 99.999% pure "five nines" copper wire. The lugs are insulated and held in place by Stycast. The length was chosen to be as small as possible while still providing enough room for soldering. Extremely pure copper (and hence low electrical resistance) is used for this purpose to minimize Joule heat generated in the lugs. At a temperature of 4 K, five nines copper has a resistivity of $\approx 6 \times 10^{-5}\ \mu\Omega\ \mathrm{cm}^{-1}$ [33], giving each lug a resistance of $\approx 7.3 \times 10^{-3}\ \Omega$. At a current of 3 A, a lug generates only 63 mW of Joule heat.

The wiring lugs are one of the primary sources of heat for the cryosphere. The Joule heat generated in the low-resistance lugs puts an upper limit to the current that can be sent through the coils in the system. We have never pushed the system to find out what that limit is. However, the cooling system has been able to survive 4 A in the U-coils and 2 A in the other sets, repeatedly, without difficulty.

The crucial role played by the high-temperature superconducting leads should also be stressed. If these leads were made of normal material instead, even five-nines copper, the Joule heat generated at high currents would overwhelm the cooling capabilities of the system. For most cryostats, Joule heating is not as severe a problem, since the wires are led up the path of the helium exhaust and are cooled by the continual flow of helium vapor. This is not possible for our system because of its modular nature. Thus, by surrounding normal copper wire by superconducting material on both sides, we have enabled a conduction-cooled cryogenic system to carry high currents as well.

### The Shutter Assembly

The cryosphere is isolated from the atomic beam source and the interlock system by a mechanical shutter. The shutter is a gold-plated piece of OFHC copper fashioned into a conical shape. The cone has a base of 1.5 cm diameter and 1.5 cm height. A small diameter hole runs through the center of the cone, inside of which a piece of high-strength fishing line is epoxied with Stycast. When the string is pulled taught the shutter closes over the atomic beam entrance to the cryosphere; when the string is loose, the shutter is caught in a copper ring. The shutter does not form a true vacuum seal for the cryosphere, of course. The seal it does make, though, is adequate to give traps with hour lifetimes and no residual beam loading.

## 3.5 The Interlock System

The interlock system is that piece of the vacuum system connecting the atomic beam source to the cryosphere (see figure 3.6). At the side of the cryosphere near the mechanical shutter is a connection for a 0.5 inch diameter stainless steel bellows. The bellows is anchored at one end to the radiation shield and at the other end to the cryosphere. The connection to the cryosphere is accomplished with OFHC copper pieces fashioned into the form of quick flanges. One piece bolts into the cryosphere and the other clamps around the end of the bellows. An indium seal is used to hold the pieces together, forming a vacuum seal.

At the other end of the bellows, another quick flange connects the outer vacuum chamber to the bellows end. This quick flange is welded to an adapter flange that connects with a gate valve at the end of the atomic beam source. When the gate valve is opened, the atomic beam source, the connecting bellows, and the cryosphere form a closed vacuum system.

Also at the gate valve connection is a vacuum tee leading to a push-pull feedthrough. The push-pull pushes on a 1 lb. weight, which is attached to the other end of the copper shutter by the high-strength fishing line. The push-pull is mounted vertically, so that, when it is fully retracted, the string is taught. This system allows a constant force to be applied to the copper shutter, leading to uniformity in the shutter opening and closing times.

## 3.6 The Radiation Shield and Its Cooling System

Since the cryosphere operates at liquid helium temperatures it must be surrounded by a liquid nitrogen cooled radiation shield, as described in section 3.3.2. This section will describe the radiation shield and its cooling system in detail. The components are

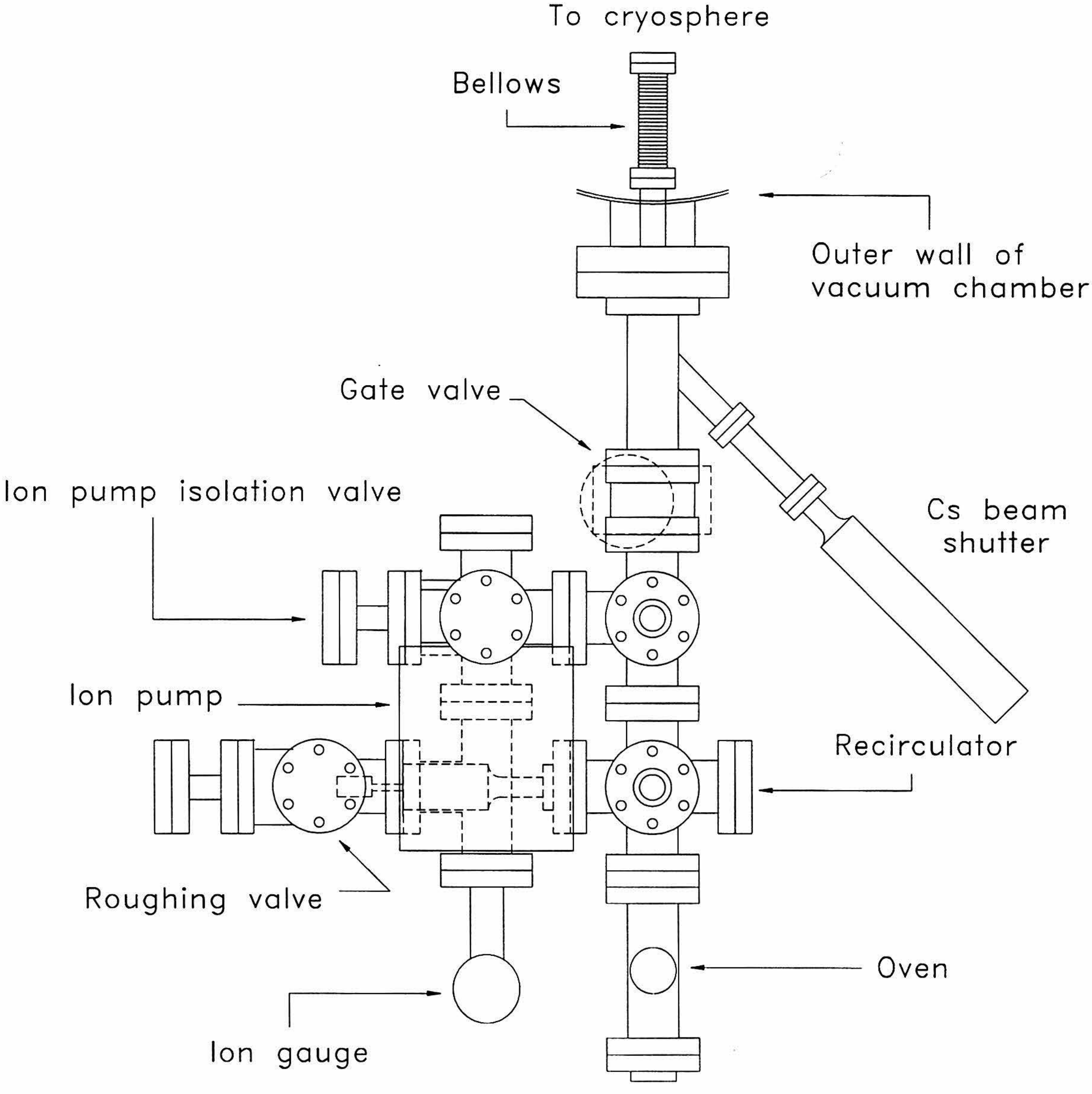

Figure 3.7: The atomic beam source and the interlock system.

the radiation shield and its endcaps, the radiation shield attachment (which supports the shield and joins it to its cooling system), the cooling U-tube and its associated transfer lines, and the liquid nitrogen external dewar.

### 3.6.1 The Radiation Shield

The actual radiation shield itself is a 12.0 inch OD, 3/8 inch thick, gold-plated, OFHC copper cylinder. The shield is composed of three pieces, namely, a main central ring and two endcaps. The shield was divided in this manner in order to make it more manageable (it is extremely heavy) and to facilitate access to the cryosphere. The shield hangs freely from eight #1/4-20 bolts anchoring into a support piece to be described shortly. At the top of the shield are various grooves and holes for wires, support bolts, and for sliding the shield over the cold finger of the main helium dewar. Both sides of the shield have many self-tapping inserts installed for anchoring the endcaps to either side. Also, the shield has seven holes in its outer edges for windows. The details of these windows are similar to those of the cryosphere, but with a 0.937 inch bore. As with the nitrogen jacket in the main helium dewar, this radiation shield is wrapped in fifteen layers of superinsulation.

### 3.6.2 The Radiation Shield Attachment

The entire radiation shield hangs from a curved attachment shown in figure 3.11. This piece is also made of OFHC copper and is gold-plated. The curve of the attachment piece exactly matches the outer radius of the radiation shield in order to provide good thermal contact, as will be described later. The attachment piece fits over the pot and cold finger of the main helium dewar. It is anchored to the outer wall of the vacuum vessel by two 1/16 inch wall stainless steel tubes. On the top surface of the attachment is a U-shaped groove. A copper tube exactly conforming to this shape is soldered into this groove with indium. Liquid nitrogen flows through the tube, cooling it, the attachment piece, and the attached radiation shield by conduction.

The attachment piece also contains 26 0.070 inch holes for wiring lugs. All wires

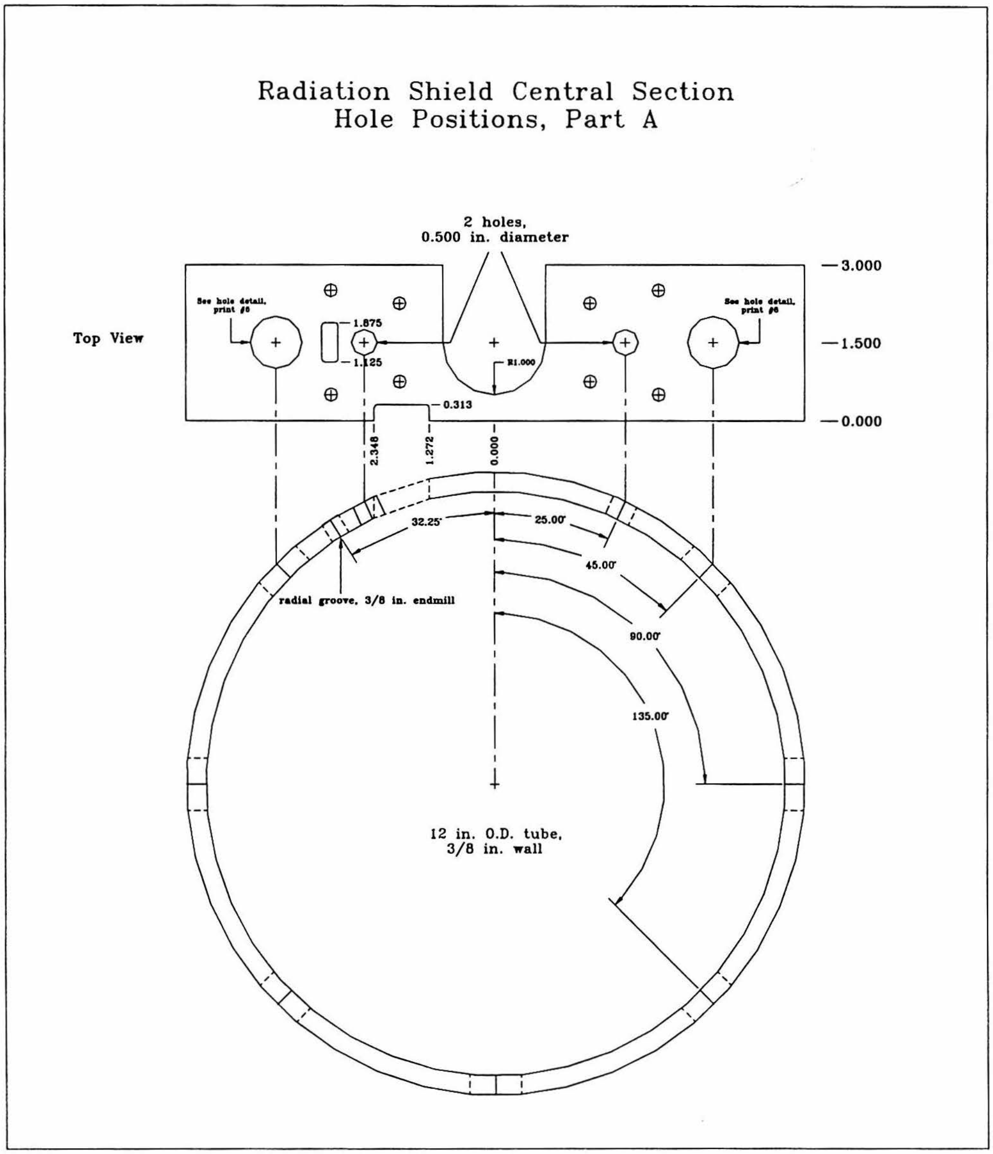

Figure 3.8: The radiation shield, view 1.

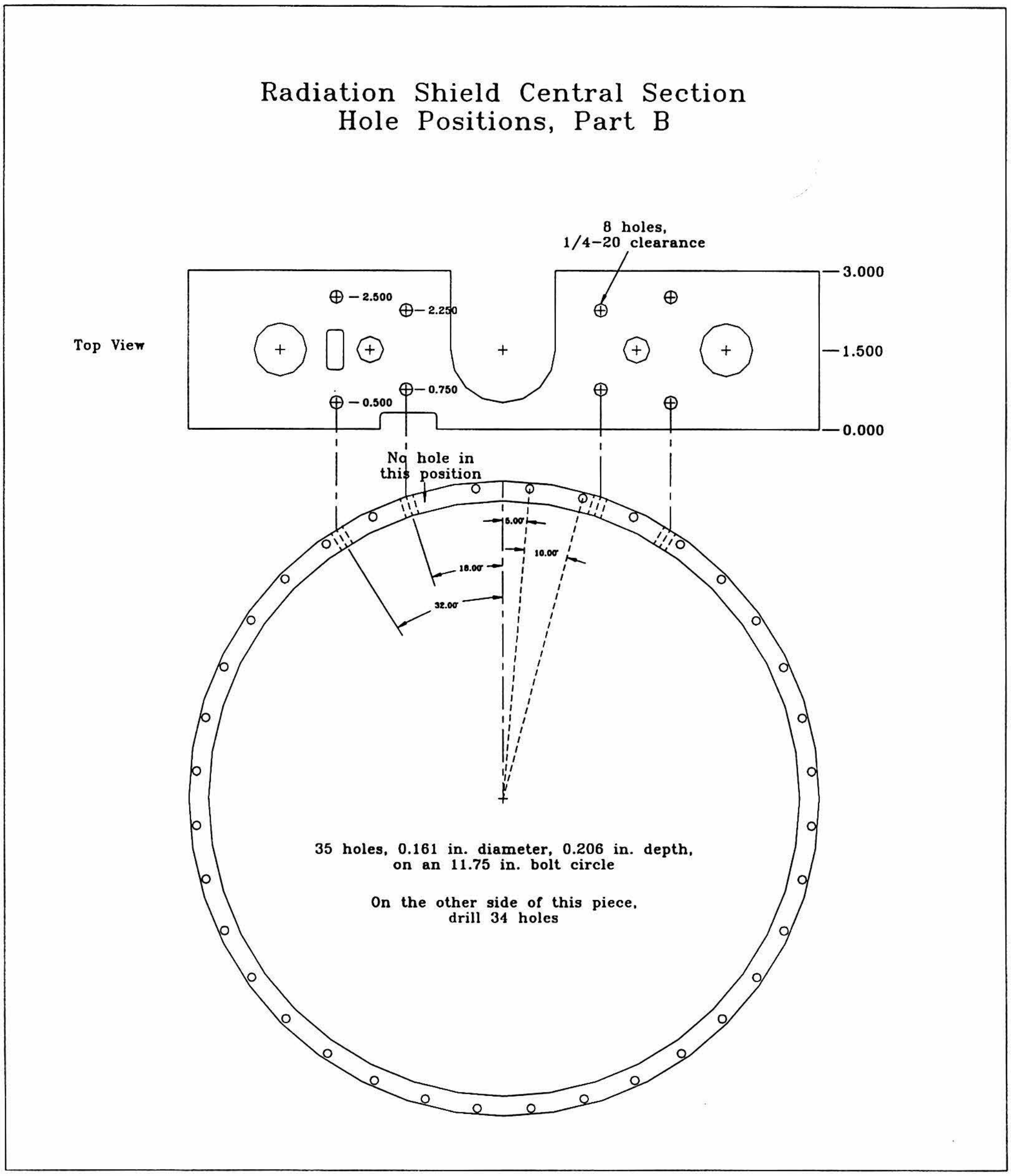

Figure 3.9: The radiation shield, view 2.

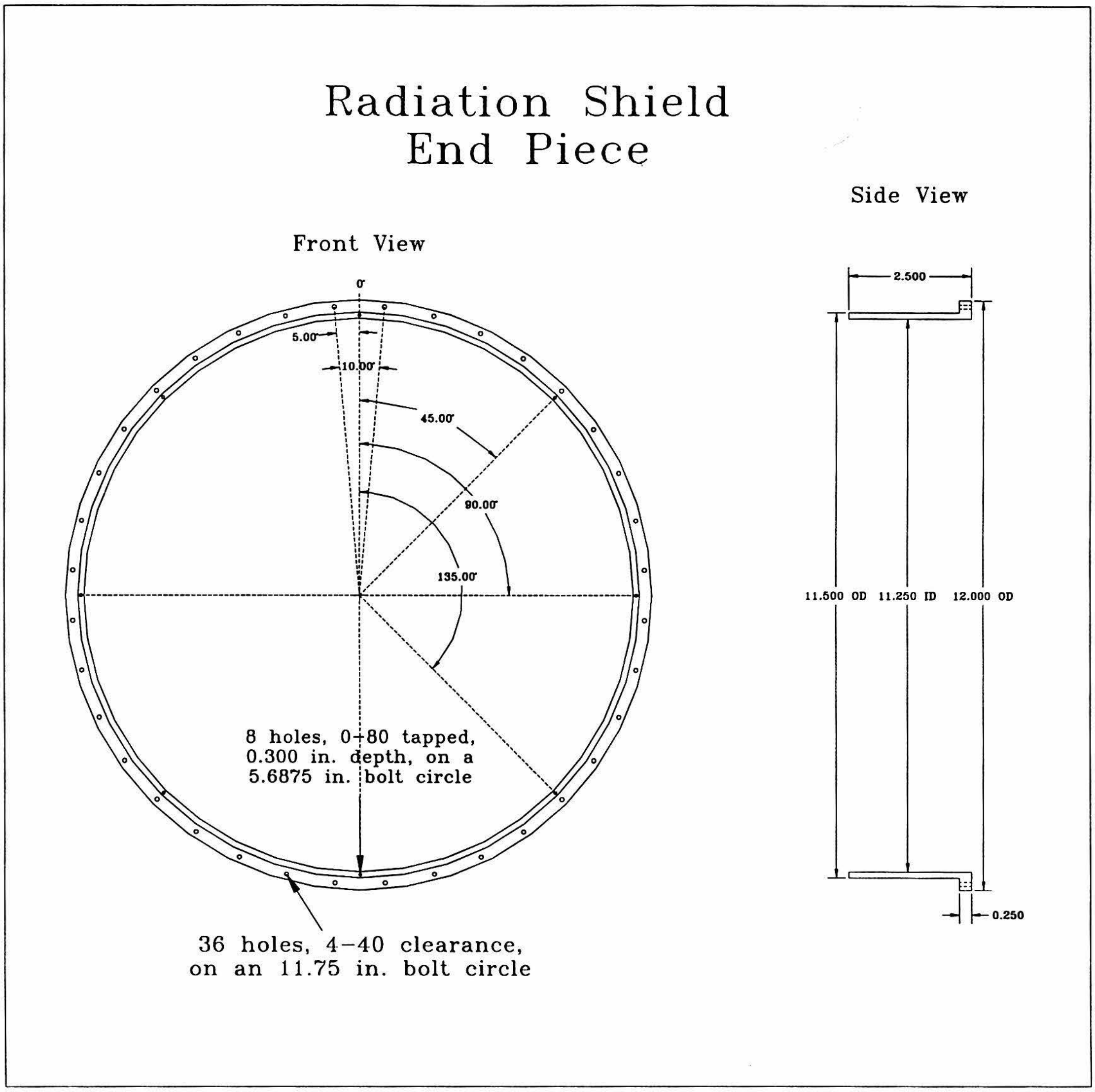

Figure 3.10: The radiation shield endpiece.

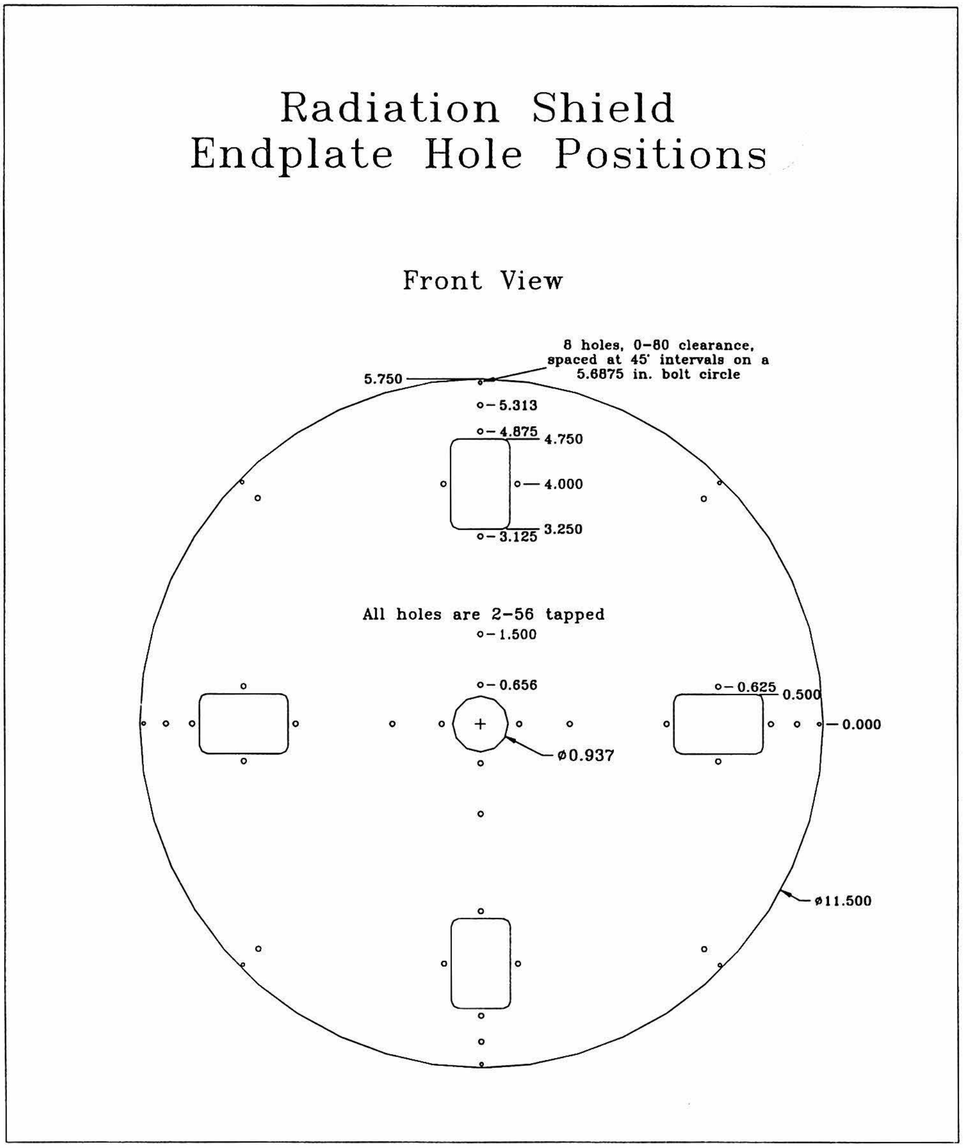

Figure 3.11: Radiation shield endplate.

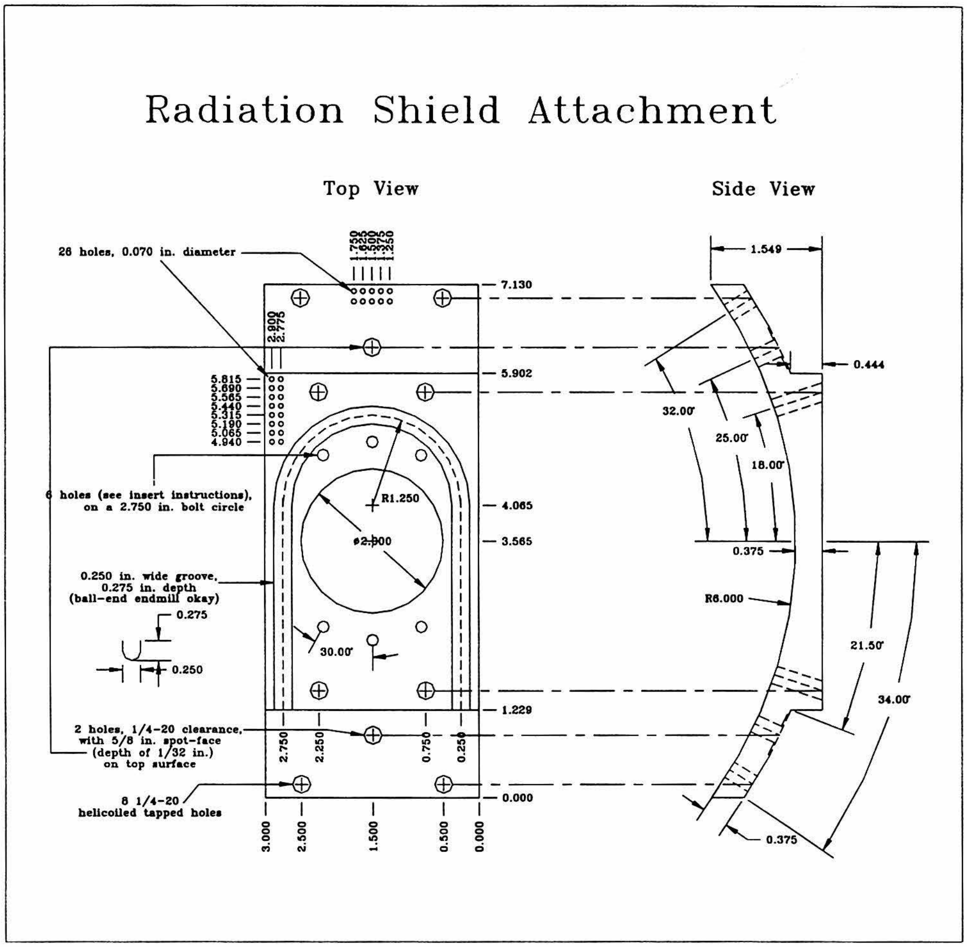

Figure 3.12: Radiation shield attachment.

leading to the cryosphere are thermally anchored at a 77 K point and a 4 K point; this attachment piece is the 77 K anchor. Short (2-3 inches) sections of magnet wire are epoxied into these holes with Stycast. Stycast is a robust low-temperature epoxy with good thermal properties. The ends of the magnet wire were stripped of their insulation and tinned, forming permanent, thermally anchored wiring lugs.

### 3.6.3 The Cooling System

The liquid nitrogen that flows through the U-tube is supplied by an external 30-liter dewar. The dewar hangs approximately 7 feet off the floor, forming a gravity-fed system. The $LN_2$ flows through an insulated transfer line, through a vacuum feedthrough, and through a system of Swagelok fittings and bellows into the U-tube. The ends of the copper U-tube are silver-soldered to a pair of Swagelok fittings to ensure leak-free operation.

The liquid nitrogen flow through this circuit is self-regulating. During cooldown, when the radiation shield temperature is well above 77 K, all of the nitrogen evaporates, increasing the pressure in the U-tube. The increased pressure restricts the flow out of the dewar, preventing an explosive boil-off. As the radiation shield approaches 77 K, the boil-off is less vigorous, causing the nitrogen flow rate to increase. This system is quite robust in practice and has never failed.

# Chapter 4 Lasers, Optics, and Imaging

## 4.1 Introduction

The apparatus described in this thesis relies on an extensive laser and optical system for its operation. There are five lasers used in this experiment: a trapping laser, a repumper laser, a master laser, a slowing laser, and a repumper for the slowing laser. Diode lasers are used in all instances because of their low cost, ease of use, and modest power requirements. Each laser must have its frequency precisely controlled. This section will give an overview of the electronics and optics for each laser, and hopefully will provide some indication of the complexity and extensive maintenance requirements for this system.

## 4.2 The Laser System

### 4.2.1 The Laser Housing

Each laser is mounted inside our custom laser housing (see next figure). The laser itself sits inside an anodized aluminum block mounted on top of a thermoelectric cooler. The TE cooler is used in a servo loop that stabilizes the laser temperature to within 1 mK/hr maximum drift. The laser light is directed to a fast compound lens (Melles Griot 06 GLC 001, 6.5 mm focal length) that collimates the beam into an ellipse with a 4:1 aspect ratio. The collimation can be adjusted by a set screw mounted just to the top of the aluminum block housing the laser. The end of the screw makes contact with a spring-loaded, flexible aluminum hinge that houses the collimating lens. By adjusting the screw, the lens can be moved back and forth to make slight adjustments to the collimation. The screw was purposely given a small range for long-term stability; typically, adjustments to the collimation only need to

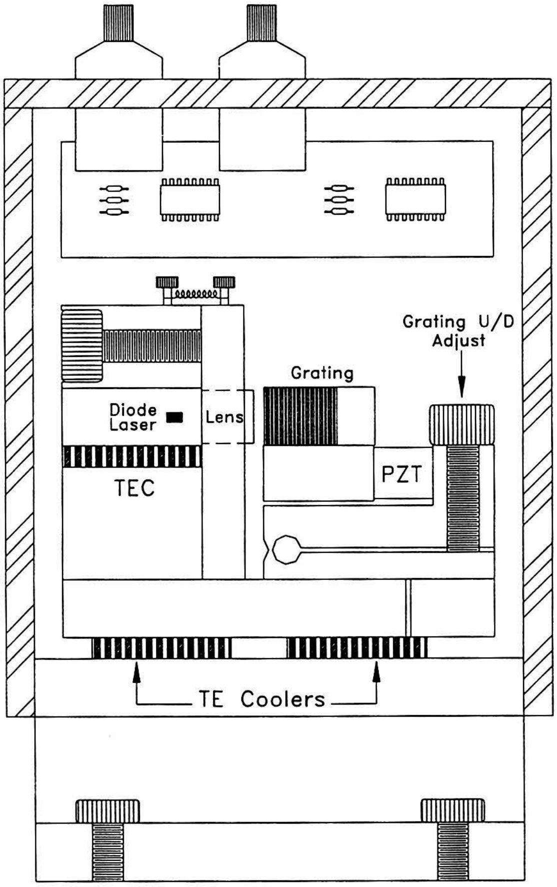

Side View

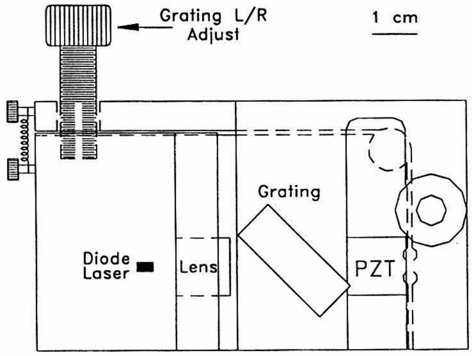

Top View

Figure 4.1: The diode laser housing.

be made every few months.

The collimated laser beam is directed to a holographic diffraction grating (Edmund Scientific J43,224, with 2400 grooves/mm) mounted in the Littrow configuration [34]. The first-order diffracted beam is directed back into the laser to provide feedback for stability and tuning. By varying the tilt of the grating and its position from the laser, the laser frequency can be tuned over a range of several GHz. By adjusting the temperature of the laser, the tuning range can be increased to over 10 GHz. Various set screws in the flexible grating mount are used to adjust the up-down and left-right orientation of the grating, and a piezoelectric transducer is used to control the laser-to-grating distance.

The entire laser-grating assembly sits on top of two peltier coolers which themselves sit upon a thick aluminum baseplate. These two coolers are used in a servo loop that stabilizes the temperature of the laser housing. We have found that this dual temperature stabilization scheme greatly improves the long-term stability of the laser. As a further aid to temperature stabilization, the balanced bridge portion of the temperature stabilization electronics is mounted inside the lucite housing to minimize the effects of temperature drifts on the differential amplifiers.

The current source used for these lasers is that of Libbrecht and Hall [35]. The controller supplies up to 200 mA with a stability of approx. 1 $\mu$A/°C; the current noise is less than 50 nA in a 1 MHz bandwith. The current source has the capacity for direct high-speed (RF) modulation (as our RF stabilization schemes require) and for lower frequency modulation as well.

### 4.2.2 Saturation Spectroscopy

All of our lasers use a saturation spectrum to provide an absolute indication of their frequency. There are many reviews of saturation spectroscopy in the literature [36], so only the major ideas will be mentioned here.

A typical saturation spectroscopy setup is pictured in fig 4.2. Here a strong pump beam (well above the saturation intensity for a given transition) and a *counterpropa-*

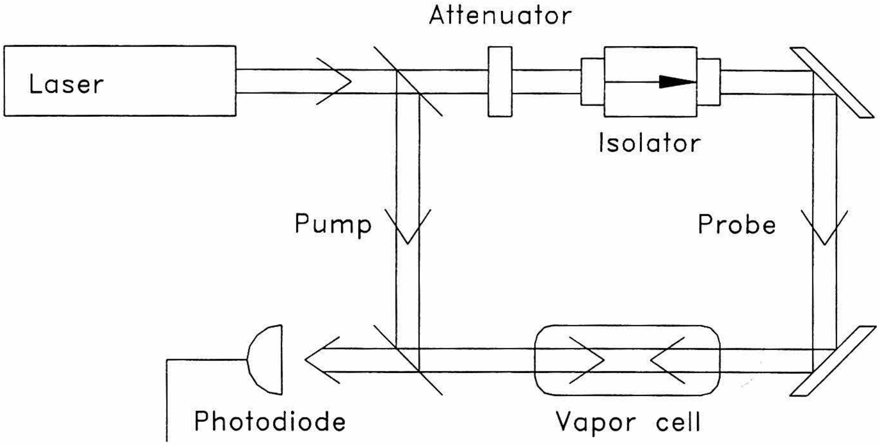

Figure 4.2: Typical saturation spectroscopy setup.

*gating* weak probe beam (well below saturation intensity) intersect inside an atomic vapor cell. If the absorption of the probe beam is monitored, the absorption profile of the probe will be altered due to the presence of the strong pump. If the pump and probe beams have the same frequency and are tuned to resonance with an atomic transition, both beams will be in resonance with all the atoms moving perpendicularly to the axis of the beams. The reason for this is simply that the beams see equal doppler shifts for these atoms. Since these atoms have zero longitudinal velocity, the absorption of the probe beam will be reduced in a narrow interval about the resonance frequency. This will manifest itself as a narrow, doppler-free peak in the absorption spectrum of the probe beam, as shown in fig. 4.3.

If the laser happens to be tuned to a frequency precisely between that of two different resonances, then the pump and probe beams see equal and opposite doppler shifts. The absorption of the probe is once again modified, resulting in the appearance of a *crossover resonance.* A crossover resonance can manifest itself as either increased or decreased absorption, depending on the level structure of the particular atom. For more details on crossover resonances and other aspects of this important spectroscopic technique, see [36].

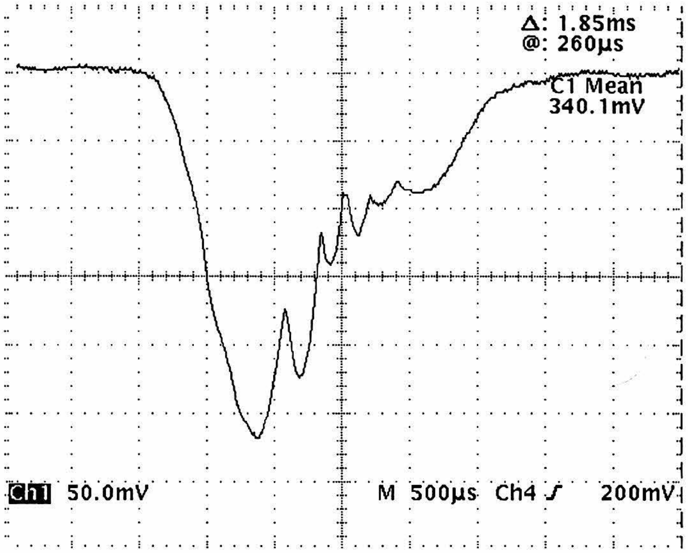

Figure 4.3: Cesium 4-5 saturation spectrum.

### 4.2.3 The Master and Trapping Lasers

Our "master" laser is used to provide a fixed-frequency reference for a heterodyne lock of the trapping laser. To understand how this scheme works, refer to the next figure. Here a simplified schematic of the heterodyne locking system is presented. The master laser is tuned to the $F = 4 \rightarrow F' = 4$ transition. A piece of the emitted beam is sent through an AO and has its frequency shifted up by 126 MHz. The reason for the shift is so that we can lock to the crossover resonance between the $F = 4 \rightarrow F' = 5$ and $F = 4 \rightarrow F' = 4$ transitions. It is desirable to lock to the $4 \rightarrow 5$ crossover because it is the strongest feature in the saturation spectrum, and also because it provides the capability of red and blue detuning for the trapping laser, as will become apparent later.

The upshifted beam from the master laser is combined on a fast photodiode with a piece of the beam from the trapping laser. These two beams beat together on the photodiode, producing a sum and a difference frequency. The sum frequency is in the optical range and well beyond the bandwidth of the photodiode, so a signal at the difference frequency appears at the photodiode output. This difference frequency

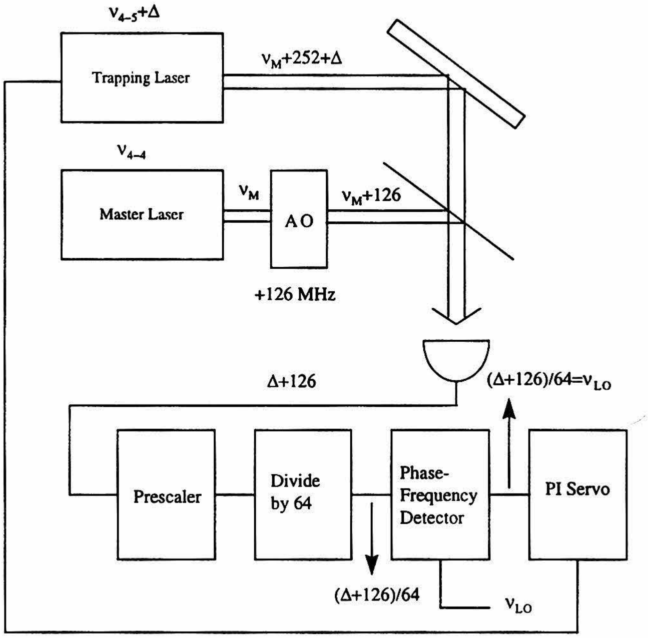

Figure 4.4: The heterodyne locking system.

is equal to $(126 + \Delta)$ MHz, where $\Delta$ is the detuning of the trapping laser from the $F = 4 \to F' = 5$ resonance (see figure).

The RF signal from the photodiode then enters an RF circuit for processing, shown schematically in the previous figure. This circuit was originally designed by Phil Willems [28]. The signal is sent first to a fast Plessey comparator (Plessey SP9685), which converts the analog RF to digital. An MC12022 prescaler then divides down the frequency by a factor of 64 to put it well within the range of our phase-locked loop chip. After passing through an LM361H comparator (used to convert from emitter coupled logic to TTL), the signal then enters a MC4044 phase/frequency detector. This chip contains a phase-locked loop which compares the frequencies of the processed photodiode signal with that of a local oscillator and outputs a signal proportional to the phase difference. This output signal is used as the error signal to a dual-stage PI servo, the output of which is fed back into the current servo of the trapping laser, completing the heterodyne loop.

When the heterodyne loop is closed and locked, the trapping laser can be tuned by changing the frequency of the local oscillator. We use an EH model 1560 programmable pulse generator for our local oscillator. This particular pulse generator has a frequency resolution of 1 ns, which gives us precise control over the frequency of the trapping laser. The EH 1560 is also GPIB-enabled, allowing the trapping laser frequency to be controlled by a computer. The frequency switching time of the EH generator is nearly 80 ms. This is acceptable for switching the trapping laser frequency if an MST is present, but unacceptable if a MOT is present (MOT timescales are typically 1 ms or so). For fast frequency switching of the trapping laser, a National Instruments PCTIO-10 timing board is used as a local oscillator switchyard. This board can handle multiple frequency inputs and can switch between them on timescales of about 40 $\mu$s.

From a consideration of the frequencies at the phase locked loop chip, an expression relating the frequency of the local oscillator $v_{LO}$ and the detuning $\Delta$ of the trapping laser can be derived. When the loop is locked, the two input frequencies it sees must be identical, so

$$\frac{\Delta + 126}{64} = v_{LO}$$

or

$$\Delta = (64 v_{LO} - 126) \text{ MHz}.$$

From this expression it is clear that the trapping laser can be tuned about the $4 \rightarrow 5'$ transition anywhere within the range of $-126$ MHz (where $v_{LO}$ is zero) to $+126$ MHz (where $\Delta$ is zero).

### Master Laser Servo

Of course, the trapping laser stability is highly dependent on the master laser stability. For locking the master laser, a modified Pound-Drever method is used [37]. FM sidebands at approximately 8 MHz are impressed upon the master laser by direct modulation of its drive current. The sidebands are 180° out of phase with one another. If the master laser is tuned precisely on the $4 \rightarrow 5$ resonance, the sidebands suffer equal attenuation as they propagate through the doppler-free saturation resonance. Phase-sensitive demodulation of the RF saturation signal then shows no signal present

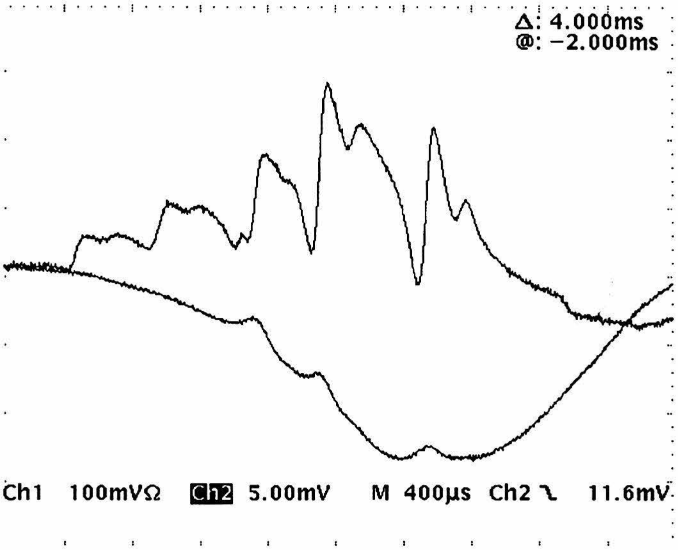

Figure 4.5: Master laser error signal.

at the modulation frequency, since the sidebands both beat with the carrier, and are $\pi$ out of phase with each other. If the laser frequency should drift, though, one sideband is attenuated to a greater degree than the other. In such a case, a non-zero signal at the modulation frequency can be recovered from the saturation signal. If the laser frequency is swept through resonance, the standard bipolar error signal is produced [37], as figure 4.5 demonstrates:

The central slope of the curve is used as the error signal for stabilizing the master laser. A dual PI servo was constructed for this purpose. The servo has a differential input for removing any common-mode noise on the error signal. The error signal is then combined with a setpoint voltage, amplified, and filtered. When the servo is engaged, a PI compensation stage is directly coupled to the laser current control, while a slow integral stage is used to control the PZT that moves the laser grating. When this servo is used in conjunction with the heterodyne lock for the trapping laser, the residual linewidth of the trapping laser can be reduced to the 100 kHz range for periods of several hours.

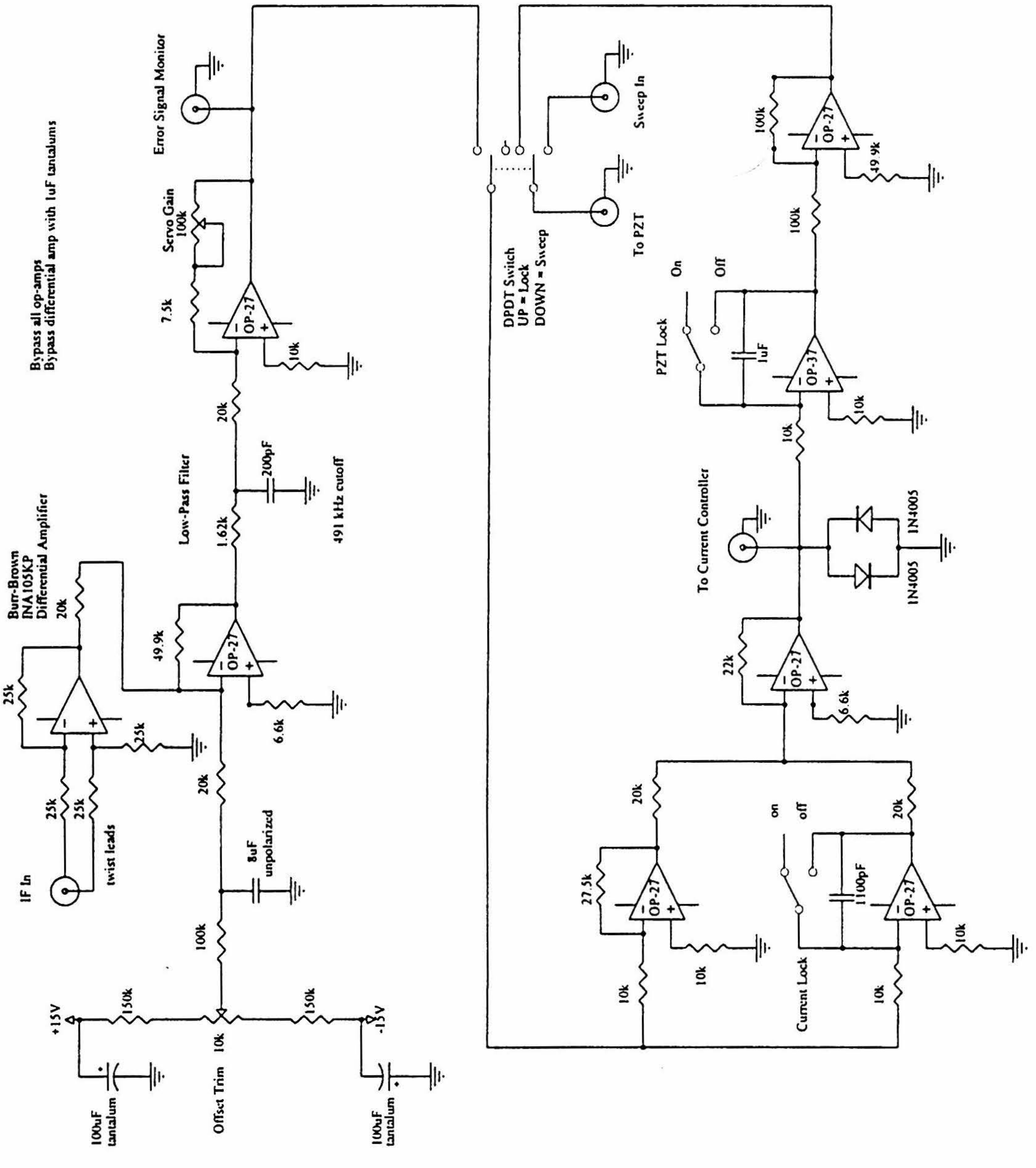

Figure 4.6: Servo for the master laser.

## 4.3 The Optical System

### 4.3.1 The Trapping and Master Laser Optical Systems

The exact optical setup used to perform this heterodyning is shown in figure 4.7. A legend identifying the figures used is presented in figure 4.8. Some general comments can be made about the optical layouts for the master and trapping lasers. Both beams emerge from their respective lasers with an elliptical aspect ratio (see the section on the laser housing) which is not an appropriate beam shape for laser cooling. Therefore each beam is sent through a pair of Melles Griot anamorphic prisms which convert the beam shapes from elliptical to circular. Each beam is telescoped down and sent through an Isomet isolator. Semiconductor lasers are very susceptible to feedback, so isolators are necessary to prevent unwanted, feedback-induced frequency pulling.

After its isolator, the master laser beam is coupled through a $\lambda/2$-polarizing beamsplitter combination to the 126 MHz AO. After emerging from the AO, the beam is split into two pieces: one piece goes to a saturation cell (for frequency monitoring), and another piece goes to the trapping laser heterodyne lock photodiode. The beam from the trapping laser involved in the heterodyne lock is split off from the main trapping laser beam by a wedge prism. Wedge prisms produce two beams (front and back reflection from the wedge). The other piece from the wedge goes to form the trapping laser saturation spectroscopy signal.

After emerging from the wedge prism, the trapping laser beam is coupled through a $\lambda/2$-polarizing beamsplitter combination. One piece from the PBS goes to an AO to form the optical pumping beam, while the other piece goes through another isolator to form the main trapping beam. The optical pumping AO shifts the frequency to within a few MHz to the red of the $F = 4 \rightarrow F' = 5$ transition. This beam is then sent through a shutter and a combination of various lenses to make its shape as round as possible. After the lens combination, the beam is circularly polarized and coupled into the main z-trapping beam.

The piece of the trapping beam emerging from the second isolator is tightly focussed through a Newport mechanical shutter. The tight focussing enables the trap-

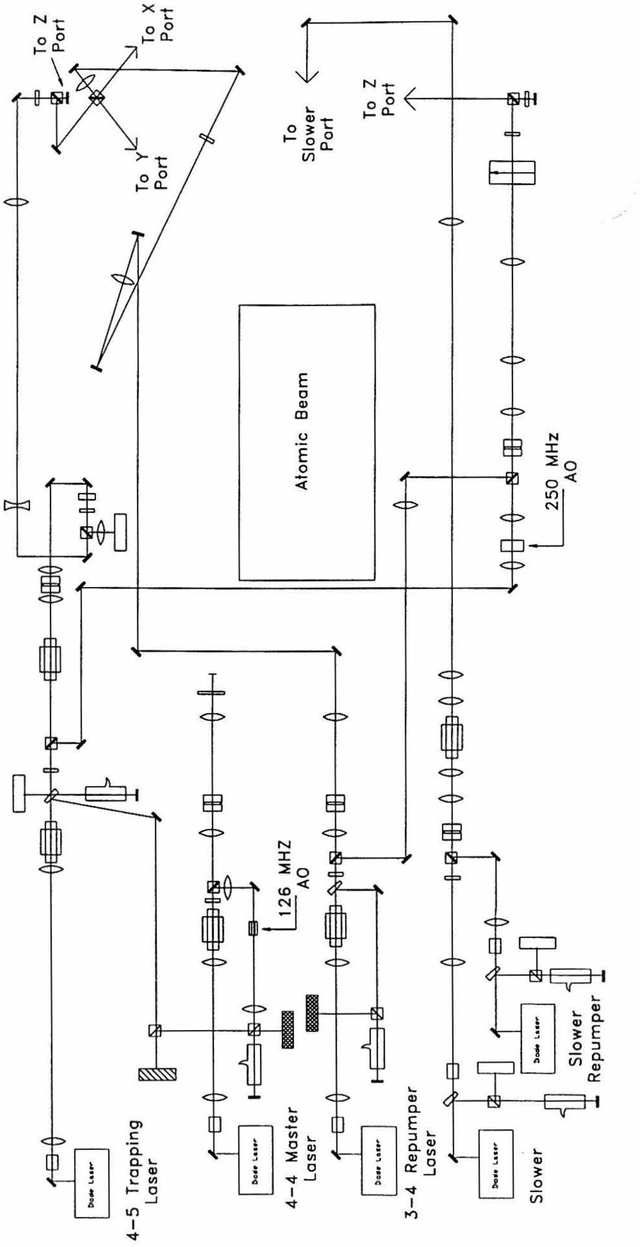

Figure 4.7: The optical system.

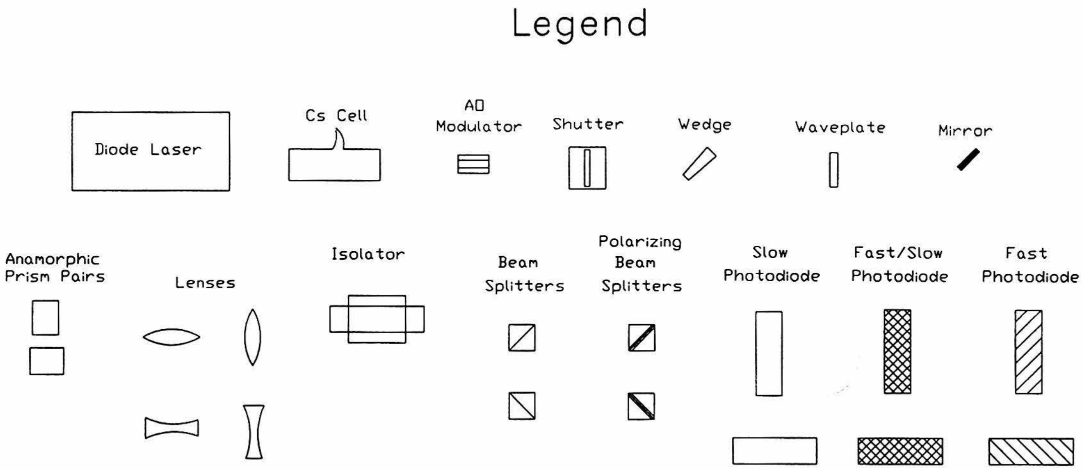

Figure 4.8: Symbols used for optical elements.

ping beam to be extinguished within a measured time of 15 $\mu$s. A fast extinction time is necessary to avoid spurious heating effects during the various stages leading up to evaporative cooling. After emerging from the shutter, the beam is sent through a DisplayTech light valve (for intensity control during PG cooling) and then another $\lambda/2$-PBS coupler. One piece from this beamsplitter is directed onto a photodiode that produces a TTL signal (active low), used for triggering a Xybion intensified CCD camera for trap imaging. The remaining trapping laser beam that is not used for triggering the CCD camera is sent to a combination of beamsplitters and $\lambda/2$ couplers to form the beams used for the actual atom traps.

### 4.3.2 The Repumper Laser Optical System

Our repumper laser does not need the exceptional frequency stability that the master and trapping lasers need. The repumper only needs to have its frequency in the vicinity of the $F = 3 \rightarrow F^{'} = 4$ transition. Its purpose is to help keep atoms on the $F = 4 \rightarrow F^{'} = 5$ trapping transition by repumping any atoms off-resonantly excited to the $F = 3$ level (see discussion in chapter 1). The optical layout of the repumper is similar to that of the master laser (see figure 4.7 ), and its servo is similar as well. From the diagram of the optical layout, it can be seen that a piece of the repumper laser is mixed in with the optical pumping beam. This piece of the repumper is circularly polarized and illuminates the trap whenever the optical pumping beam is on. It was hoped that, by adding this additional $\sigma^+$ beam during optical pumping, the pumping could be enhanced. In practice, though, the enhancement in optical pumping due to this beam is negligible.

## 4.4 The Imaging System

### 4.4.1 Introduction

The primary means of obtaining information about our atom traps is through fluorescence imaging. After forming an MST and performing any desired experiments with it, the lasers are flashed on and an image of the fluorescing atoms is taken. The width of the atom cloud is directly related to the temperature of the atoms, and the atom number is proportional to the intensity of the fluorescence. By capturing a known amount of the fluorescence with a calibrated photodiode, the number, density, and temperature of the atom cloud can be determined.

The camera is the crucial piece of equipment here. We use a highly sensitive, intensified, charge-coupled device (ICCD) camera to take images of our traps. The camera is a Xybion Electronic Systems model ISG-350 with a GEN-III intensifier. The ICCD consists of the intensifier, which multiplies the incident photon flux by several orders of magnitude (without degrading the resolution) followed by a CCD array.

The camera acquires an image in the following manner. Incident photons are converted to electrons by a photocathode. The electrons pass through a multichannel electron multiplier and strike an output phosphor, where they are converted back to photons. The photons get captured by a fiber optic minifier and are coupled directly to the CCD array. The CCD accumulates electrons for the duration of the image, after which time the camera reads the CCD and forms the image.

The process of acquiring an image requires careful synchronization of the lasers.

During the time the MST is held before imaging, the trapping and repumping beams are shuttered closed and the trap is completely in the dark. Each of these beams is controlled by a Newport mechanical shutter. The trapping laser beam is focused to a fine point in the plane of the shutter aperture; the rise time of the light when the shutter opens is approximately 20 $\mu$s.

To take an image of the trap, the repumper shutter is given a command to open first. From the time the command to open is given to the time the shutter becomes fully open is nearly 5.8 ms. Four milliseconds after issuing the command to open the repumper shutter the trapping laser shutter is told to open. The four millisecond delay is chosen to allow for any variation in the rise time of the repumper shutter. The delay also ensures that the repumper is fully open when the trapping laser shutter starts to open.

A piece of the trapping beam is split off after the shutter to be used as a camera trigger. This light is focussed onto a photodiode that produces a TTL LOW signal when illuminated and a TTL HIGH signal when not illuminated. This convention is used to satisfy the Xybion ICCD camera, which requires an active TTL LOW gate. The CCD array is exposed at the instant when the trapping shutter becomes fully open, typically 5 to 7 ms after the trapping laser shutter is told to open. During the wait for the trapping laser shutter, the atoms in the $|4,4\rangle$ state do not interact with the repumper light, since it is tuned to the $F = 3$ to $F' = 4$ transition, and is 9.2 GHz out of resonance with the atoms.

We typically expose only one video field of the image. The video signal is sent to an Imaging Technologies *PC Vision Plus* Frame Grabber card and is stored in the card's frame memory. The single-field image is stored in a file, and then is read back into the frame memory of the frame grabber card. When reading the image back in, the captured field is doubled in the vertical direction to give the image the correct 640 X 480 aspect ratio.

A video monitor connected to the frame grabber card allows a visual inspection of the image. To analyze the image and determine the trap temperature, a white box is displayed on the video monitor to delineate a portion of the image. The user can

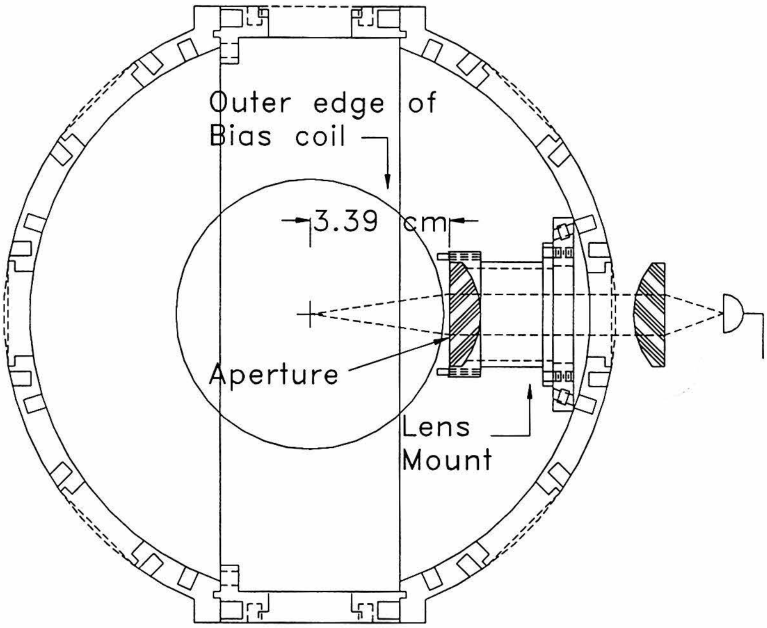

Figure 4.9: The trap imaging system.

adjust the sides of the box to select a piece of the image for fitting. After selecting the piece of the image with the trap profile in it, the frame grabber card is disabled and the selected image portion is written to the video memory of the computer. The image is then colorized, filtered with a 3 X 3 median filter, and displayed on the computer screen for fitting.

### 4.4.2 Determination of the Number of Atoms

The number of atoms in a trap can be determined by first measuring the fluorescence from the trap and then dividing by the calculated fluorescence per atom. It is not possible to capture all of the light emitted by our trap into a full $4\pi$ steradians, since we have only a limited number of ports with which to view the trap. Hence it is necessary to determine the fraction of the total fluorescence captured by our imaging system.

Our imaging system is shown in figure 4.9. The system consists of a 1cm aperture (a thin Beryllium copper plate), a fast lens and lens mount, and a photodiode mounted outside the vacuum chamber. The aperture was limited to 1 cm to reduce spherical aberration, in case any video images were to be taken through this port. The lens mount was designed to position the lens one focal length away from the center of the trap. With this arrangement, the light captured from the trap comes out parallel to the imaging axis and is focussed on the photodiode. The photodiode is mounted inside a low-noise amplifier module and has been carefully calibrated. The calibration information enables a conversion from emitted power to a measured photodiode voltage.

From the figure, it can be seen that the trap center is 3.39 cm from the 1 cm aperture, subtending a solid angle of 0.067 steradians. This system is therefore able to capture $0.067/4\pi = 0.0053 = 0.53\%$ of the total emitted fluorescence.. As the light makes its way through the imaging system, approximately 10% of it is absorbed by the lens and the windows of the vacuum system. Hence the power detected by the photodiode ($P_{\mathrm{det}}$) is related to the power an atom actually emits ($P_{atom}$) as follows:

$$P_{\mathrm{det}} = (0.0053)(0.90)(P_{atom}),$$

or

$$P_{\mathrm{det}} = (0.0048)P_{atom}.$$

The total power that an atom radiates can be expressed as $P_{atom} = \hbar\omega_L\Gamma\Pi^e$, where $\Pi^e$ is the population of all excited states [12]. This expression assumes that all the transitions have the same frequency, and that they all have equivalent transition rates $\Gamma$. For the cesium atom, the transitions of interest occur between the lower hyperfine ground state levels and the excited state $6^2P_{\frac{3}{2}}$. Even though the $F = 3$ and $F = 4$ hyperfine levels are separated by 9.2 GHz, this separation is a negligible fraction of the ground to excited state transition frequency of 3.5 x $10^{14}$ Hz. Hence the expression for $P_{atom}$ is valid.

For a two-level atom in a plane wave of Rabi frequency $\Omega$ and detuning $\delta$, the expression for the power radiated becomes [9]:

$$P_{atom} = \hbar\omega_L \frac{\Gamma}{2} \frac{\Omega^2/2}{\delta^2 + \Gamma^2/4 + \Omega^2/2}.$$

Unfortunately, cesium atoms in MOTs do not satisfy the conditions under which this expression is valid. As explained by Townsend *et al.* [12], this expression must be averaged over all the transitions between the Zeeman sublevels in both the ground and excited states. Further complicating this picture is the realization that the Rabi frequency and the local polarization of the electric field vary with position in the trap. The generally accepted method for handling these complications [38] is to assume that the radiated power can be expressed as follows:

$$P_{atom} \cong \hbar\omega_L \frac{\Gamma}{2} \frac{C_1^2\Omega_T^2/2}{\delta^2 + \Gamma^2/4 + C_2^2\Omega_T^2/2}.$$

Here $C_1$ and $C_2$ are Clebsch-Gordan coefficients averaged over all possible transitions. From careful measurements made over a six month period, Townsend *et al.* find $C_1^2 = C_2^2 = 0.7 \pm 0.2$.

The Rabi frequency $\Omega_T^2$ is determined by the average laser intensity in the trap:

$$\Omega_T^2 = 6\Omega^2 = 6\Gamma^2 \frac{I_{avg}}{2I_0},$$

with the 6 arising from the fact that there are 6 laser beams intersecting at the trap center. The quantity $I_0$ is the saturation intensity of the given transition; for the $F = 4$ to $F' = 5$ trapping transition in cesium, $I_0 = 1.1$ mW cm$^{-2}$.

Calculation of $\Omega_T^2$ requires a convention for expressing the average intensity of one of the trapping laser beams $I_{avg}$. The standard practice is to express the intensity profile of the beam as follows:

$$I(r, \phi) = I_0 e^{-r^2/\sigma^2}.$$

If the width $\sigma$ can be measured, a radius can be found at which the beam intensity is down from its peak intensity by a factor of $e^{-2}$. The beam intensity is then defined to be the total power contained within the $e^{-2}$ diameter, divided by the $e^{-2}$ diameter.

Experimentally, the width $\sigma$ is determined by measuring the power transmitted through apertures of various diameters. The measured powers are then fitted to an expression found by integration of the beam intensity profile. If the above expression for $I(r, \phi)$ is integrated over $r$ and $\phi$, the total power contained in a circle of radius $R$ centered on the beam can be shown to be:

$$P(R) = \pi\sigma^2 I_0 \left(1 - e^{-R^2/\sigma^2}\right).$$

We sent our beam through apertures varying in diameter from 5 mm to 1 mm; our fitted curve indicates that $\sigma = 3.23$ mm. Our $e^{-2}$ diameter is then $2r_e = 2\sqrt{2}\sigma = 9.14$ mm, which gives an effective area for our beam of 0.65 cm$^2$. If an aperture of radius $R$ is used to measure the power of the laser beam, the average intensity of the beam is

$$I_{avg} = \frac{P(R)}{0.65} \text{ W cm}^{-2}.$$

Knowledge of the average beam intensity allows a calculation of the Rabi frequency $\Omega_T^2$ and therefore the power radiated by a single atom $P_{atom}$. By triggering a storage oscilloscope at the instant the image is taken, the voltage signal can be read and converted into an emitted power from the above calibration table. Dividing the equivalent photodiode power by the calculated $P_{atom}$ yields the number of atoms in the trap.

### 4.4.3 Determination of the Trap Density and Temperature

If the number of atoms in a trap is known, then the trap density and temperature can be found in a straightforward manner from an image of the trap. We work with quadrupole and Ioffe traps in this experiment, hence there are two cases to consider.

### Case 1: Quadrupole Traps

A quadrupole trap provides a potential well with a linear gradient for the trapped atoms. Near the origin, the magnetic field can be expressed in the following form:

$$\mathbf{B}(x,y,z) = \left(-\frac{B_z'}{2}x\right)\mathbf{e}_x + \left(-\frac{B_z'}{2}y\right)\mathbf{e}_y + \left(B_z' z\right)\mathbf{e}_z.$$

An atom with total angular momentum $\mathbf{F}$ has a magnetic moment of

$$\boldsymbol{\mu}_F = -\mu_B g_F \mathbf{F},$$

and magnetic potential energy of $-\boldsymbol{\mu}_F \cdot \mathbf{B}$. Weak-field seeking atoms have $\boldsymbol{\mu}_F$ antiparallel to $\mathbf{B}$, so

$$-\boldsymbol{\mu}_F \cdot \mathbf{B} = \mu_B g_F m_F B,$$

where all quantities represent magnitudes. Since gravity plays an important role in trapped atom dynamics, the total potential energy of atoms in a quadrupole trap is

$$U(\mathbf{r}) = \frac{1}{2}\mu_B g_F m_F \left|B_z'\right| \sqrt{\rho^2 + 4z^2} + mgz.$$

A classical gas of trapped atoms in equilibrium has a density profile that varies exponentially as the potential energy:

$$n(\mathbf{r}) = n_0 e^{-U(\mathbf{r})/k_B T}.$$

The peak density $n_0$ can be found by normalizing the density to the total number of atoms in the trap:

$$N = \int n(\mathbf{r})\, d\mathbf{r} = 2\pi n_0 \int_{z=-\infty}^{z=+\infty} dz\, e^{-mgz/k_b T} \int_{\rho=0}^{\rho=\infty} e^{-\alpha\sqrt{\rho^2+4z^2}}\, \rho\, d\rho,$$

with $\alpha = \frac{\mu_B g_F m_F |B'_z|}{2k_B T}$. After performing the integrations one obtains

$$n(\mathbf{r}) = n_0 e^{-(\alpha\sqrt{\rho^2+4z^2}+mgz/k_BT)},$$

with

$$n_0 = \frac{N}{64\pi\alpha}\left[4\alpha^2 - (\frac{mg}{k_BT})^2\right].$$

With the density known, a useful expression for fitting trap images can be derived. Our CCD camera system captures light from the trap in a direction perpendicular to the z-axis of the quadrupole coils. Arbitrarily denoting this axis as the y-axis, our camera sees an intensity $I(x,z)$ proportional to

$$\begin{aligned} I(x,z) &\approx \int n(\mathbf{r})\,dy = n_0 \int_{-\infty}^{+\infty} dy\, e^{-(\alpha\sqrt{\rho^2+4z^2}+mgz/k_BT)} \\ &= 2n_0 e^{-mgz/k_BT} \int_0^{\infty} dy\, e^{-\alpha\sqrt{x^2+y^2+4z^2}}. \end{aligned}$$

If the substitution $t^2 = x^2 + y^2 + z^2$ is made, the integral can be reduced to

$$I(x,z) \approx 2n_0 e^{-mgz/k_BT} \int_{\sqrt{x^2+4z^2}}^{\infty} \frac{te^{-\alpha t}}{\sqrt{t^2-(x^2+4z^2)}}.$$

This integral is of the form

$$\int_u^{\infty} dx \frac{xe^{-\alpha x}}{\sqrt{x^2-u^2}} = uK_1(\alpha u),$$

where $u > 0$ , $\mathrm{Re}\,\alpha > 0$, and $K_1$ is the modified Bessel function of integer order [39]. The intensity profile becomes

$$I(x,z) \approx 2n_0 e^{-mgz/k_BT}\sqrt{x^2+4z^2}K_1(\alpha\sqrt{x^2+4z^2}),$$

or, expressed in terms of physical quantities,

$$I(x,z) \approx \frac{N}{(k_BT)^3}\frac{\left[(\mu_B g_F m_F |B'_z|)^2 - (mg)^2\right]}{16\pi\mu_B g_F m_F\,|B'_z|} e^{-mgz/k_BT}\sqrt{x^2+4z^2} \times$$

$$K_1\left[\frac{\mu_B g_F m_F|B_z'|}{2k_B T}\sqrt{x^2+4z^2}\right].$$

This expression represents a quadrupole trap image centered at the origin. Unfortunately, the origin of the image profile (the exact pixel coordinates) is not known before an image is taken by the CCD camera. In addition, the most convenient origin for video images is not at the center of the screen, but in the upper left corner of the screen, with the x axis horizontal and the positive z axis oriented downwards. Denoting the video coordinates by $(\tilde{x},\tilde{z})$ and letting the center of the image be at video coordinates $(a_{3,}a_4)$, the transformation between the two coordinate systems is:

$$\begin{aligned} x &= \tilde{x}-a_3 \\ z &= a_4-\tilde{z}. \end{aligned}$$

Making this substitution in the above expression for $I(x,z)$, one obtains

$$\begin{aligned} I(x,z) \approx{} & \frac{N}{(k_BT)^3}\frac{\left[(\mu_B g_F m_F|B_z'|)^2-(mg)^2\right]}{16\pi\mu_B g_F m_F\,|B_z'|}e^{-mg(a_4-\tilde{z})/k_BT}\sqrt{(\tilde{x}-a_3)^2+4(a_4-\tilde{z})^2}\,\cdot \\ & K_1\left[\frac{\mu_B g_F m_F|B_z'|}{2k_BT}\sqrt{(\tilde{x}-a_3)^2+4(a_4-\tilde{z})^2}\right]. \end{aligned}$$

This expression is now in a form that is suitable for fitting. Extracting the constants into fit parameters $a_{1,}$ $a_2$ and $a_5$ results in

$$\begin{aligned} I_{fit}(\tilde{x},\tilde{z};\mathbf{a}) ={} & a_1e^{-a_2(a_4-\tilde{z})}\sqrt{(\tilde{x}-a_3)^2+4(a_4-\tilde{z})^2}\,\times \\ & K_1\left[a_5\sqrt{(\tilde{x}-a_3)^2+4(a_4-\tilde{z})^2}\right]+a_6. \end{aligned}$$

This is a function of the variables $\tilde{x}$ and $\tilde{z}$ with six adjustable fit parameters $a_1\cdots a_6$. Parameters $a_1$, $a_2$, and $a_5$ are not completely independent, since the temperature $T$ is common between them. Obviously, this is a complicated function, and a nonlinear method is required to fit an actual trap image to it. The general procedure for problems such as this is to define a figure of merit $\chi^2(\mathbf{a})$ and globally minimize it over the space of the variables $a_1 \cdots a_6$. Press *et al.* [40] provide a one-dimensional Levenberg-Marquardt method for performing such fits; we have modified their method to handle the multidimensional case. Denoting the actual image pixel value at $(\tilde{x}_i, \tilde{z}_i)$ by $I(\tilde{x}_i, \tilde{z}_i)$, our $\chi^2$ merit function is

$$\chi^2(\mathbf{a}) = \sum_{i=1}^{N} [I(\tilde{x}_i, \tilde{z}_i) - I_{fit}(\tilde{x}_i, \tilde{z}_i; \mathbf{a})]$$

which is iteratively minimized over the **a** parameters.

With the **a** parameters determined, the trap temperature can be found by choosing parameter $a_5$ (which is equal to the parameter $\alpha$ above), setting its value equal to that from the fit, and solving for $T$.

### Case 2: Ioffe Traps

The Ioffe trap provides a harmonic potential well and thus gaussian density and image profiles. In contrast to the case of the quadrupole trap, the density of an Ioffe trap can be determined without first having to find the temperature. Choosing this form for the density

$$n(x, y, z) = n_0 e^{-x^2/\sigma_x^2} e^{-y^2/\sigma_y^2} e^{-z^2/\sigma_z^2},$$

a normalization to $N$, the total number of atoms in the trap, results in this expression for the peak density:

$$n_0 = \frac{N/\pi^{\frac{3}{2}}}{\sigma_x \sigma_y \sigma_z}.$$

Our Ioffe traps are radially symmetric, so $\sigma_x = \sigma_y = \sigma_r$, giving

$$n_0 = \frac{N/\pi^{\frac{3}{2}}}{\sigma_r^2 \sigma_z}.$$

To determine the widths $\sigma_r$ and $\sigma_z$, a generic gaussian function is used (the y-dimension having been integrated out):

$$I_{fit}(\tilde{x}, \tilde{z}; \mathbf{a}) = a_1 e^{-\left(\frac{\tilde{x}-a_2}{a_3}\right)^2} e^{-\left(\frac{\tilde{z}-a_4}{a_5}\right)}.$$

As with the quadrupole fits, a $\chi^2$ figure of merit is iteratively minimized over the $\mathbf{a}$ parameters. The radial width $\sigma_r$ is set equal to the fit parameter $a_3$, and the z-width $\sigma_z$ is equal to the fit parameter $a_5$.

To determine the actual temperature of the Ioffe trap, it is necessary to relate the $\sigma$ parameters to actual physical quantities. For this an explicit expression for the trapping potential is needed. The magnetic part of the potential $U_B(\mathbf{r}) = -\boldsymbol{\mu} \cdot \mathbf{B}(\mathbf{r})$ requires knowledge of the magnetic field. Near the origin of the trap, equation 2.4 provides a convenient expression for the field magnitude:

$$B = B_0 + \beta z^2 + \frac{1}{2}\left(\frac{\alpha^2}{B_0} - \beta\right)\rho^2.$$

This expression is valid for an Ioffe trap in a gravity-free region of space. The general effect of gravity on these traps is to cause the trap to "sag", or to be displaced downward from the gravity-free equilibrium position. This sagging effect distorts the atom distribution and complicates the analysis of trap images. Typically, a weak gradient is added to the Ioffe field to counteract gravitational effects and to restore symmetry to the traps. The actual field gradient required, though, depends on the $g$-factor and $m$-state of the atom. For cesium atoms in the $F = 4$, $m_F = 4$ state, a simple calculation indicates that the required gradient $G_z$ is $-23$ G cm$^{-1}$. Including this term along with the gravitational potential yields an expression for the potential energy of an atom in an Ioffe trap:

$$U(\mathbf{r}) = \mu B_0 + \mu\beta z^2 + \frac{\mu}{2}\left(\frac{\alpha^2}{B_0} - \beta\right)\rho^2 + \mu G_z z + mgz.$$

For the calculations that follow it is helpful to change variables and eliminate some terms in this potential. If these definitions are made:

$$\begin{aligned} U_0 &= \mu B_0 \\ A &= \frac{\mu}{2}\left(\frac{\alpha^2}{B_0} - \beta\right) \\ C &= \mu\beta \end{aligned}$$

$$D = mg + \mu G_z,$$

then the potential can be expressed as

$$U(\mathbf{r}) = U_0 + A\rho^2 + Cz^2 + Dz.$$

The last term represents a constant force, which only has the effect of redefining the equilibrium position to $z_{eq} = -D/2C$. If a change of variables is made to $\tilde{z} = z - z_{eq}$, the potential becomes, after discarding non-essential constant terms,

$$U(\mathbf{r}) = A\rho^2 + C\tilde{z}^2.$$

With the known constants $A$ and $C$, the $\sigma$ parameters can be related to the physical aspects of the trap. To do this, the density can be expressed as:

$$n(\mathbf{r}) = n_0 e^{U(\mathbf{r})/k_B T} = n_0 e^{-\tilde{C}z^2 + \tilde{A}\left(x^2+y^2\right)},$$

where $\tilde{C} = C/k_B T$, $\tilde{A} = A/k_B T$. From this expression, it is evident that

$$\begin{aligned} \frac{1}{\sigma_z^2} &= \tilde{C} = \frac{\mu\beta}{k_B T} \\ \frac{1}{\sigma_r^2} &= \tilde{A} = \frac{\frac{\mu}{2}\left(\frac{\alpha^2}{B_0} - \beta\right)}{k_B T}, \end{aligned}$$

relations that yield the trap temperature if the widths $\sigma_r$ and $\sigma_z$ can be determined from fits to a trap image.

# Chapter 5 Quadrupole Trap Experiments

## 5.1 Introduction

This chapter presents an overview of three of the quadrupole trap experiments performed with this system. The first experiment to be described is the measurement of magnetostatic trap lifetimes. Lifetimes up to 4000 seconds were measured, representing the longest-lived magnetostatic traps ever observed. The next experiment is concerned with the trapping of a single atom. An unambiguous signal of one and two atom traps was observed, and live video images of single and few atom traps were obtained. The final experiment is concerned with the stability of MOTs at high field gradients. This experiment was important for its role in identifying some fundamental MOT properties, and it led to the identification of stochastic diffusion as the dominant atom loss mechanism for MOTs in high fields.

## 5.2 Lifetime Measurements

The measurements of quadrupole magnetostatic trap lifetimes proceeded as follows. First, cesium atoms were loaded directly from an atomic beam and collected in a MOT with a gradient of 10 G cm$^{-1}$. No slower was used for this experiment, since it was not necessary to maximize the number of atoms captured. During the loading process, a photodiode monitored the trap fluorescence. The trap was considered to be fully loaded when the photodiode voltage stopped rising and leveled off.

After the completion of trap loading, the gradient of the quadrupole coils was jumped to a higher value. For the data to be presented, the final gradients were 50 G cm$^{-1}$ and 1500 G cm$^{-1}$. A few milliseconds before the jump, the MOT laser beams (trapping and repumper) and the atomic beam were shuttered closed, resulting in the transfer of atoms to the magnetostatic quadrupole trap. Assuming the MOT atoms

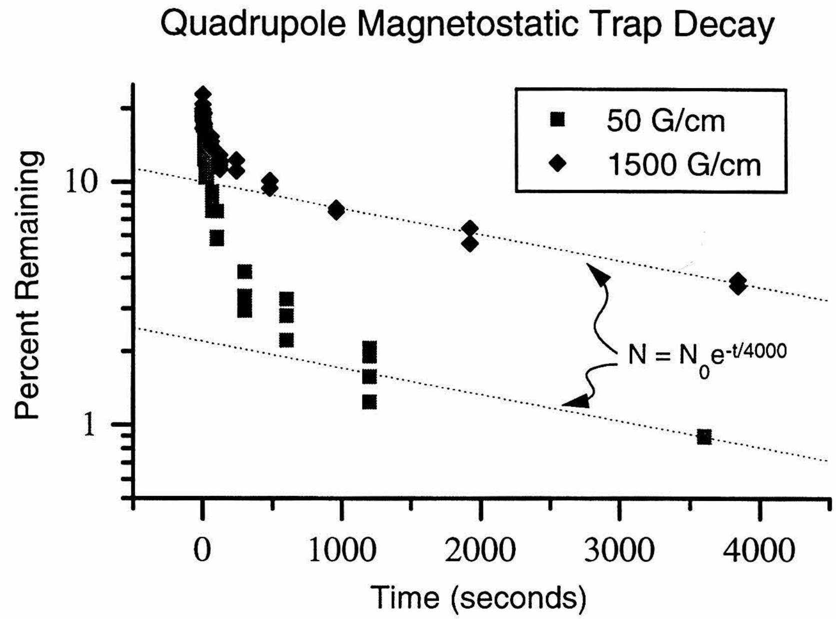

Figure 5.1: Quadrupole MST decay curves.

to be equally distributed amongst the $2\times4+1$ m-states of the $F = 4$ manifold, the transfer process resulted in the capture of 4/9 of the atoms in the MST.

After ramping the fields of the MST, the MST was held for a variable length of time before re-forming the MOT and recording the photodiode voltage. The hold time varied from 1 second to over an hour. The 1 second time was used as a baseline for comparisons with later times, and it also helped reduce initial loading variations. A plot of the data obtained is presented in figure 5.1.

From this figure it can be seen that the background losses cause the traps to decay exponentially in time, with a time constant of 4000 seconds. This represents the longest trap lifetime ever measured. Also, the time constant is independent of the field gradient, as it should be for background gas collisions. From the collisional calculations presented in [28], the time constant of 4000 seconds places an upper limit to the pressure in the trapping chamber of $3 \times 10^{-13}$ torr.

One further aspect of this graph deserves mention. The trap decay initially is not exponential. After much consideration of various explanations, it seems that the initial fast decay is due to the gradual pressure decrease in the trapping chamber. Immediately after the MST is formed, the pressure in the inner chamber is higher than at later times, since the atomic beam has just been shuttered closed, and any residual cesium has not yet had sufficient time to cryopump away. After about 500 seconds, the residual background gas is finally pumped away, and the curve goes over into an exponential.

## 5.3 Single Atom Traps

Magneto-optical traps with few atoms are worthy of study for a number of reasons. First, at high field gradients (on the order of 1 kG $\mathrm{cm}^{-1}$), all MOTs naturally have few atoms. The extreme compressions characteristic of this regime lead to collision processes varying as the square of the density becoming the dominant mechanism for atom loss. At lower compressions, the $n^2$ loss processes are too weak, and are masked by background losses. Thus, questions such as the stability of a two-atom MOT to elastic collisions become meaningful.

Furthermore, a single trapped atom provides an interesting system for studying fundamental processes in quantum optics. For instance, it is well-known that the resonance fluorescence from a single atom is drastically modified if the excitation is provided by nonclassical light [41]. The frequency width of the fluorescence can be greater or less than that of scattered classical light, depending on the bandwidth of the incident squeezed light. The scattered light can also exhibit bunching or antibunching, depending on the characteristics of the excitation. For all these reasons, the pursuit of single-atom and few-atom MOTs is a worthwhile goal.

The work to be reported represents a considerable improvement over that previously published. The first evidence of single atom trapping was reported by Hu *et al.* [42]. Their experiment used a room-temperature vapor cell trap with an avalanche photodiode for fluorescence detection. The detection of single atom jumps in the fluorescence was somewhat obscured by the background fluorescence from the gas in the vapor cell. Furthermore, real-time imaging of single and few-atom MOTs was not possible, since an APD is not an imaging device.

Our experiment has overcome these difficulties, and it has yielded a clear and unambiguous signal of single-atom jumps in the trap fluorescence. This has been accomplished by using an extremely sensitive intensified CCD camera for photodetection. The properties of this camera have been described previously in the chapter on imaging.

This experiment was conducted as follows. First, since a single atom emits a total fluorescence power in the femtowatt range, it was necessary to eliminate all extraneous sources of light in the laboratory. All non-essential pieces of equipment were turned off, and all LEDs were taped over with opaque tape. All lasers and as much of the associated optics as possible were enclosed in opaque black plastic boxes; the sides of the boxes were then taped over with duct tape. An extensive system of baffles was constructed to thoroughly shield the trap from all possible sources of stray light, even those few photons scattering off air molecules in the path of the trap beams.

A MOT was loaded from the atomic beam, and the field gradient was ramped up to the kG $\text{cm}^{-1}$ range, as in the experiment of the previous section. The Gen-III intensifier on the CCD camera was turned up to its maximum gain setting, and, after a few seconds of trap decay, MOTs with one to several atoms were observed on the live video feed from the camera. A sensitive, highly amplified photodiode recorded the fluorescence from the trap, yielding a time series such as that in the next figure:

In this figure, a clear and unambiguous level structure to the fluorescence can be observed, indicating the presence of one, two, and three atom MOTs. The inset, representing a histogram of the observed fluorescence, makes this even more apparent.

The next figure is a three-dimensional representation of one and two-atom images obtained with the CCD camera. The signal to noise ratio is extremely high in these figures, attesting to the sensitivity of the imaging system used in this experiment.

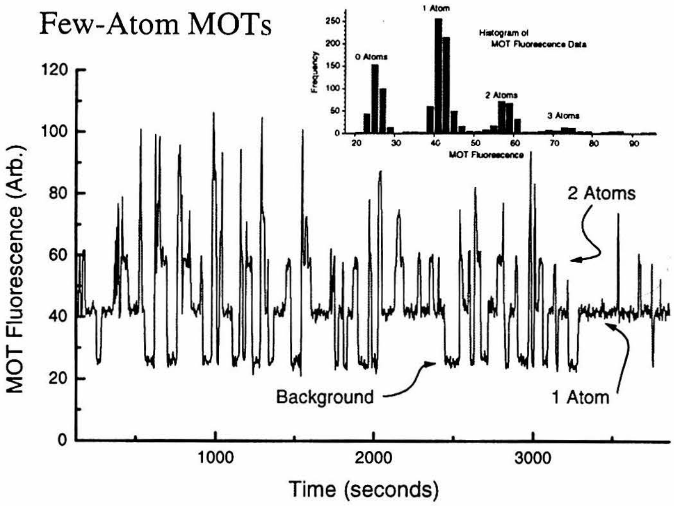

Figure 5.2: Evidence for single-atom MOTs.

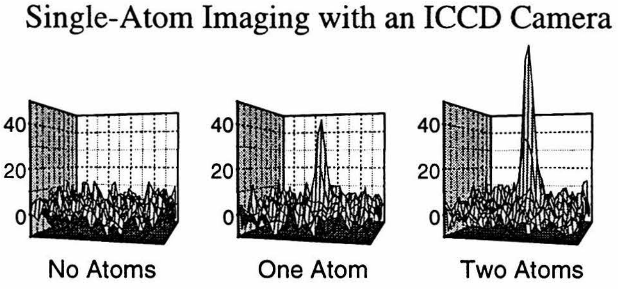

Image Resolution about 15 μm.

Figure 5.3: Representation of single-atom images.

## 5.4 Stability of High Field Gradient MOTs

The experiments reported in this section were concerned with measuring the limits of MOT stability with respect to laser intensity, detuning, and field gradient. A MOT was loaded in the manner described previously; the field gradient was then increased until only a single atom was left in the trap. After the appearance of a single atom, the field gradient was steadily increased until the atom was lost from the trap. For each set of values for the intensity, detuning, and maximum field gradient, multiple data points were taken and averaged.

A paper describing the results and modeling of this experiment has been published: the citation is *Physical Review Letters* **78**(9), 1660-1663, 1997. Detailed modeling of the experiment can be found in the doctoral thesis of Phil A. Willems [28]. Beginning on the following page, the paper is reproduced in its entirety.

## 5.5 Appendix to Chapter 5

# Stability of Magneto-Optical Traps with Large Field Gradients: Limits on the Tight Confinement of Single Atoms

P. A. WILLEMS[1], R. A. BOYD, J. L. BLISS, AND K. G. LIBBRECHT[2]

*Norman Bridge Laboratory of Physics, 12-33 California Institute of Technology, Pasadena, CA 91125*

**Abstract.** We report measurements of the stability of magneto-optical traps (MOTs) for neutral atoms in the limit of tight confinement of a single atom. For quadrupole magnetic field gradients at the trap center greater than $\sim$ 1 kG/cm, we find that stochastic diffusion of atoms out of the trapping volume becomes the dominant particle loss mechanism, ultimately limiting the MOT size to greater than $\sim$ 5 microns. We measured the diffusive loss rate as a function of laser power, detuning, and field gradient for trapped cesium atoms. The data are modeled with a phenomenological Fokker-Planck diffusion analysis with estimated trap pseudopotentials. In addition, for as few as two atoms the collisional loss rates become very high for tightly confined traps, allowing the direct observation of isolated 2-body atomic collisions in a MOT.

PACS numbers: 32.80.Pj, 39.10.+j

(Submitted to Phys. Rev. Letters 10/31/96)

The magneto-optical trap (MOT) [1] is a useful tool for producing large numbers of laser-cooled and trapped neutral atoms at sub-mK temperatures. Many recent experimental investigations of ultra-cold atomic collisions, atom optics and interferometry, and gaseous Bose-Einstein condensation have used MOTs as a first step in the preparation of cold atom samples. The MOT itself has been the focus of numerous studies, which have examined collective behavior from radiation trapping [2], collisional losses

---

[1] PRESENT ADDRESS: ARROYO OPTICS, 1646 17TH ST., SANTA MONICA, CA 90404

[2] ADDRESS CORRESPONDENCE TO *kgl@sundog.caltech.edu*

[3], and polarization-gradient cooling [4, 5] in MOTs. In this Letter we examine the potential for using MOTs to confine neutral atoms to small and well-defined regions of space. In this "tight confinement" limit one makes connection to investigations of quantum-limited atomic position measurements in optical fields [6], and in addition addresses the physical limits of magneto-optical lenses for focusing atomic beams [7]. The tightest possible confinement of small numbers of magneto-optically trapped radioactive atoms may also be desirable [8].

Because polarization-gradient cooling is quite effective in MOTs [4, 5], a significant reduction in trap size via improved cooling would require cooling below the single-photon recoil limit, which has not yet been realized in MOTs. The alternative for achieving tighter atom confinement is to increase the trap spring constant, which is expected to be proportional to magnetic field gradient [1]. We have found, using measurements of the dynamical behavior of trapped atoms, that for typical MOT parameters the spring constant is indeed linearly dependent on the quadrupole magnetic field gradient, up to axial gradients of at least $B' = dB_z/dz = 1.4$ kG/cm, while the damping constant remains independent of $B'$ [9]. Thus the trap size is expected to be proportional to $(B')^{-1/2}$. We identify here a new diffusive loss mechanism that ultimately limits the trap stability at high $B'$, and thus limits the degree to which neutral atoms can be stably confined in a MOT.

The stability of a MOT is determined by the different mechanisms that remove atoms from the trap. These can be parameterized by a trap population rate equation,

$$dN/dt = R - (\tau_{\text{back}}^{-1} + \tau_{\text{diff}}^{-1})N - \beta N(N-1)$$

where $N$ is the number of atoms in the trap, $R$ is the MOT loading rate, $\tau_{\text{back}}$ is the trap lifetime due to background collisions, $\beta$ arises from collisions between trapped atoms [10], and $\tau_{\text{diff}}$ is the mean time for diffusion of atoms out of the trapping volume. Each of the parameters in turn depends on the characteristics of the MOT, such as the laser intensity, detuning from the atomic resonance, beam size, and the quadrupole field gradient. The parameters also depend on $N$ when $N$ is large, owing to collective effects between atoms [2].

Our experimental investigations of tightly confined MOTs were performed in a vacuum chamber cooled to below 4K, inside of which MOTs were formed [11]. With this system we could produce high quadrupole field gradients using superconducting magnetic field coils, while background collisional losses gave $\tau_{\mathrm{back}} \approx 1$ hour. A copper shutter at 4K in the side of the chamber admitted a 450K thermal cesium beam to load atoms into the MOTs. An intensified CCD camera provided sufficient sensitivity that fluorescence from single atoms could be observed on a live video image [12].

Figure 1 shows a measurement of the average residence time $\langle\tau\rangle$ for atoms in a MOT, as a function of $B'$, for a single laser intensity and detuning. This was determined by forming a stable MOT and then measuring the average time before the atom(s) escaped. For trap populations as small as $N = 2$, collisional losses dominate over other loss mechanisms as $B'$ is increased; these losses are consistent with typical collisional loss rates in MOTs [3]. Furthermore, we found that a high-field-gradient MOT with two atoms almost always decayed to an empty MOT, which we interpret as the direct observation of isolated two-body collisions between trapped atoms.

For single-atom MOTs the trap loss at high $B'$ was dominated by stochastic diffusion of the atom out of the MOT capture volume. To examine the behavior of the diffusive loss-rate parameter $\tau_{\mathrm{diff}}$ as a function of laser intensity and detuning, we first loaded several atoms into the MOT, increased $B'$ until one atom remained, then continued to increase $B'$ until the atom was observed to leave the trap, with $dB'/dt$ such to give $\langle\tau\rangle \approx \tau_{\mathrm{diff}} \approx 1$ sec). This procedure was repeated several times to check reproducibility, giving a measure of the field gradient $B'$ for which $\tau_{\mathrm{diff}} \approx 1$ sec. Figure 2 shows these measurements over a range of laser intensities and detunings.

To model the single-atom MOT data in Figures 1 and 2 we calculate the behavior of the diffusive loss coefficient $\tau_{\mathrm{diff}}$ using a 1-D Fokker-Planck diffusion model. We first make the simplifying assumption that the atomic motion in the MOT is everywhere strongly overdamped. Dynamical studies of MOTs have shown that this assumption is justified at least near the trap center, even for large laser intensities and large $B'$, due to the effects of polarization-gradient cooling [9, 14]. With this assumption the

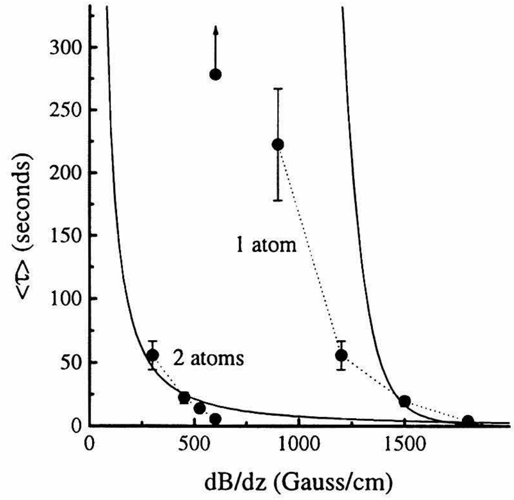

Figure 5.4: Average residence time for one and two cesium atoms in a MOT.

Fokker-Planck equation reduces to the Smoluchowski equation [15], and the rate for diffusion of atoms out of the trap is given by

$$\tau_{\text{diff}}^{-1} = \left(\frac{\kappa k_B T}{2\pi\alpha^2}\right)^{1/2} \Big/ \int_0^b e^{U(z)/k_B T} dz$$

where $\alpha$ is the usual MOT damping coefficient (defined by damping force $F = -\alpha v$, where $v$ is the atom velocity), $\kappa$ is the spring constant at the trap center ($F = -\kappa z$), $T$ is the trap temperature, and $U(z)$ is the MOT pseudopotential ($U \approx \frac{1}{2}\kappa z^2$ near the trap origin). The 1-D equation suffices for this because the 3-D equation separates, and in Monte-Carlo simulations we find that atoms always diffuse out of the trap along the axial direction (which is the most tightly confining). The integral is from $z = 0$, the trap center, to $z = b$, the point at which atoms are no longer confined by the trap. We can approximate the integrand by $U(z) \approx -\kappa b^2/2 + \kappa bz$, which is an

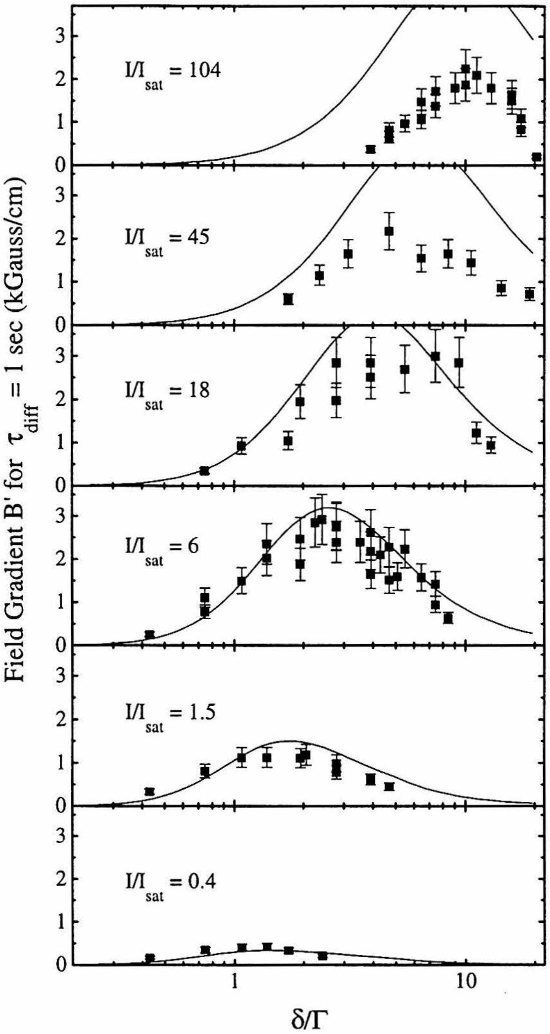

Figure 5.5: MOT stability data.

expansion about $z = b$, giving the analytic expression

$$\tau_{\text{diff}}^{-1} \approx \frac{1}{\sqrt{\pi}} \frac{\kappa}{\alpha} \left( \frac{\kappa b^2}{2k_B T} \right)^{1/2} e^{-\kappa b^2/2k_B T}.$$

Evaluation of this expression requires knowledge of two quantities, the MOT relaxation time $\tau_{\text{relax}} \equiv \alpha/\kappa$, and the ratio of the overall trap depth $U_0 \approx \frac{1}{2}\kappa b^2$ to the trap temperature $T$. To model our data these must be given as a function of laser intensity $I$ and detuning $\delta$, and as a function of field gradient $B'$. Our theoretical understanding of these parameters is unfortunately incomplete, due in part to complications of sub-Doppler cooling mechanisms present for atoms possessing several nearly degenerate magnetic sub-levels, and generalization of 1-D theories to 3-D MOTs. Theory is particularly uncertain at high laser intensity $I/I_{sat} \gg 1$, which applies for much of the data in Figure 2, and for non-zero magnetic fields, such as are present at the edge of a MOT.

In spite of these theoretical uncertainties, we can nevertheless make crude analytical estimates of the parameters in the above expression for $\tau_{\text{diff}}^{-1}$, guided by recent measurements of MOT dynamics. The purpose of this is twofold: to test that the lifetime data in Figure 2 are indeed consistent with our underlying hypothesis of diffusive loss, and to model the minimum attainable MOT size. The latter is relevant in regard to magneto-optical focusing of atomic beams.

The MOT relaxation time $\tau_{\text{relax}}$ can be readily measured through observations of the motion of atoms trapped in a MOT, for example by displacing the trap and observing its relaxation to equilibrium. Such measurements give values of $\tau_{\text{relax}}$ that are about 10× larger than predicted by 1-D sub-Doppler theory, and show an unexpected linear dependence on detuning $\delta$ [5]. Our own dynamical measurements using cesium [9] give $\tau_{\text{relax}}/(1\,\text{sec}) \approx (0.03\ \text{G/cm})(2\delta/\Gamma B')$, where $\Gamma$ is the natural linewidth of the transition, independent of intensity for $1 < I/I_{sat} < 15$ (for cesium $\Gamma = 2\pi \times 5.2$ MHz and $I_{sat} = 1.1\ \text{mW/cm}^2$).

The relative trap depth $U_0/k_B T$ is the most difficult parameter in the above expression to model theoretically, since $U_0$ depends crucially on the behavior of the

MOT forces near the edge of the trap, where the Zeeman splitting is of the same order as the light shift of the ground state [19]. The transition from the low-field region near trap center, where polarization-gradient forces are in effect, to the strong-field region is particularly problematic. Measurements of typical values of $U_0$ have been made using a pulsed disturbance [1] and using catalyzed cold collisions [16], but a systematic study measuring $U_0$ as a function of $I$, $\delta$, and $B'$ has not yet been performed. Taking $U_0 = \frac{1}{2}\kappa b^2$, however, we can proceed using phenomenological estimates of $T$, $\kappa$, and $b$ separately.

For low atom numbers, measurements of atom temperatures in MOTs are found to be identical with those measured in 3-D $\sigma^+ - \sigma^-$ optical molasses, which for low intensities and large detunings ($\delta/\Gamma > 5$) is given by $T \approx [2.6 + 60(\Gamma/2\delta)(I/I_{sat})]$ $\mu K$ for cesium [5]. At smaller detunings the temperature is larger than that given by this expression, in agreement with 3-D calculations [20]; in this region ($\delta/\Gamma < 5$) the extrapolation $T \approx [260(\Gamma/2\delta)^2 + 60(\Gamma/2\delta)(I/I_{sat})]$ $\mu K$ describes temperature data adequately for our model.

The spring constant can be calculated using 1-D sub-Doppler theory, giving $\kappa \approx A\mu_B B' k(2\delta/\Gamma)/[1 + (2\delta/\Gamma)^2]$ [4, 2, 17], where $A$ is a constant depending on atomic parameters. A number of measurements of the spring constant $\kappa$ have been made [5, 4, 17, 9], with the result that the 1-D theory gives roughly the correct functional form (over the limited intensity range approximately $0.4 < I/I_{sat} < 4$), but overestimates the magnitude of $\kappa$ by about an order of magnitude. For cesium we find empirically that $A \approx 0.10 \pm 0.03$.

Semiclassical and quantum calculations have shown for large detuning that the boundary between the central and outer regions of a (two-component) MOT occurs at the radius $b \approx \eta(I/I_{sat})(\hbar\Gamma/\mu B')(\Gamma/2\delta)$, where $\eta$ is a numerical factor near unity [19]. At this radius the light-shift of the atomic ground state equals the Zeeman shift, and the MOT restoring force reaches a local maximum. Beyond this radius the restoring force falls rapidly, and the effective temperature increases due to the suppression of sub-Doppler cooling mechanisms. Thus for a very tightly confined MOT we expect rapid diffusion of atoms out of the MOT beyond this radius.

Evaluating $\tau_{\text{diff}}^{-1}$ using the above estimates for $\tau_{\text{relax}}$, $T$, $\kappa$, and $b$, gives an adequate fit to our data at low intensities, where sub-Doppler theory and the MOT dynamical data are reasonably secure, but grossly overestimates the trap stability ($\tau_{\text{diff,calc}} \gg \tau_{\text{diff,observed}}$) at higher intensities. This discrepancy is not surprising, since the sub-Doppler theory is known to break down at high laser intensities. We find, however, that if we add an *ad hoc* high-intensity roll-off to $U_0$, for example taking $b = \eta(I/I_{sat})(\hbar\Gamma/\mu B')(2\delta/\Gamma)/(1+6I/I_{sat}+(2\delta/\Gamma)^2)$, (which equals the above expression for $b$ in the limit of low intensity and large detuning), we obtain a fairly good fit to the data, shown in Figure 2. Note the prefactor $\eta$ serves as a scaling factor in Figure 2, and is adjusted to fit the low-intensity data. Additional measurements of $U_0$ and $\kappa$ at high laser intensities, or a more reliable theoretical model of MOTs in this region, are necessary to quantitatively reproduce our MOT stability data at the higher intensities.

The above phenomenological model can be used to estimate the minimum attainable MOT size. This question is of particular importance in regard to the ultimate physical limits in using 2-D MOTs for the tight focusing of neutral atomic beams. The smallest possible single-atom MOT can be formed by ramping up $B'$ quickly, realizing a transient tight confinement before the atom diffuses away. The trap's finite response time gives the smallest MOT when $\tau_{\text{diff}} \approx \tau_{\text{relax}}$, or equivalently $\kappa b^2/k_B T \approx 1$. Taking the trap radius as $\kappa z^2 \approx k_B T$, the minimum size is given by $z_{\text{min}}(\delta, I) \approx k_B T/\kappa_0 b_0$, where $\kappa_0 = \kappa/B'$ and $b_0 = bB'$. Assuming the same parameters used above to compute $\tau_{\text{diff}}^{-1}$ we find that $z_{\text{min}}(\delta, I)$ exhibits a broad minimum around $\delta/\Gamma \approx 2.5$, $I/I_{sat} \approx 3$, with a global minimum MOT size of $z_{\text{global min}} \approx 2.4$ microns. Note that the value of $z_{\text{global min}}$ depends only weakly on the details of our model; $z_{\text{global min}}$ is attained at moderate laser intensities, where the model is fairly secure, and is not sensitive to the form of high-intensity roll-off chosen. These results suggest that plain MOTs will not provide tight enough confinement to exhibit interesting fluorescence behavior, as has been observed with trapped ions [21].

We also attempted to make super-stable Hanle-effect MOTs by using rectified dipole forces, which for high laser intensities can exceed the usual MOT scattering forces [22]. With larger trap spring constants and trap temperatures that are comparable to regular MOTs, we expected to realize tighter atom confinement. We found, however, that with such traps the field gradients for which $\tau_{\text{diff}} = 1\,\text{sec}$ were always substantially lower (typically $B' < 100$ G/cm) than those for a normal $\sigma^{+} - \sigma^{-}$ MOT. This suggests that strong Hanle-type stimulated forces, although effective in 1-D, may not be effective in 3-D MOTs.

In summary, we examined magneto-optical traps in the "tight-confinement" limit, and have made the first measurements of the diffusive loss rate as a function of laser intensity and detuning, and MOT field gradient. The data are well modeled at low intensities using a simple phenomenological Fokker-Planck analysis, which supports our hypothesis that atom diffusion is the primary trap loss mechanism in the limit of tight confinement. Extending the model with the addition of an *ad hoc* high-intensity roll-off, we find a minimum transient MOT size of $\sim$ 5 microns, a robust result which is insensitive to the model details. These results apply to generic MOTs, with random (and fluctuating) phases of the different laser beams; further investigation of tight MOTs using phase-stable trapping lasers may be quite interesting, potentially leading to controlled sub-micron atom trapping in a single optical lattice site.

This research was supported in part by funding from Millard and Muriel Jacobs, and the California Institute of Technology.

# Bibliography

[1] E. L. Raab, M. Prentiss, A. Cable, S. Chu, and D. E. Pritchard, Phys. Rev. Lett. **59,** 2631 (1987).

[2] T. Walker, D. Sesko, and C. Wieman, Phys. Rev. Lett. **64,** 408 (1990); A. M. Steane, M. Chowdhury, and C. J. Foot, J. Opt. Soc. Am. B **9,** 2142 (1992); W. Ketterle *et al.*, Phys. Rev. Lett. **70,** 2253 (1993); C. G. Townsend *et al.*, Phys. Rev. A **53,** 1702 (1996).

[3] D. Sesko *et al.*, Phys. Rev. Lett. **63,** 961 (1989); M. H. Anderson *et al.*, Phys. Rev. A **50,** R3597 (1994).

[4] A. M. Steane and C. J. Foot, Europhys. Lett. **14,** 231 (1991); C. J. Cooper *et al.*, Europhys. Lett **28,** 397 (1994).

[5] M. Drewson *et al.*, Appl. Phys. B **59**, 283 (1994).

[6] K. D. Stokes *et al.*, Phys. Rev. Lett. **67,** 1997 (1991); J. R. Gardner, M. L. Marable, G. R. Welch, and J. E. Thomas, Phys. Rev. Lett. **70,** 3404 (1993); P. Storey, M. Collett, and D. Walls, Phys. Rev. A **47**, 405 (1993); S. Kunze, G. Rempe, and M. Wilkens, Europhys. Lett. **27**, 115 (1994).

[7] J. Nellessen, J. Werner, and W. Ertmer, Opt. Commun.**78**, 300 (1990); E. Riis, D. Weiss, K. Moler, and S. Chu, Phys. Rev. Lett. **64**, 1658 (1990).

[8] G. Gwinner *et al.*, Phys. Rev. Lett. **72**, 3795 (1994); Z-T. Lu *et al.,* Phys. Rev. Lett. **72**, 3791 (1994).

[9] P. A. Willems, Ph.D. thesis, California Institute of Technology, 1997; P. A. Willems, R. A. Boyd, J. L. Bliss, and K. G. Libbrecht, *in preparation.*

[10] Collisional loss is usually parameterized in terms of the decay of the average atom density $\dot{n} = -\beta^* n^2$, which is a more suitable notation when $N$ is large; these are related by $\beta = \beta^*/V$, where $V$ is the effective volume of the trapped atoms. For small $N$, $\beta$ is independent of $N$.

[11] P. A. Willems and K. G. Libbrecht, Phys. Rev. A **51**, 1403 (1995). For the present investigations a new and larger version of this system was used.

[12] Single atoms in MOTs have been observed previously by: Z. Hu and H. J. Kimble, Optics Lett. **19**, 1888 (1994); F. Ruschewitz *et al.*, Europhys. Lett. **34,** 651 (1996); D. Haubrich *et al.,* Europhys. Lett. **34**, 663 (1996).

[13] The collisional decay curve was generated by extrapolating the density from measurements at low $B'$, assuming $n \propto N \cdot (B')^{3/2}$. At high $B'$ the collisional loss rate increases as the trap depth decreases, which explains the observed discrepancy in the 2-atom lifetime in Figure 1 at large $B'$. The 1-atom lifetime at low $B'$ is limited by loss mechanisms other than diffusion.

[14] P. Kohns *et al.*, Europhys. Lett **22**, 517 (1993).

[15] S. Chandrasekhar, Rev. Mod. Phys. **15**, 1 (1943).

[16] D. Hoffmann, S. Bali, and T. Walker, Phys. Rev. A **54,** R1030 (1996).

[17] C. D. Wallace *et al.*, J. Opt. Soc. Am. B **11**, 703 (1994).

[18] P. D. Lett *et al.*, J. Opt. Soc. Am. B **6**, 2084 (1989).

[19] C. G. Townsend et al., Phys Rev. A **52**, 1423 (1995).

[20] K. Mølmer, Phys. Rev. A **44**, 5820 (1991).

[21] R. G. DeVoe and R. G. Brewer, Phys. Rev. Lett. **76**, 2049 (1996).

[22] R. Grimm *et al.*, J. Phys. II **2**, 593 (1992); O. Emile *et al.*, Europhys. Lett. **20**, 687 (1992). Our trap configuration was the same as the latter reference, with the same polarization precision.

# Chapter 6 Cross-Section Measurements

## 6.1 Introduction

A gas of trapped atoms is driven towards thermal equilibrium by collisions. At the low temperatures characteristic of magnetostatic traps the collisions are predominantly s-wave, meaning that the scattering can be characterized by a single quantity, the s-wave scattering length $a$. The magnitude of $a$ determines the cross section through the relation

$$\sigma \approx \frac{8\pi a^2}{1+k^2a^2}, \tag{6.1}$$

where k is the wavevector of the incident atom [43]. The sign of $a$ is also of critical importance, for it determines whether the interatomic interactions are attractive or repulsive. Attractive interactions have $a < 0$, and repulsive interactions have $a > 0$.

There is an implied temperature dependence in the above equation, since the wavevector is dependent on the collision energy. An estimate of the temperature dependence can be obtained from simple considerations. An atom in the trap with momentum $p = \hbar k$ has, on average, a kinetic energy equal to $\frac{3}{2}k_BT$, or

$$\frac{p^2}{2m} = \frac{\hbar^2k^2}{2m} = \frac{3}{2}k_BT,$$

which implies that

$$k^2 = \frac{3mk_BT}{\hbar^2}.$$

This gives $\sigma$ the following form:

$$\sigma \approx \frac{8\pi a^2}{1+\frac{3mk_BT}{\hbar^2}a^2}, \tag{6.2}$$

showing that the cross section has a $1/T$ temperature dependence. This expression also shows that the product $ma^2$ determines the relative importance of the temperature-dependent term in the denominator. For a cesium atom in the $|4,4\rangle$ state, based on measurements of $a$ by Chu and collaborators [3], the product $ma^2$ is predicted to be a factor of 7 greater than that for rubidium and a factor of 27 greater than that for sodium. In other words, the temperature dependence of $\sigma$ will manifest itself to a greater extent in cesium than in the other alkali atoms. This effect further complicates attempts at evaporative cooling in cesium, since evaporation must begin at relatively high temperatures in highly compressed traps.

For most alkali atoms, the scattering length is a difficult quantity to calculate from first principles. It is extremely sensitive to the positions of the highest bound states of the interatomic potentials. In the case of cesium, these potentials are not known with sufficient accuracy to make definite predictions. Hence, measurements of the cross section are of great importance in determining the feasibility of evaporative cooling.

Prior to the work of this thesis, the only knowledge of the Cesium $|4,4\rangle$ on $|4,4\rangle$ cross section came from an *indirect* measurement in reference [3]. From measurements of frequency shifts in a Cesium fountain, these authors deduced the $T = 0$ s-wave cross section to lie somewhere in the range of $2.5 \times 10^{-11}$ cm$^2$ to $75 \times 10^{-11}$ cm$^2$. Even the lower bound of $2.5 \times 10^{-11}$ cm$^2$ represents an enormous value, a full order of magnitude greater than the cross section for the $|3,-3\rangle$ state of Cesium [44]. The attractiveness of the $|4,4\rangle$ state of Cesium for evaporative cooling should be apparent.

In this chapter, I present our measurements of trap equilibration processes that give an upper bound to the $|4,4\rangle$ on $|4,4\rangle$ cross section of $5.4 \times 10^{-13}$ cm$^2$ at a temperature of 260 $\mu$K. This value is approximately a factor of two smaller than the unitary limit for pure s-wave scattering at this temperature. However, d-wave contributions to the scattering are expected to manifest themselves at temperatures above 150 $\mu$K [45]. Our results demonstrate that there is no significant d-wave contribution up to a temperature of 260 $\mu$K.

## 6.2 Background

To measure a cross section, a sample of atoms must be prepared in a non-equilibrium state and then be allowed to equilibrate. The rate at which the trap approaches equilibrium is determined by the collision rate and hence by the collision cross-section. The initial state of disequilibrium is produced by forming a MOT and then transferring the atoms to a spin-polarized Ioffe trap in an imperfect manner. For this experiment, we use an Ioffe trap with field curvatures that produce non-optimal mode matching. This causes the radial and axial "temperatures" of the trap to be initially unequal. The inequality in the radial and axial temperatures can be exaggerated by varying the field curvatures (and hence trap frequencies) along the radial and axial directions. Many different traps were tried for this experiment; we selected the one that gave us the clearest signature of equilibration for the measurement.

Other methods for introducing disequilibrium were tried as well. Our initial method was to form a quadrupole trap and then rapidly push it upwards with the application of an external bias field. The sudden kick would cause the atoms in the trap to spray upwards, slosh around, and eventually settle back into equilibrium. The time evolution of the approach to equilibrium (via the changing aspect ratio of the atom cloud) could be monitored to yield a value of the cross section. This method was tried repeatedly over the course of several weeks, but the trap images so obtained were of poor quality, and the uncertainties and errors in the measurements swamped any signal. Hence the method of imperfect mode matching was used.

Since a trap with unequal radial and axial temperatures eventually equilibrates, there must be a rate $\Gamma_{mix}$ for redistribution of the trap's energy amongst the different dimensions. In the simplest approximation, the approach to equilibrium for any dimension $i = (x, y, z)$ is governed by Newton's law of cooling [45]:

$$dT_i/dt = \Gamma_{mix}\left(T_{av} - T_i\right)$$

where $T_{av} = \frac{1}{3}\Sigma_i T_i$ is the average temperature of the trap at time $t$. This average should remain constant as the equilibration progresses. This equation simply states that the rate at which a trap dimension equilibrates is proportional to how far out of equilibrium it is. In general, for any actual trap, there will be an additional heating term due to the presence of residual background gas or from the influence of any unblocked portions of the atomic beam. This heating rate is generally exponential in time with a rate $\Gamma_{heat}$. Hence the equation governing the equilibration of the trap becomes:

$$dT_i/dt = \Gamma_{heat} T_i + \Gamma_{mix}(T_{av} - T_i).$$

If the equation is divided through by $T_i$, then the following equation is obtained:

$$\frac{d \ln T_i}{dt} = \Gamma_{heat} + s_i \Gamma_{mix}, \tag{6.3}$$

where $s_i = (T_{av} - T_i)/T_i$, the "mixing sensitivity" of the $i^{th}$ dimension. From this equation, it is evident that $\Gamma_{mix}$ can be obtained by plotting the left-hand side of the above equation vs. the $s_i$'s and taking the slope of the curve.

If the mixing rate $\Gamma_{mix}$ is known, then the elastic collision rate can be found easily. Many groups have shown that the collision rate $\Gamma$ is related to the mixing rate by the relationship $\Gamma = 2.7\Gamma_{mix}$ [19]. Thus by measuring the mixing rate the cross section can be determined from the relation

$$n\sigma v_r = \Gamma \tag{6.4}$$

where $n$ is the average density of the atom cloud, and $v_r$ is the relative speed of two atoms in the trap.

## 6.3 Experimental Procedure

The cross section measurements all begin with the formation of a slowed MOT at 10 G/cm and −15 MHz detuning. With these values of the field gradient and detuning we are able to collect approx. $5 \times 10^7$ atoms at a temperature of roughly 80 $\mu$K. After

MOT formation, the trapping laser is detuned $-46$ MHz to provide further cooling. After approx. 2 ms the trapping laser is then jumped to $-62$ MHz and its intensity reduced by a factor of 20 for polarization gradient cooling. Polarization gradient cooling continues for 3 ms, after which time the trap has a temperature of about 40 $\mu$K. After the polarization gradient cooling phase, the trapping laser is shuttered closed, and the atoms are optically pumped into the $|4,4\rangle$ state for 2 ms.

The atoms are optically pumped into the $|4,4\rangle$ state by a $\sigma^+$ polarized laser beam tuned to the $4-4'$ transition. A bias field of 10 G is used for the optical pumping. It was necessary to retroreflect the pumping beam in order to avoid blowing the atoms away from unbalanced radiation pressure. During the optical pumping, the repumper laser beam is left on to keep atoms out of the $F=3$ manifold. In addition, a $\sigma^+$ polarized repumper beam is introduced along the direction of the $|4,4\rangle$ beam to provide a polarized component to the repumping. In practice, we find that this beam has little effect on the overall optical pumping efficiency.

Immediately after optical pumping, the magnetic trap is loaded by turning on the Yin-Yang fields around the pumped atoms. As mentioned previously, the mode matching is performed in such a way as to induce temperature differences along the radial and axial directions of the trap. Once these differences are established in the magnetic trap (we typically wait one millisecond), a radio-frequency field is applied to the trap for 3 seconds. The purpose of the RF field is to strip away any non $|4,4\rangle$ state atoms that may remain in the trap due to imperfect optical pumping. We have observed that our traps undergo a gradual increase in their average temperatures if the RF is not applied. We interpret this heating as being due to the presence of weakly-bound $F=3$ atoms suffering glancing collisions with the colder $F=4$ atoms. When the RF is applied, we observe no such heating. On our best days, our optical pumping and subsequent capture efficiency is approx. 50 percent, comparable to that reported by Wieman's group in their $F=3$ cross section experiment [45].

Our optical pumping efficiency is limited by several factors. By far, the dominant factor is the additional heating caused by prolonged optical pumping. Each time a trapped atom absorbs a photon from the optical pumping beam and then spontaneously emits it, the atom gains the momentum of the emitted photon. Essentially, the atom does a random walk in space, much like atoms in an atomic beam do when they are slowed by a chirped slower. If the optical pumping were to continue indefinitely, the atoms would gain enough kinetic energy to exceed the depth of the trap and would be lost. Of course, the s-wave limit for scattering (approximately 150 $\mu$K for Cesium) would be exceeded much sooner. In practice we find that a pumping time of 2 ms with a beam of 0.75 mW cm$^{-2}$ intensity is sufficient to provide us with enough atoms to conduct our experiment and keep the trap temperature reasonably close to the s-wave limit.

Another source of optical pumping inefficiency is due to stress-induced birefringence in the windows of our apparatus. A material is birefringent if the index of refraction it presents to an incident optical field depends on the polarization of that field. Birefringent materials are disastrous to circularly polarized light because they introduce phase shifts between the two linearly polarized field components, causing the circular polarization to become elliptical. One way to avoid stress-induced birefringence is, obviously, to avoid putting any stress on critical windows. In our system, however, some degree of stress is unavoidable due to the thermal contraction of the windows on our cryosphere. Our optical pumping beam must pass through several windows on its way in and out of the chamber before being retroreflected; this causes some unavoidable degradation of our circular polarization.

After optically pumping the atoms to the $|4,4\rangle$ state, loading them into the Yin-Yang trap, and applying RF, we wait a variable amount of time before taking an image of the trap. The equilibration process can be studied by varying the time before the image is taken. At short times (5 seconds) we observe large temperature differences between the radial and axial directions, but at longer times (45 seconds), the temperatures are more nearly equal.

With the measured time dependence of the radial and axial widths, the temperatures can be extracted according to the expressions in chapter 4. Doing so produces the plot in figure 5.1.

In figure 5.1 the approach to equilibrium of the radial and axial temperatures

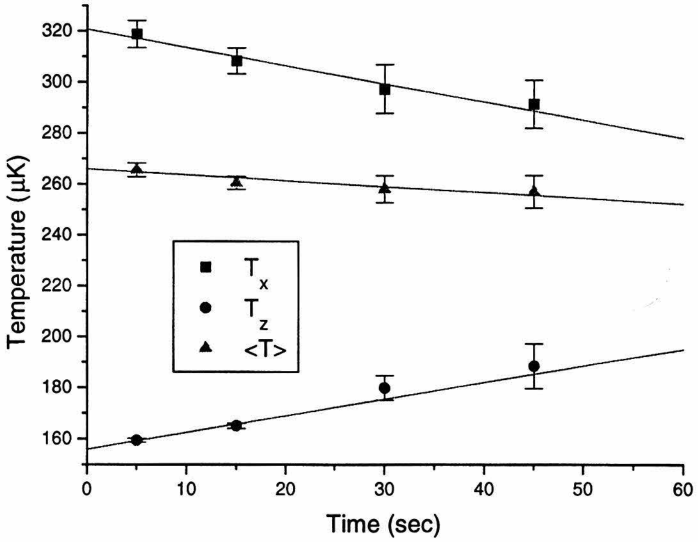

Figure 6.1: Evolution of radial and axial temperatures.

is plotted, along with the time dependence of the average temperature. Each point on the graph is the average of several runs; the size of the error bars reflects the scatter in the data. This plot clearly shows that the imperfect mode-matching used for this trap produced a gas in a high state of disequilibrium. As time increases, the radial and axial temperatures approach one another, indicating the system's progress towards equilibrium. Note also that the z-temperature (axial) grows faster than the x-temperature (radial). The reason for this is that the CCD camera could only see two dimensions of the trap. There is a y-dimension exchanging heat with the z-dimension, causing the axial width to rise faster than the x-width falls.

Knowledge of the temperatures yields the various mixing sensitivities $s_i$, enabling the value of $\Gamma_{mix}$ to be determined from equation 6.3. In figure 5.2 a plot of this equation for the axial temperatures is shown; a plot for the radial temperatures yields a comparable value for $\Gamma_{mix}$ and is therefore not displayed here. The slope of the line yields the following value for $\Gamma_{mix}$:

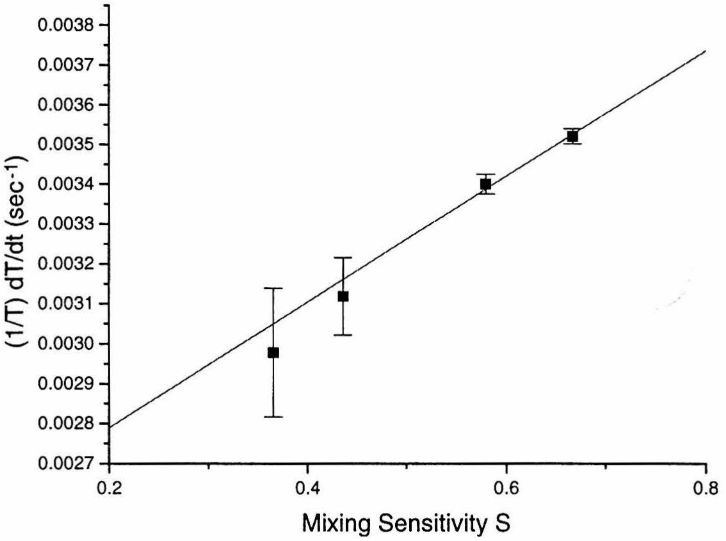

Figure 6.2: Energy evolution.

$$\Gamma_{mix} = (0.0016 \pm 0.0002)\ \text{sec}^{-1}.$$

With $\Gamma_{mix}$ known, the cross section can be found from equation 6.4. The peak density for this particular run was $n_0 = 10^9\ \text{cm}^{-3}$, yielding a trap-averaged density of $n_0/\sqrt{8} = 3.5 \times 10^8\ \text{cm}^{-3}$; the temperature of 260 $\mu$K yields a relative velocity of

$$v_r = \sqrt{\frac{16 k_B T}{\pi m}} = 28.8\ \text{cm s}^{-1},$$

assuming a Maxwellian distribution of atomic speeds. The error in our density measurement is conservatively estimated at 25%; this error is dominant when propagated through to the cross section expression. Putting all of these factors together yields our upper bound for the cross section at 260 $\mu$K:

$$\sigma = (4.3 \pm 1.1) \times 10^{-13}\ \text{cm}^2.$$

## 6.4 Discussion

Ideally, it would be useful to repeat these measurements, at the same temperature, but with the density low enough to preclude any signal of trap equilibration. This "low n" data would be useful for subtracting out any equilibration caused by trap anharmonicities or other non-collisional effects. We indeed made repeated attempts to obtain such low n data, but were unable to see any clear signal within the limits of our error bars. Hence, the value quoted above must be considered an absolute upper bound that includes *all* possible trap equilibration processes, not just collisional equilibration processes. If the number of atoms in the trap could be increased by an order of magnitude, both low n and high n data could be taken, and an actual value for the collisional cross section could be obtained.

This measurement is also meaningful for what it says about d-wave contributions to the scattering. At the 260 $\mu$K temperature of this experiment, it is intuitively clear that only the lower-order partial waves should contribute to the scattering. Each successive partial wave should make its presence felt when the energy of the colliding atoms is high enough to overcome the centrifugal barrier height for the given $l$-value. Since only even-order partial waves contribute to identical boson scattering, an expansion of the cross section into partial waves yields the following expression [46]:

$$\sigma = \frac{8\pi}{k^2} \sum_{l\ even} (2l+1) \sin^2 \delta_l.$$

With knowledge of the cesium van der Waals potential, it is possible to estimate the temperatures at which the $l = 2$ and $l = 4$ contributions to the scattering become important. From the van der Waals coefficients given in [47], the d-wave contribution should enter at approximately 150 $\mu$K, and the f-wave contribution near 1 mK. For a trap of 260 $\mu$K, the maximum resonant s-wave contribution is $\sigma_s = 8\pi/k^2 = 1.4 \times 10^{-12}$ cm$^2$. This is larger than our measured upper bound, and it lies well outside of our error bars. Thus it can be concluded that, up to temperatures of 260 $\mu$K, there is no resonant d-wave contribution, and the scattering is predominantly s-wave.

Finally, this value can be used to estimate the $T = 0$ value of the scattering length, although this estimate is entirely without experimental justification. Given that there is no appreciable d-wave contribution out to 260 $\mu$K, equation 6.2 can be solved for $a$, yielding $a \approx 33a_0$, where $a_0$ is the Bohr radius. This value lies outside of the range for $a$ quoted by [3]. Of course, this does not constitute a measurement of the scattering length, and an explicit temperature dependence of the cross section would have to be demonstrated before such a statement could be believed.

# Chapter 7 Evaporative Cooling - Theory

## 7.1 Introduction

Evaporative cooling is currently the most powerful method known for producing dense gases of ultracold atoms. The method consists of removing the hottest atoms from a gas and allowing collisions to establish equilibrium at a lower temperature. The atom removal is accomplished by the use of RF-induced spin flips at the outer edges of the trap. The method is extremely powerful, and it provides the only demonstrated means of attaining Bose-Einstein Condensation in systems of alkali atoms.

Since the original proposal by Hess [48], evaporative cooling has been successfully applied to cool traps of spin-polarized hydrogen [49], Rubidium [20], Sodium [19], and Lithium [26]. The major drawback of the method, though, is that a large portion of the trapped atoms must be lost during the evaporation process. For small initial atom numbers, this can be a severe hindrance to efficient detection of the cooled trap.

The alkalis mentioned above have been evaporatively cooled in states having a positive value of the scattering length. As discussed in the introduction to chapter 6, a positive scattering length means that the interactions between the ultracold atoms are inherently repulsive. This prevents further collapse of the atomic sample into a liquid or solid, and it ensures that the size of any condensate will be relatively large.

The $|4,4\rangle$ state of cesium, though, is predicted to have a large, negative scattering length [3]. It is presently a subject of heated debate as to exactly what a negative scattering length means for a Bose condensate. Several authors have predicted that negative scattering length systems have a limit to the number of atoms that their condensates can hold [63]. Stoof has predicted that negative scattering length systems could possibly undergo a collapse into a superfluid solid or liquid [64]. Whatever their ultimate fate, there is intense interest in evaporation dynamics of negative scattering length systems. This has been driving motivation behind our evaporative cooling work with cesium.

This chapter will be concerned with a description of the theory underlying evaporative cooling. At the end of the chapter, computer simulations will be presented that demonstrate the major trends predicted by the theory. In the next chapter, our experimental efforts in evaporative cooling of cesium will be presented.

## 7.2 Theory

The purpose of this section is to derive results necessary for a description of evaporative cooling. The methods presented here are based on the work of Walraven [50], his co-workers [51], and original work. The bulk of the credit, though, for formalizing the theory of evaporative cooling goes to Walraven's group. They have placed the theory on a firm theoretical foundation, removing most of the hand-waving and heuristics that previously characterized the subject. For convenience, most of the notation used here will be that found in their publications.

A theoretical description of evaporation is complicated by the fact that a gas undergoing evaporative cooling is not in a true state of equilibrium. The atoms are trapped in a potential well of finite depth, and a true thermal distribution of energies is therefore not possible. However, if the assumption is made that the well depth is much greater than the average energy of any single atom in the trap, then a quasi-thermal distribution is established, and thermodynamic methods can provide a meaningful description.

The work of this section rests on two main assumptions. First, the motion of the atoms in the trap is assumed to be ergodic [51], meaning that the phase space distribution of the atoms depends only on their energy, and not on the details of their orbital motion. Ergodicity is, in general, a valid assumption for magnetic traps. The non-ergodic mixing times that have been measured to date indicate that such mixing takes place only over long time scales, typically 30 seconds or greater [19]. The assumption of ergodicity enabled Luiten *et al.* to derive a critical result for the rate at which atoms are collisionally excited to energies exceeding the well depth [51].

Furthermore, the atoms are assumed to constitute a classical gas with energies distributed according to a truncated Boltzmann distribution. The truncation energy is equal to the well depth, which is made to continually decrease during the evaporation process. Luiten *et al.* [51] have shown, through direct numerical integration of the Boltzmann equation, that a truncated Boltzmann distribution provides an excellent approximation to the actual non-equilibrium distribution. The truncated Boltzmann form also lends itself quite naturally to calculation, enabling closed-form expressions to be obtained for most of the major results.

The general procedure in what follows will be to first find an analytic expression for the energy density of states for an Ioffe potential well. If the density of states is known, the partition function can be found; from the partition function, all thermodynamic results can be derived. The ultimate goal is an equation governing the evaporative cooling process, which is an equation relating the trap temperature to its energy and atom loss rates.

### 7.2.1 Density of States

If $\varepsilon$ denotes the energy of an atom trapped in the potential $U(\mathbf{r})$, then the number of states $\rho(\varepsilon)$ available to the atom at this energy is, by definition,

$$\rho(\varepsilon) = h^{-3} \int d^3r d^3p \, \delta\left(p^2/2m + U(\mathbf{r}) - \varepsilon\right),$$

since Planck's constant $h$ is the volume of the fundamental unit cell in phase space [52]. By use of a well-known property of the delta function [53]

$$\delta\left(f(x)\right) = \sum_{i=1}^{N} \frac{\delta(x - x_i)}{|f'(x_i)|},$$

where the $x_i$ are the roots of the function $f(x)$, the integral can be transformed into a form more useful for calculations:

$$\rho(\varepsilon) = \frac{2\pi(2m)^{\frac{3}{2}}}{h^3} \int_{U(\mathbf{r})\leq\varepsilon} d^3r \, \sqrt{\varepsilon - U(\mathbf{r})}.$$

For a gas of atoms in a magnetic trap, the potential $U(\mathbf{r})$ can be found from knowledge of the magnetic field $B(\mathbf{r})$. From equation 2.3, the field magnitude in cylindrical coordinates can be written as:

$$B(\rho, \phi, z) = \sqrt{\alpha^2\rho^2 + (B_0 + \beta z^2)^2}.$$

where it is assumed that $\alpha^2 \gg \beta B_0$, as is typically the case for evaporative cooling. The magnetic potential energy in such a field is $U(\mathbf{r}) = -\mu \cdot B(\mathbf{r}) = \mu B(\rho, \phi, z)$ for weak-field seeking atoms. Here, $\mu = \mu_F g_F m_F$, so that

$$U(\mathbf{r}) = \sqrt{\tilde{\alpha}^2\rho^2 + (U_0 + \tilde{\beta} z^2)^2} - U_0,$$

where $\tilde{\alpha} = \mu\alpha$, $\tilde{\beta} = \mu\beta$,and a constant offset has been added, for convenience, to make $U(0) = 0$. Substituting this form for the potential into the expression for the density of states yields:

$$\rho(\varepsilon) = \frac{2\pi(2m)^{\frac{3}{2}}}{h^3} \int_{U(\mathbf{r})\leq\varepsilon} d^3r \sqrt{\varepsilon + U_0 - \sqrt{\tilde{\alpha}^2\rho^2 + (U_0 + \tilde{\beta} z^2)^2}}.$$

This integral, though difficult, can be performed analytically [51], resulting in a compact expression for $\rho(\varepsilon)$:

$$\rho(\varepsilon) = A\left(\varepsilon^3 + 2U_0\varepsilon^2\right), \tag{7.1}$$

where $A = (2m\pi^2)^{\frac{3}{2}}/(h^3 2\alpha^2\beta^{1/2})$.

### 7.2.2 Phase Space Distribution

As is well-known from classical statistical mechanics, an ideal gas in equilibrium in the potential $U(\mathbf{r})$ has a Boltzmann phase space distribution [54]

$$f(\mathbf{r}, \mathbf{p}) = n_0\Lambda^3 e^{-(U(\mathbf{r})+p^2/2m)/k_B T}.$$

The quantity $n_0$ is the central density of the gas ($n(\mathbf{r} = \mathbf{0})$), and $\Lambda$ is the thermal

DeBroglie wavelength

$$\Lambda = \frac{h}{\sqrt{2\pi m k_B T}}.$$

As discussed above, an appropriate phase space distribution for a gas undergoing evaporative cooling is a truncated Boltzmann, with the truncation energy $\varepsilon_t$ equal to the well depth $\eta k_B T$:

$$f(\mathbf{r}, \mathbf{p}) = n_0 \Lambda^3 e^{-(U(\mathbf{r})+p^2/2m)/k_B T} \Theta\left(\varepsilon_t - U(\mathbf{r}) - p^2/2m\right).$$

The variable $\eta$ is known as the "truncation parameter"; it plays a prominent role in the evaporation process. The phase space distribution may also be written in terms of the total energy $\varepsilon$ as follows:

$$f(\varepsilon) = n_0 \Lambda^3 e^{-\varepsilon/k_B T} \Theta\left(\varepsilon_t - \varepsilon\right). \tag{7.2}$$

The $\Theta$ function is the Heaviside Step Function $\Theta(x)$, which is equal to 1 for $x \geq 0$ and 0 everywhere else.

Truncation changes the normalization of the phase space distribution. The quantity $\Lambda$ is still equal to the thermal DeBroglie wavelength, and the quantity $n_0$ is still a density, but $n_0$ is no longer equal to the actual central density $n(\mathbf{r} = \mathbf{0})$. To find an actual expression for $n_0$ in the truncated case, the most efficient method is to compute the density directly. With the phase space distribution known, the real space density can be computed by integrating over the momenta:

$$n(\mathbf{r}) = h^{-3} \int d^3p\, f(\mathbf{r}, \mathbf{p}) = n_0 \Lambda^3 e^{-U(\mathbf{r})/k_B T} \int d^3p\, e^{-p^2/2mk_B T} \Theta\left(\varepsilon_t - U(\mathbf{r}) - p^2/2m\right).$$

The integrand can be transformed into an incomplete gamma function, resulting in:

$$n(\mathbf{r}) = n_0 e^{-U(\mathbf{r})/k_B T} \Gamma\left(\frac{3}{2}, \frac{\varepsilon_t - U(\mathbf{r})}{k_B T}\right). \tag{7.3}$$

The incomplete gamma function is defined as:

$$\Gamma(x,\eta) = \frac{1}{\Gamma(x)}\int_0^{\eta} dt\, t^{x-1}e^{-t}. \tag{7.4}$$

From equation 7.3 for the density $n(\mathbf{r})$, the relationship between the central density $n(\mathbf{r}=\mathbf{0})$ and the density parameter $n_0$ is seen to be:

$$n(\mathbf{r}=\mathbf{0}) = n_0\Gamma\left(\frac{3}{2},\frac{\varepsilon_t}{k_BT}\right).$$

Since the incomplete gamma function is bounded between 0 and 1, the central density will always be less than that given by the density parameter $n_0$. Only in the limit of infinite well depth does $n_0$ equal the central density. The quantities $n_0$ and $\Lambda$, though, are still meaningful for expressing the normalization constant for the truncated distribution, since their product remains an accurate measure of the peak phase space density. The regime of quantum degeneracy (approximately one atom per cubic DeBroglie wavelength) is reached when $n_0\Lambda^3 \approx 1$.

### 7.2.3 Partition Function

With the distribution function known, the partition function can be calculated from the relation [52]:

$$Z = \int_0^{\varepsilon_t} d\varepsilon\, \rho(\varepsilon)e^{-\varepsilon/k_BT}. \tag{7.5}$$

Substituting equation 7.1 for the density of states into equation 7.5, a closed-form expression for the partition function results:

$$Z = Z_0\left[\Gamma(4,\eta) + \frac{2}{3}\frac{U_0}{k_BT}\Gamma(3,\eta)\right].$$

Here the parameter $Z_0 = 6A(k_BT)^4$, which is the partition function for an infinitely deep trap having $U_0 = 0$.

With this expression for the partition function, all thermodynamic properties of the gas can be computed. Before proceeding with this calculation, though, it is helpful to introduce an additional quantity that will aid in the interpretation of future results. Since the total number of atoms in the trap can be expressed as

$$N = \int d\varepsilon \, \rho(\varepsilon) f(\varepsilon),$$

we see that, after substituting equation 7.2 for the phase space density, a relation between the atom number and the partition function arises:

$$N = \int d\varepsilon \, \rho(\varepsilon) n_0 \Lambda^3 e^{-\varepsilon/k_B T} \Theta(\varepsilon_t - \varepsilon) = n_0 \Lambda^3 \int_0^{\varepsilon_t} d\varepsilon \, \rho(\varepsilon) e^{-\varepsilon/k_B T} = n_0 \Lambda^3 Z.$$

Defining a "reference volume" $V_e = N/n_0$ [50], this relation becomes

$$V_e = \Lambda^3 Z.$$

The reference volume $V_e$ is essentially the volume of the evaporating gas in the finite-depth potential well. In the limit of an infinitely deep potential, the reference volume approaches the true thermodynamic volume $V = N/n(0)$. Since $n_0 < n(0)$, the reference volume is smaller than the thermodynamic volume, as it should be.

### 7.2.4 Internal Energy

The total internal energy of the gas can be computed directly from the density of states

$$E = \int d\varepsilon \, \varepsilon \rho(\varepsilon) f(\varepsilon),$$

or from a derivative of the partition function [Goodstein]

$$E = N k_B T^2 \frac{1}{Z} \frac{\partial Z}{\partial T}. \tag{7.6}$$

The latter expression turns out to be the most useful. To compute the derivative of $Z$, it is necessary to first find the derivative of the incomplete gamma function. A useful technique for differentiating integrals is Leibnitz's Rule: for a function $\phi(\alpha)$

defined as an integral

$$\phi(\alpha) = \int_{u_1(\alpha)}^{u_2(\alpha)} f(x,\alpha)\,dx,$$

the derivative can be computed by the following formula:

$$\frac{\partial\phi}{\partial\alpha} = \int_{u_1(\alpha)}^{u_2(\alpha)} \frac{\partial f}{\partial\alpha}(x,\alpha)\,dx + \frac{\partial u_2}{\partial\alpha} f(u_2,\alpha) - \frac{\partial u_1}{\partial\alpha} f(u_1,\alpha).$$

By applying this rule to the incomplete gamma function (equation 7.4), a useful relation can be derived:

$$\frac{\partial\Gamma(x,\eta)}{\partial\eta} = \frac{x}{\eta}\left[\Gamma(x,\eta) - \Gamma(x+1,\eta)\right] = \frac{e^{-\eta}\eta^{x-1}}{\Gamma(x)}.$$

With this relation, a tedious calculation yields the following expression for the internal energy of a gas trapped in an Ioffe potential well:

$$E = \frac{12\Gamma_5 + 6(U_0/k_BT)\Gamma_4}{3\Gamma_4 + 2(U_0/k_BT)\Gamma_3} Nk_BT. \tag{7.7}$$

Here, the symbol $\Gamma_k$ is an abbreviation for $\Gamma(k,\eta)$, with $\eta = \varepsilon_t/k_BT$ as discussed previously. Note that in the limit of an infinitely deep well, $\Gamma_k \rightarrow 1$. For typical evaporative cooling conditions ($B_0 \approx 2G$, $T < 1\mu K$), $k_BT \ll U_0$ and $E \rightarrow 3Nk_BT$, the appropriate result for a harmonic well.

The expression for the total energy can be cast into a more familiar form by using the reference volume $V_e$. Since $V_e = N/n_0 = \Lambda^3 Z$, the derivative of the partition function in equation 7.6 can be expressed in terms of a derivative of the reference volume. Expressing the energy in this form yields the following expression [50]:

$$E = \left(\frac{3}{2} + \gamma\right) Nk_BT,$$

where

$$\gamma = \left(\frac{\partial \ln V_e}{\partial \ln T}\right)_{\varepsilon_t}.$$

In this form the individual kinetic and potential energy contributions are apparent.

### 7.2.5 Heat Capacity

It is also necessary to know the heat capacity of the gas in order to accurately describe its behavior during evaporation. Before the heat capacity can be computed, though, the independent thermodynamic variables of the problem must first be identified. From equation 7.7 for the total energy, it is evident that there are three independent variables: $N$, $T$, and $\varepsilon_t$. In a typical evaporative cooling scenario, the truncation energy is ramped down gradually as the gas cools. A good approximation to the ramping methods that have been employed thus far is to assume that the truncation parameter $\eta$ is kept constant during the evaporation. This means that the depth of the potential well decreases in proportion to the falling temperature of the gas. With this assumption about $\eta$, the needed heat capacity is the heat capacity at constant $\eta$:

$$C_\eta = \left(\frac{\partial E}{\partial T}\right)_{\eta,N} .$$

By keeping $\eta$ constant in the expression for the total energy (equation 7.7), straightforward differentiation produces the following expression for the heat capacity at constant $\eta$:

$$C_\eta = 6Nk_B\left[\xi\frac{2\Gamma_3(2\Gamma_5+\xi\Gamma_4)-\Gamma_4(3\Gamma_4+2\xi\Gamma_3)}{(3\Gamma_4+2\xi\Gamma_3)^2}+\frac{2\Gamma_5+\xi\Gamma_4}{3\Gamma_4+2\xi\Gamma_3}\right],$$

where $\xi = U_0/k_BT$, and, as before, $\Gamma_k = \Gamma(k,\eta)$. As a check on this expression, in the limit of an infinitely deep well and with $k_BT \ll U_0$, the heat capacity $C_\eta \rightarrow 3Nk_B$, as expected.

### 7.2.6 Equation for Energy Loss

Knowledge of the heat capacity $C_\eta$ enables an analog of the first law of thermodynamics to be written for the evaporatively cooling gas. Given that the three independent variables are the temperature $T$, the number of atoms $N$, and the truncation parameter $\eta$, a change in any of these variables produces a change in the total energy equivalent to

$$dE = C_{\eta,N}\ dT + \mu_{\eta,T}\ dN + \left.\frac{\partial E}{\partial \eta}\right)_{T,N} d\eta.$$

For the type of evaporative cooling considered here, the truncation parameter $\eta$ remains constant, so the last term in this equation is zero. For the second term, it can be seen from equation 7.7 for the total energy that

$$\mu_{\eta,T} = \left.\frac{\partial E}{\partial N}\right)_{\eta,T} = \frac{E}{N}.$$

Hence the expression for the differential change in the total energy reduces to

$$dE = C_{\eta,N}\ dT + \frac{E}{N}\ dN,$$

or

$$\dot{E} = C_{\eta,N}\dot{T} + \frac{E}{N}\dot{N}. \tag{7.8}$$

The importance of this equation lies in the fact that it relates evaporation-induced changes in the internal energy and atom number directly to a temperature change of the gas. In what follows, rate equations for $N$ and $T$ will be derived. These equations, when combined with equation 7.8, will allow the total energy to be eliminated, leaving a set of coupled differential equations for $N$ and $T$.

### 7.2.7 Rate Equation for N

Several processes can cause atom loss during evaporation. In addition to the atoms lost by forcibly ramping down the depth of the potential well, there is also a "natural" evaporation rate caused by collisions occurring within the trap. Furthermore, residual background gas atoms in the trapping chamber can collide with atoms in the trap, causing additional atom loss. This loss is generally exponential with time. These three loss processes are independent of each other, allowing changes in the atom number to be expressed as:

$$\dot{N} = \dot{N}_{NE} + \dot{N}_{FE} + \dot{N}_B.$$

Each of these loss processes will be discussed in turn.

### Atom Loss Caused by Natural Evaporation

Atoms in the trap continually undergo collisions with each other, irrespective of the presence of any forced evaporation. These collisions tend to equilibrate the trap on timescales $\tau \approx (n\sigma v)^{-1}$. Equilibration leads to a repopulation of the high-energy tail of the Boltzmann distribution, and, to atoms eventually spilling over the top of the potential well. The rate at which atoms leave the trap due to this collisional equilibration is what is denoted by $\dot{N}_{NE}$.

An actual calculation of this loss rate requires an equation for the evolution of the distribution function $f(\varepsilon)$. Generally, such a task requires a solution of the Boltzmann equation. For a gas in the s-wave scattering regime, Luiten *et al.* [51] have solved the Boltzmann equation under not-too-restrictive assumptions. They assume only that the motion of the atoms in the trap is "sufficiently ergodic," so that the phase space distribution function is expressible in terms of the total energy, as in equation 7.2. They also assume that any atoms promoted via collisions to energies exceeding the well depth are removed from the trap before they collide with any other atoms. With these assumptions, their analysis produces the following result for the natural evaporation rate:

$$\dot{N}_{NE} = -n_0^2 \overline{v} \sigma e^{-\eta} V_{EV},$$

with $\overline{v} = (8k_BT/\pi m)^{1/2}$ the mean thermal speed of the atoms in the trap, and

$$V_{EV} = \frac{\Lambda^3}{k_BT} \int_0^{\varepsilon_t} d\varepsilon\, \rho(\varepsilon) \left[ (\varepsilon_t - \varepsilon - kT) e^{-\varepsilon/k_BT} + kTe^{-\varepsilon_t/k_BT} \right],$$

an "effective volume" for the evaporation. Note that the expression varies as the square of the density, as it should for a two-body process, and that the rate decreases exponentially with increasing well depth.

### Atom Loss Caused by Forced Evaporation

A forced downward ramp of the potential well causes the atoms at the truncation energy $\varepsilon_t$ to be lost from the trap. At any given trap energy $\varepsilon$, there are

$$dN = f(\varepsilon)\rho(\varepsilon)d\varepsilon$$

atoms on a constant energy contour in the trap. At the truncation energy $\varepsilon_t$, this implies a forced evaporative loss rate of

$$\dot{N}_{FE} = -f(\varepsilon_t)\rho(\varepsilon_t)\dot{\varepsilon}_t.$$

### Atom Loss Caused by Background Collisions

Residual background atoms in the trapping chamber can cause trap loss through collisions. The background gas atoms are generally at room temperature (in our system, they are at 4 K). These atoms are orders of magnitude hotter than the sub-millikelvin atoms in the trap; hence any collisions between the two can be disastrous for the trapped atoms. Regardless of the vacuum quality, background collisions cause the atom number to decay exponentially in time, with a time constant $\tau_B$. Thus, one can write:

$$\dot{N}_B = -\frac{N}{\tau_B}.$$

The time constant is sensitive to the background gas pressure, as was first shown by Bjorkholm [55]. A trap with a typical background pressure in the low $10^{-11}$ torr range would have a time constant of one or two minutes. Our cryogenic system has demonstrated time constants of 4000 seconds.

### 7.2.8 Rate Equation for E

The total energy of the evaporating gas is affected by the same processes that cause atom loss from the trap. In addition to the energy loss due to forced evaporation, there is energy loss due to natural evaporation and energy loss due to residual background collisions. These allow a rate equation for $E$ to be written as:

$$\dot{E} = \dot{E}_{NE} + \dot{E}_{FE} + \dot{E}_{B}.$$

#### Energy Loss Caused by Natural Evaporation

Collision-induced evaporation causes the internal energy of the trap to decrease along with the atom number. With the Boltzmann equation formalism of Luiten *et al.*, this energy loss rate can be computed to be

$$\dot{E}_{NE} = \dot{N}_{NE}\left[\varepsilon_t + \left(1 - \frac{X_{EV}}{V_{EV}}\right) k_B T\right].$$

The quantity $X_{EV}$, as with $V_{EV}$ above, has the dimension of a volume and is equal to

$$X_{EV} = \frac{\Lambda^3}{k_B T}\int_0^{\varepsilon_t} d\varepsilon\, \rho(\varepsilon)\left[k_B T e^{-\varepsilon/k_B T} - (\varepsilon_t - \varepsilon + k_B T)e^{-\eta}\right].$$

The quantity $\left(1 - \frac{X_{EV}}{V_{EV}}\right)$ can be shown to be bounded between 0 and 1 [51]; hence this equation says that natural evaporation causes atoms to carry away an average energy between $\varepsilon_t$ and $\varepsilon_t + k_B T$.

#### Energy Loss Caused by Forced Evaporation

Forced evaporation removes atoms at the truncation energy $\varepsilon_t$, so the energy carried away by these atoms must be $\varepsilon_t$ times the rate at which this loss occurs, or

$$\dot{E}_{FE} = -\varepsilon_t \dot{N}_{FE} = -\eta k_B T \dot{N}_{FE}.$$

**Energy Loss Caused by Background Collisions**

As with the previous section, this energy loss rate must be the average energy per atom times the loss rate for this process, or

$$\dot{E}_B = -\frac{E}{N}\dot{N}_B = -\frac{E}{\tau_B}.$$

## 7.3 Simulations

Using the expressions derived above for the various energy loss and atom loss mechanisms, the equations governing evaporative cooling can be reduced to the following set:

$$\begin{aligned}
\dot{N} &= -n_0^2\overline{v}\sigma e^{-\eta}V_{EV} - f(\varepsilon_t)\rho(\varepsilon_t)\dot{\varepsilon}_t - \frac{N}{\tau_B} && (7.9)\\
\dot{E} &= -\left[\varepsilon_t + \left(1 - \frac{X_{EV}}{V_{EV}}\right)k_BT\right] n_0^2\overline{v}\sigma e^{-\eta}V_{EV} - \eta k_BTf(\varepsilon_t)\rho(\varepsilon_t)\dot{\varepsilon}_t - \frac{E}{\tau_B} && (7.10)\\
\dot{E} &= C_{\eta,N}\dot{T} + \frac{E}{N}\dot{N}. && (7.11)
\end{aligned}$$

The last two equations can be used to eliminate $\dot{E}$, and equation 7.7 can be substituted for $E$, leaving a set of two coupled, first-order differential equations for $N$ and $T$. All other terms in the equations can be expressed in terms of $N$, $T$, and the physical constants $\eta$ (truncation parameter), $\tau_B$ (background loss time constant), $a$ (scattering length), $B_0$ (bias field at trap center), $\alpha$ (radial field gradient), and $\beta$ (axial field curvature). Given a set of values for these constants and initial values for $N$ and $T$, the equations can be stepped forward in time to reveal the dynamics of the evaporation process.

**Variation with $\eta$**

It is interesting to study the dynamics of evaporative cooling as a function of the truncation parameter $\eta$. Intuitively one expects that, for very high values of $\eta$, evaporation would proceed slowly, if at all. A high value of $\eta$ means that very few of the

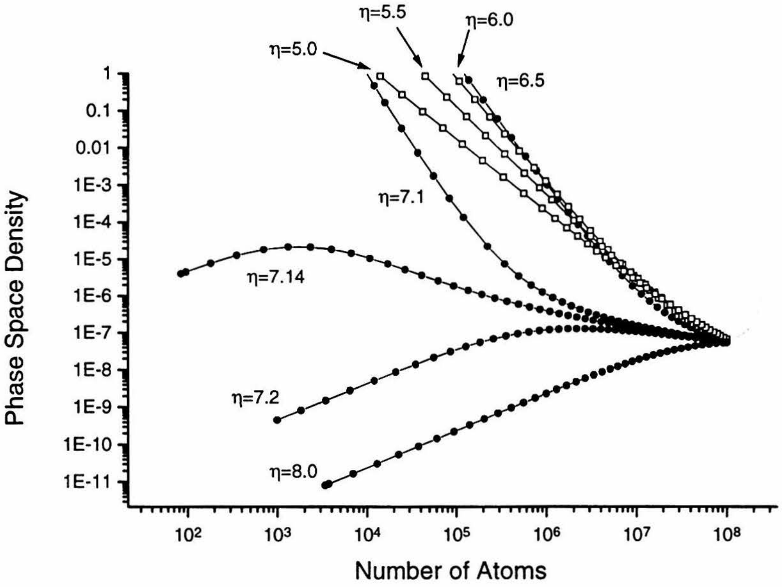

Figure 7.1: Behavior of phase space density for various values of the truncation parameter.

atoms are forcibly removed due to evaporation, and that background gas collisions dominate the trap loss process. This is an undesirable situation, since background collisions remove both hot and cold atoms, whereas forced evaporation removes only the hottest ones.

As the value of $\eta$ is lowered, the efficiency of the evaporation increases, since a greater number of the hottest atoms are being forced from the trap. Here "efficiency" means the greatest gain in phase space density per atom lost. Eventually a critical value of $\eta$ is reached at which the evaporation is able to continue all the way to BEC. Further lowering $\eta$ eventually results in a decrease of the cooling efficiency, since too many of the colder atoms are lost due to truncation.

These conclusions are confirmed by the simulations. Figure 7.1 is a plot of the phase space density versus atom number for various values of the truncation parameter $\eta$. The following values, typical for our trap, have been chosen for the physical parameters: $\tau_B = 60$ s, $a = 200a_0$, $B_0 = 1.8$ G, $\alpha = 270$ G cm$^{-1}$, and $\beta = 300$ G

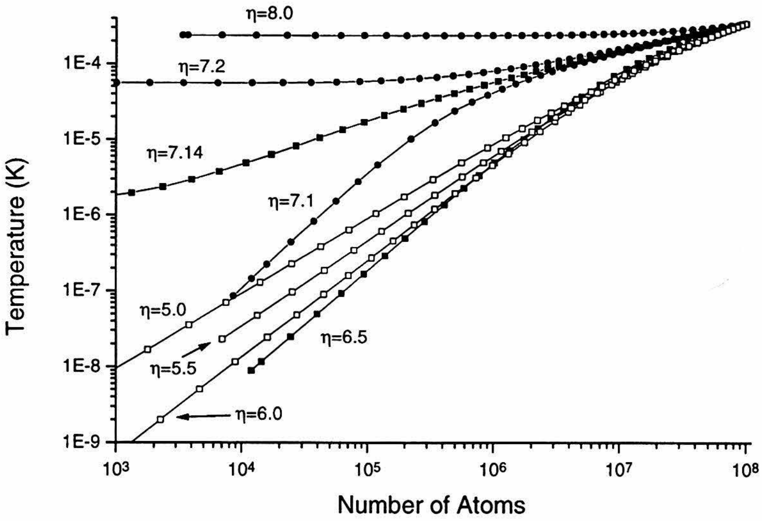

Figure 7.2: Behavior of trap temperature for various values of the truncation parameter.

$\text{cm}^{-1}$.

In the plot, the initial condition is at the lower right portion of the graph, and the cooling proceeds to the left along the curves. From the figure it can be seen that, for $\eta \leq 7.14$, the forced evaporation is not sufficient to carry the system to BEC. The trap temperature decreases somewhat, as the next figure shows, but the temperature loss is not sufficient to increase the phase space density or to drive up the equilibration rate.

Somewhere between $\eta = 7.14$ and $\eta = 7.10$ a critical value of the truncation parameter is reached that allows the system to enter a stage of runaway evaporative cooling. Runaway evaporation is a state marked by a continually increasing phase space density, real space density, and collision rate. As the figures clearly show, an $\eta$ of 7.1 satisfies this condition. Note that it is possible to reach runaway evaporation with an initially *decreasing* collision rate. The curve in figure 7.3 for $\eta = 7.1$ shows that the collision rate decreases initially, turns around near $10^6$ atoms, then accelerates until quantum degeneracy is reached.

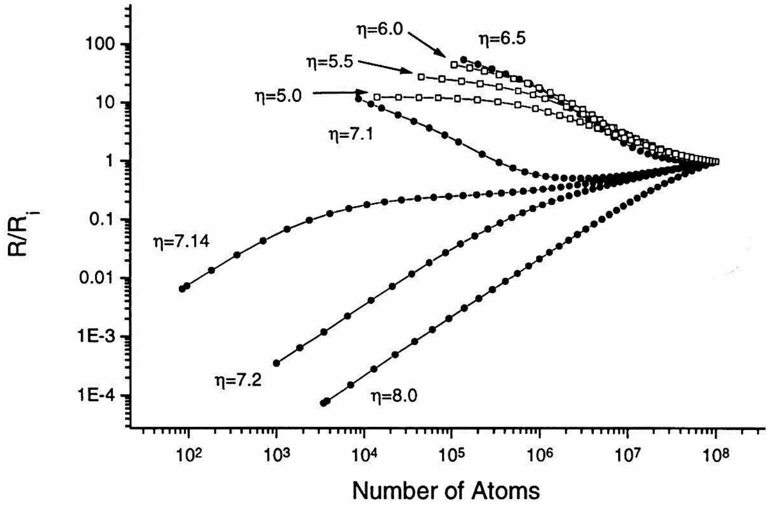

Figure 7.3: Behavior of the collision rate for various values of the truncation parameter.

For values of $\eta$ smaller than that required for the onset of runaway, there is an extremal value that produces the most efficient cooling, or the greatest phase space gain for total number of atoms lost. In these simulations, the extremal value is $\eta = 6.5$. This value of $\eta$ is obviously the one to choose experimentally, since it leaves the system with the greatest number of atoms at the end of the evaporation process.

As $\eta$ is decreased below the extremal value, the efficiency of the cooling begins to fall. For values of $\eta$ between 5 and 6, the system still reaches BEC, but it does so with fewer atoms and with less phase space gain per atom lost. The reason for this behavior is that for these low values of $\eta$, the truncation "knife" removes not only the hottest atoms (as it should), but too many of the colder ones as well. Further decreases in $\eta$ should result in a system with very few atoms unable to attain BEC. Unfortunately, the equations become very unstable at low $\eta$, and numerical difficulties prevented further investigation of this regime.

# Chapter 8 Evaporative Cooling - Experimental

## 8.1 Introduction

The purpose of this section is to provide a detailed description of the procedure followed in our attempts to achieve runaway evaporative cooling. A successful evaporative cooling run requires a complicated, multi-step procedure. Each step needs to be fully optimized if the cooling scheme is to be successful. We were unable to achieve runaway cooling for a variety of reasons; these reasons and our cooling procedure will be discussed in this chapter.

A typical evaporative cooling run can be broken down into these individual steps:

- MOT Loading
- PG Cooling
- Optical Pumping
- Mode-Matching
- Compression
- Evaporation and Imaging
- Coil Defluxing and System Reset

In what follows, each individual process will be discussed in detail.

### 8.1.1 MOT Loading

The purpose of the loading phase is the accumulation of large numbers of atoms in the trap. Since evaporation is inherently a lossy process (decreases of four or five orders of magnitude in the atom number are not uncommon), it is desirable to begin the process with as many atoms as possible. Our system loads from an atomic beam directed at the center of our MOT. Direct capture from the atomic beam, though, is not very efficient, since this method only captures the low-velocity tail of the beam. A typical capture speed for a MOT might be 20 cm $s^{-1}$; when loaded from a thermal beam with a mean temperature of 500 K, the percentage of the total number of atoms captured is very small indeed.

A dramatic improvement in the number of atoms loaded can be obtained with a slowed atomic beam. Slowed beams produce large numbers of atoms with speeds small enough to be captured by the MOT. One powerful method for producing a slowed beam is that of Zeeman Tuned Slowing [56]. With this method the beam moves along the axis of a solenoid tapered so as to keep an opposing, fixed-frequency laser beam in resonance with the atoms in the beam. This method is capable of producing an intense flux of slow atoms (trap loading rates of $\approx 10^{10}$ atoms $s^{-1}$ [65]).

Because of technical difficulties with our cryogenic system, and also because of physical space limitations, we are not presently able to use a Zeeman-tuned slower. Instead, we use a comparable alternative to Zeeman slowing called chirped-laser slowing [57]. In this method we oppose our atomic beam with a laser beam tuned slightly to the red of the 4-5 transition. The oncoming atoms in the beam see the laser photons doppler-shifted up into resonance, enabling them to absorb the photons from the beam. When a photon gets absorbed, the absorbing atom loses forward momentum in an amount equal to that of the incoming photon. At some later time, the atom spontaneously re-emits the photon in a random direction. Even though the spontaneous emission is in a random direction, the atoms in the beam continually absorb photons from a *single* direction. The net result is a dramatic reduction in the forward velocity of the atoms, with a small amount of transverse heating.

As the atoms slow down, the doppler shift of the laser beam decreases. If the doppler shift is not maximally on resonance with the atoms, the cooling efficiency is reduced, and the number of atoms loaded into the trap goes down as well. To compensate for the changing doppler shift, the laser beam is *chirped,* or scanned in frequency so as to keep the atomic beam maximally on resonance. We typically chirp the beam from –200 MHz to $-5$ MHz or so in 4.3 ms, these parameters being determined by trial and error optimization. On our best slowing days, we can increase the number of atoms loaded into our trap over the non-slowed case by a factor of 50, and load $\approx 10^8$ atoms into the MOT.

### 8.1.2 Polarization-Gradient Cooling

It is advantageous to begin evaporative cooling with as high an initial density as possible. The collision rate is proportional to $n_0 \sigma v$, so, if the initial density could be increased, the thermalization rate would increase as well. The density of the PG cooled trap can be increased by ramping up the coil currents and compressing the trap. Unfortunately, a compression of the trap causes the trap to heat. This heating can be minimized by beginning the compression with as cold a trap as possible, i.e., with a PG cooled trap.

To put this in more quantitative terms, consider an efficient form of compression, an *adiabatic* compression. An adiabatic compression conserves phase-space density, which means that the product $n_0 \Lambda^3$ remains constant during the compression. Since $\Lambda$ has a $T^{-1/2}$ dependence, an adiabatic compression conserves the product $n_0/T^{3/2}$, so that the final temperature is related to the initial temperature as follows:

$$T_f = T_0 \left( \frac{n_f}{n_0} \right)^{2/3} .$$

It is common for the compression stage to increase the density by at least an order of magnitude, meaning that the final temperature will be approximately five times the initial temperature. In practice, a true adiabatic compression is difficult to achieve, so the final temperature is usually even higher than this.

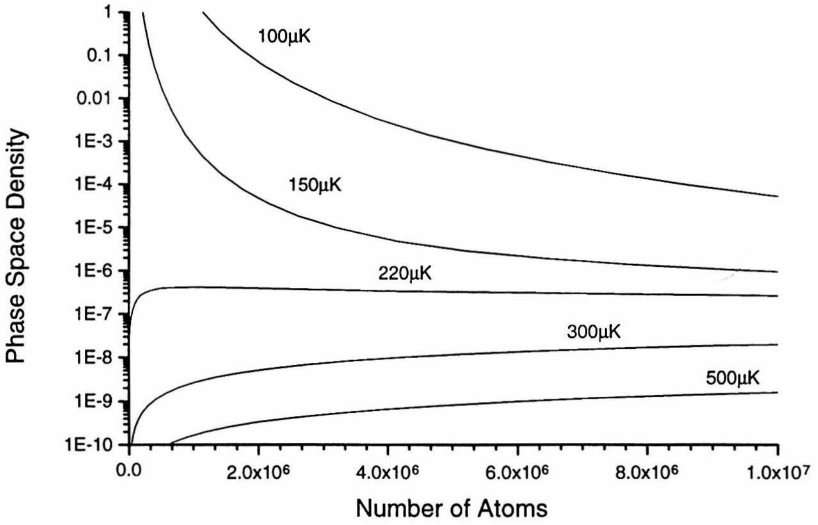

Figure 8.1: Evaporation with various initial temperatures.

To investigate the effect of the initial temperature on the evaporation process, refer to figure 7.1. The initial conditions in this plot are $\eta = 8.0$, $N_0 = 5 \times 10^7$ atoms, and other parameters as in the previous simulations. Here the effects of the initial temperature are clearly apparent. If the temperature is too high, evaporation simply cannot continue into the regime of quantum degeneracy. The reason for this is straightforward: if the temperature is too high, too many atoms must be lost initially to carry away the excess heat.

The theory of PG cooling [15] predicts that the final temperature of a PG-cooled trap is proportional to the light-shift parameter:

$$T \sim l = \frac{\Omega^2}{|\delta|\,\Gamma},$$

where, as before, $\Omega$ is the Rabi frequency, $\delta$ is the laser detuning from resonance, and $\Gamma$ is the linewidth of the transition. This expression has been found to be valid for values of $l$ down to approximately. 0.1 [58]. Below this value, Townsend *et al.* have found that the confinement of the MOT starts to degrade, causing trap densities to decrease [12]. These authors speculate that the degradation is caused by a reduction of the spring constant, but they have no explanation of the mechanism. For our system, we have not found the degradation to be as severe. In fact, our measured temperatures are lower the greater the detuning from resonance, so we typically keep $l \approx 0.1$.

We perform our PG cooling stage in the following manner. After MOT loading, the laser detuning is jumped to the red of the $F = 4$ to $F' = 5$ resonance to a variable value; typically, we detune to 60 MHz. After a delay of 2 ms (for trap oscillations to die out), the field gradient is reduced from its 10 G value at loading to approx. 1.7 G. The power in the trapping laser is reduced by a factor of 20, giving a light-shift parameter of roughly 0.2. The reduction in the trapping laser power is accomplished by the use of a DisplayTech light valve. The light valve is essentially a voltage-controlled $\lambda/2$ waveplate; when used with a polarizer, it provides a quick ($\approx$ 30 $\mu$s) and precise means for laser beam attenuation.

When the light valve reaches its maximum attenuation the trap is PG cooled for up to 3 ms. The 3 ms value is a trade-off between timing constraints (imposed by laser shutters) and density loss (caused by too long a PG cooling time). We find that PG cooling for longer than 5 ms causes excessive trap loss. With a successful PG cooling stage, we can typically reduce the temperature of our trap by a factor of 2 or 3, to somewhere between 60 $\mu$K and 80 $\mu$K.

### 8.1.3 Optical Pumping

After the MOT has been PG cooled, the atoms are optically pumped into the $|4,4\rangle$ state to prepare for capture in the Yin-Yang trap. The optical pumping is necessary for two reasons. First, after the PG cooling phase, the atoms in the MOT are distributed amongst all of the trappable m-states, i.e. m=4,3,2,1. The states with lower m-values are more weakly bound, and atoms in these states tend to get ejected from the trap in the transfer process from MOT to MST. Furthermore, the presence of multiple m-states in the MST complicates the interpretation of images, and it affects the trap dynamics and collisional processes. Thus, to have clean images and to capture the greatest number of atoms, an optical pumping stage is included.

At the end of the PG cooling stage, the MOT fields are turned off and a uniform bias field from the outer bias coils is applied to the trap. Circularly polarized $\sigma^+$ light tuned slightly to the red of the $F = 4$ to $F' = 4$ transition is applied to the atoms for two milliseconds. The $F = 3$ to $F' = 4$ repumper is on for this time as well. The two millisecond time is a compromise between heating caused by optical pumping and the number of atoms pumped. The longer the optical pumping beam is left on, the hotter the atoms get, but more atoms get optically pumped. The two millisecond time limit enables us to capture approx. 50%-60% of the atoms in the Yin-Yang trap with minimal heating. The 50%-60% figure is characteristic of atom trapping experiments today [59]. Presumably, most of the atoms captured are in the $|4, 4\rangle$ state, but we have no direct way of measuring the actual populations in the different m-states. If there were a significant population in the lower m-states, the trap images would show a pronounced halo since the lower m-states are more weakly bound. We observe no such halo in our trap images.

### 8.1.4 Mode Matching

After the optical pumping stage, the atoms must be loaded into the spin-polarized magnetostatic trap. The best method for capturing the atoms is to offer them a magnetic potential well with the same curvatures as the well of the PG cooled MOT. This minimizes the heating caused by the transfer process. Unfortunately, with an imperfect PG cooling stage, the mode-matching must be done at higher than ideal currents in order to capture the hottest atoms. In our experiments, we found that calculations of the trap frequencies proved to be relatively useless for determining optimal mode-matching. By trial and error, we found a mode-matched trap that allowed us to capture most of the atoms after optical pumping, but it left the trap with a higher than desirable temperature. Unfortunately, we were unable to reduce the temperature of the trap without losing a significant fraction of the atoms.

### 8.1.5 Compression

The compression stage is used to drive up the collision rate by increasing the trap density, and, to some extent, the trap temperature. Ideally one desires an adiabatic compression, since this type of compression conserves phase space density and produces minimal heating. In practice, though, the achievable compressions are somewhat less than adiabatic.

Our traps are compressed by incrementally ramping up the currents in the various coils of the Yin-Yang trap. We typically ramp up the currents in the inner mot coils and the U-coils in 500 steps, taking 1 ms per step. The current in each coil is incremented in turn in a round-robin fashion (our GPIB controller does not allow simultaneous ramping). After these coils achieve their full current, we adjust the current in the outer bias coil slowly, typically taking 1000 steps of 1 ms each. The bias coil current is chosen to give a small residual bias at the trap center (approx. 2 G), and it is adjusted slowly to squeeze the trap without production of excess heat. Various ramping methods were tried, both fast and slow; this method produced the best results.

### 8.1.6 Evaporation

After the compression step, the trap is given 1 ms to equilibrate before evaporation begins. The evaporation is performed by introducing an RF field into the trapping chamber. There is a small RF coil mounted inside the cryosphere that has a direct line of sight to the trap center. The leads from this coil are attached to an SMA feedthrough mounted in one of the unused window ports on the cryosphere. The feedthrough is connected to a piece of flexible, stainless steel, cryogenic transmission line, anchored to the radiation shield at the other end. The waveguide is attached to a two-wire transmission line connecting the radiation shield to a port on the outer vacuum chamber. This port contains an SMA feedthrough, which is connected to a

GPIB-enabled, HP RF generator via a piece of BNC cable.

The evaporation is accomplished by having the RF field induce transitions amongst the m-levels of the $F = 4$ manifold [60]. This is essentially a magnetic resonance problem - once the atoms make transitions to states having $m$ negative or 0, they are ejected from the trap. To estimate the RF frequency needed for evaporation, consider an atom moving in the Yin-Yang harmonic potential well. If the truncation parameter is $\eta$, the maximum field experienced by an atom in this well is

$$B_{\max} = B_0 + \frac{\eta k_B T}{g_F \mu_B}.$$

This corresponds to an RF frequency of

$$v_{RF} = \frac{g_F \mu_B}{\hbar} \left[ B_0 + \frac{\eta k_B T}{g_F \mu_B} \right],$$

or

$$v_{RF} = \frac{1}{\hbar} \left[ g_F \mu_F B_0 + \eta k_B T \right].$$

This expression is the relationship between the trap temperature and the RF frequency for a given truncation parameter.

The evaporation was performed by ramping down the RF frequency. The HP generator can change its frequency every 125 $\mu$s, so the ramps were piecewise continuous. Both linear and exponential ramps were tried; linear and exponential ramps with multiple segments of different time constants were tried as well. No matter how the ramps were performed, no increase in the phase space density exceeding one order of magnitude was ever observed.

At the end of the ramping period, the RF was turned off and the trap was given a period of time to equilibrate. Then the repumper shutter was opened, illuminating the trap with $F = 3 \rightarrow F^{'} = 4$ light. Approximately 4 ms later, the trapping laser shutter was opened. The 4 ms delay is necessary because of uncertainties in the opening times of the mechanical shutters. The trapping laser light triggered a TTL photodiode, sending a gate signal to the Xybion CCD camera. On receipt of the gate signal, the camera snapped a 100 $\mu s$ exposure. The image was captured by an Imaging Technologies frame grabber board and then colorized, filtered, and fit to a 2-D gaussian profile.

### 8.1.7 Coil Defluxing

After acquiring the image and fitting it, the system was reset for another run. The coils, though, were not able to make further traps because of flux trapping within the superconducting wire. Our coils are wound with multifilamentary NbTi wire. This is a type-II superconducting material, and it suffers from the usual flux penetration problem above the lower critical current. The lower critical current is proprietary to the wire's manufacturer, Supercon, and is not known. For our coils, though, we see evidence of flux trapping with approx. 200 mA of current in the coils.

The flux trapping problem for a given wire composition cannot be overcome - only its effects can be minimized. The multifilamentary wire helps in this regard by minimizing the volume of superconducting material. To expel the trapped flux the coils were driven normal by sending current through small resistive heaters mounted on the U-coils and on the bias coil. The U-coils go normal within 5 seconds of being heated; the bias coil follows suit after about 15 seconds. With the U-coils and the bias coil normal, the heating process is continued until conduction drives the inner MOT coils normal after about 30-45 seconds. After all coils go normal, the heat is turned off and the coils are allowed to cool down and become superconducting again. The cooling process takes anywhere from two to three minutes, after which time the coils can be used for further trapping.

### 8.1.8 Discussion

A typical before, during, and after image of an evaporative cooling run is seen in the next figure 8.2. These images are not from the same trap, since our imaging procedure is destructive. However, the image shapes are characteristic of the various stages of the evaporation process. In all three images, the linear scales are identical, but the

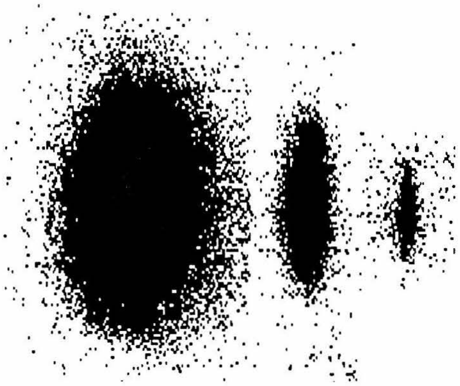

Figure 8.2: Images before, during, and after evaporation.

CCD camera gain increases dramatically from left to right.

In figure 8.2, the large blob on the left is the PG cooled trap immediately after mode-matching. The trap has a slight prolate shape, intermediate between that of the PG cooled quadrupole trap and the excessively prolate Yin-Yang trap. The middle image is the trap after compression and after some evaporation. The symmetrical cigar-shape is characteristic of the Yin-Yang field. The image on the right is the trap after enough evaporation to put it nearly at the limit of our detection capability. In this particular example, evaporation increased the phase space density by nearly one order of magnitude over its initial value.

As for our difficulties with achieving runaway, the main reason we failed is that our compressed magnetostatic traps are too hot. We have an unexplained source of heat in our traps that causes our compressed MSTs to be too hot for initial evaporation. This heat seems to arise after the PG cooling stage and during the mode-matching stage. Although we have not been able to identify the precise cause of this extra heat, some or all of the following alternatives are possible.

The first possibility seems to be that our PG cooling stage is not working well enough. Successful PG cooling requires good circular polarization of the laser beams. The polarization of our beams may be degraded to an unacceptable extent by cryogenic-induced stresses in the windows of our cryosphere. Stress-induced birefringence is a common problem in the cryogenic community [61]; one typically overcomes it by taking great pains to mount optical components in the most stress-free manner possible. Even though our windows are mounted with soft Indium seals, the cooldown to 4 K could easily subject them to stresses beyond our detection ability.

If the problem does indeed lie with the polarization, this could be a major impediment to the future development of cryotrapping. Needless to say, we have spent months trying to improve the quality of the PG cooling. Some modest improvements have been made, but no single reliable method that produces consistently cold traps has been found.

Another reason for the excess heat could lie in the manner in which the coils are mode-matched. It is not possible to simultaneously energize all coils in the Yin-Yang trap. Due to the nature of our power supplies, each coil must be separately energized in turn. After the optical pumping stage, the current in the lower MOT coil is jumped, then the upper MOT coil, the U-coils, and lastly the bias coil. There is a delay of 320 $\mu$s between each jump due to the GPIB protocol. It may be that the successive jumps of the coils shake the atoms excessively, driving up their temperature. We have tried different orders of coil ramping, but the final temperature is unchanged.

There is another problem with the mode matching. Since the PG cooling is not as effective as it could be, the trap must be mode matched at a higher current to capture the hotter atoms. If the PG cooled trap is mode-matched into a weaker trap, unacceptable atom loss occurs. Thus, to capture the desperately needed atoms in the MST, the trap must be mode-matched at too high a current. If the trap is mode-matched at a lower current, the atoms are cooler, but many of them are lost. This is indeed a serious problem, and it can only be overcome if the PG cooling can be improved.

Another reason for lack of success with evaporative cooling may lie with the cross section. The primary motivation for using the $|4,4\rangle$ state is its reportedly large s-wave cross section [3]. The $T = 0$ cross section has been measured to be at least one order of magnitude larger than that of any other alkali atom. Because of our difficulty with evaporative cooling, we were led to remeasure this cross section in the hopes that perhaps it is smaller than what it was claimed to be. Indeed, we find that, even when the $1/T$ dependence of the cross section is taken into account, we find an upper bound on the cross section to be a factor of two below the maximum resonant s-wave value.

### Suggestions for improvement

Obviously, the PG cooling capabilities of the cryotrap need to be improved. If cryogenic stress is indeed the reason for the excess heat, then it is possible, in principle, to correct any degree of elliptical polarization by the use of a Soleil-Babinet compensator. Perhaps each beam of the trap would require such a device. This option has not been available to us, though, because of the prohibitive expense of these compensators.

Another major improvement would be realized if the coil design and optical layout were redone to handle larger beams. The number of atoms a MOT can hold is in proportion to the cube of the beam diameter [62]; hence a large improvement could be realized if the beam diameter were doubled. Higher atom numbers seems to be the universal panacea in the BEC business; by loading an order of magnitude more atoms in to the MST, many of the picky details of the present experiment could be avoided.

# Appendix A Dewar Precooling, Fill, and Warmup

## A.1 Precooling Procedure

There **must** be a vacuum in the space surrounding the floating shield before evacuating the liquid helium reservoir. The LHe tank can only support a limited inward pressure. It may be helpful to refer to the drawing of the dewar, fig. 3.2, as these steps are followed.

1. Pump out the LHe tank and backfill with He gas. This step is necessary to remove any water in the LHe tank.

2. Pump on the central tube at the top of the dewar. Exercise the needle valve several times to make sure that the capillary tube is not clogged (listen to the pump). Keep pumping on the central tube for the remaining steps.

3. Start transferring LN2 to the LHe tank. Exercise the needle valve frequently during the transfer to make sure that it doesn't freeze during the rapid cooldown. It takes approximately 20 minutes to start accumulating LN2 on the bottom surface of the LHe reservoir. When the LN2 begins to accumulate, there will be a big pump response when the needle valve is exercised (since liquid is flowing through the capillary), and the exhaust will also be reduced somewhat. Put a hose on the dewar exhaust to keep out any water. Fill the LHe tank about 1/3 full with LN2. Fill the LN2 reservoir 1/2 full. Fill the blue dewar.

4. Open needle valve to fill 1K pot. Leave LN2 in both LHe and LN2 tanks overnight.

## A.2 Fill Procedure

1. Close the needle valve. Insert the threaded helium exhaust tube into the LHe fill port. Pressurize the LHe reservoir (4-5 psi) to blow any remaining LN2 out. Send the LN2 into the LN2 jacket.

2. Pressurize the 1K pot (4-5 psi) to force the LN2 out of it, back through the capillary, and into the LHe tank. Repeat step 5. After LN2 stops coming out of the exhaust tube, keep pressurizing for another 5-10 minutes.

3. Pump on the LHe reservoir about 10 minutes or so to get the last LN2 out. Make sure that a He gas backfill system has been setup before pumping. Open the needle valve while pumping on the central tube to fill the capillary with He gas. 1K pot should be above 77K.

4. Start transfer of LHe to the reservoir. Insert the transfer line slowly into the storage dewar and purge the transfer line of any air. Wait until very cold He gas comes out the other end, then insert into cryostat. Once in place, pressurize the storage dewar. A slow transfer gives more efficient cooling (until transfer line losses dominate). Exercise the needle valve during transfer (still pumping on central tube). After about 30 minutes, check the LHe level sensor for accumulation. He transfer rate should be slow enough so that no LHe accumulates for 30 min. When the LHe exhaust at the top of the dewar dies down, it is a likely sign that some accumulation has started. Turn up the pressure on the storage dewar to 4-5 psi. Try for a transfer rate of approx. 40 l/hr. Watch exhaust and level sensor to see when the storage dewar is empty.

5. After transfer, replace the LHe transfer line with the radiation baffle tube, and connect all three dewar exhausts to the exhaust network. If the central tube is not being pumped on, vent it through the exhaust network as well. Make sure the level sensor is **off** when not in use.

## A.3 Warmup Procedure

1. Let blue dewar empty itself out (takes about 40 hours if completely full). Blow the LN2 out if necessary.

2. Empty the LN2 jacket. Insert poly-flow tubing with cork into one exhaust port of the reservoir so that the tube touches the bottom. Cork another exhaust port, and pressurize through the third port to force the LN2 out.

3. Empty the LHe tank. Insert the threaded tube into the LHe fill port. Pressurize one of the other ports to force the LHe out.

4. With all cryogens removed, let the system sit until all parts are above 77K. Make sure the gate valve is closed; remove its power so that it stays closed. Turn off the interlock ion pump so that the rising pressure blast won't trip its protection mechanisms.

5. If the entire system needs to be warmed up, plug the right-angle valve into the wall socket so that it stays open. Turn off the main turbopump and let the outer chamber up to dry nitrogen gas (through the valve on the turbopump). Monitor the pressure with the thermocouple gauge - do not let the pressure get above 1 atmosphere! When the pressure is near 1 atm., open the extra valve on the outer endcap to act as a safety; put a paper towel in the hole to prevent pressure buildup from the volumes of cryopumped gas that will be released. The entire system will warm up via conduction through the nitrogen gas. Let the temperature of the inner chamber rise to above 273K.

6. Open system.

# Appendix B Vacuum Cleaning Procedures

This appendix provides an overview of the procedures used for cleaning the components in our vacuum system. The procedures are adapted from those used at the Stanford Linear Accelerator Center.

## B.1 Copper

### B.1.1 Degreasing

Mix a solution of Alconox alkali cleaner and water, reasonably concentrated so that lots of suds are generated. Scrub the parts vigorously with a tile cleaning brush until the grease deposits are off. Be sure to get the Alconox into all crevices and holes, no matter how tiny.

Tapped holes are a problem. To clean them, take a pipe cleaner and swab it around repeatedly in the tapped hole. Repeat the swabbing procedure until the pipe cleaner comes out with no grease on it. When the pipe cleaner comes out clean, take a Kim-Wipe and roll it into a point small enough to fit inside the tapped hole. Swab the Kim-Wipe around in the hole, then remove it. If the Kim-Wipe is clean, move on to the next hole. If not, repeat the pipe cleaner treatment. Rinse all parts in tap water thoroughly to get the greasy soap off.

Mix a new solution of concentrated Alconox and water. Immerse the parts in this solution, and ultrasonically clean for 10 minutes. Rinse thoroughly with tap water.

Soak the parts in Enbond Q527 alkali cleaner (product of Enthone, Inc., New Haven, CT) for 5 minutes at 180° F. Mix the Enbond in the ratio of 1/2 lb. per gallon of water. Heat the solution with an immersion heater resistant to alkali attack (such as one coated with Incoloy). A good choice for a heater is a 1000W Protherm, model OSI-U-110. Remove the parts with teflon-coated tongs. Rinse thoroughly for at least 2 minutes in tap water. Make sure all of the Enbond is off.

### B.1.2 Deoxidation

Immerse the parts in a straight solution of 50% *concentrated* hydrochloric acid (available from VWR) for 2 minutes. The oxide will instantly be removed once the parts become immersed in the acid. Rinse thoroughly for at least two minutes in running tap water. Store the deoxidized parts in water to prevent re-tarnishing.

### B.1.3 Surface Etch

Immerse the parts for 1-2 minutes in this solution:

1. 70% Phosphoric Acid, 75% concentration
2. 23% Nitric Acid
3. 6.5% Acetic Acid, Glacial
4. 0.5% Hydrochloric Acid, Analytical Grade

When the parts are immersed in this solution, millions of tiny bubbles form as the surface gets etched away. As the etching continues, the solution begins to turn green. For most of our cleaning, we obtained good results with a 1 minute dip. When the part is removed, it will be covered with a white bubbly film. Remove the film with a 2 minute tap water rinse. Make sure all of the acid solution is off. Note: after the rinse, the part will slowly begin to tarnish.

### B.1.4 Bright Dip

Immerse the parts for 5 seconds in this frightening mix, called *Chromerage:*

1. 33% Water

2. 0.5% Hydrochloric Acid, Analytical Grade
3. 43% Sulfuric Acid
4. 23% Nitric Acid, added *slowly*

This is a dangerous solution if mixed haphazardly, or too fast. The mixing of these acids produces a highly exothermic reaction, and it is possible for the solution to boil and fume for quite some time. We usually mix this stuff in a glass beaker sitting in a big Neoprene pan with lots of baking soda nearby. It is best to wait until the solution cools to room temperature before dipping parts in it.

When the parts are dipped in this solution, the surface begins to get eaten away, producing a bright shiny finish. When the parts are removed from the solution, the reaction continues and green smoke rises up from the parts! Remove the parts from the solution and place them immediately in a big tub of water, then rinse in tap water for 2 minutes. There is hardly any tarnishing during the rinse.

### B.1.5 Passivation

After the acid treatment, the surface consists of fresh copper that is highly susceptible to oxidation. To form a stable surface, the surface must be passivated. Mix a solution of 99 parts distilled water and 1 part Oxyban 60 (product of Thiokol/Dynachem Corp., Tustin, CA). Immerse the parts for 5 minutes, then rinse in tap water for 1 minute. The parts should be shiny and beautiful at this point.

### B.1.6 Final Rinsing

1. Rinse in cold deionized water for 1 minute (min. resistivity of 1 MΩ·cm).
2. Rinse in hot (90° C or greater) deionized water for 1 minute.
3. Immerse in analytical reagent grade isopropyl alcohol at 115° F for 30 seconds.
4. Blow parts dry with clean, dry nitrogen gas (40-50 psi is good).

5. Wrap in vacuum grade aluminum foil (from All Foils Co., Brooklyn Heights, OH).

## B.2 Stainless Steel (304 series)

### B.2.1 Degreasing

Follow the degreasing procedure for copper.

### B.2.2 Surface Etch

Immerse the parts in the following solution, at room temperature, until the parts are free from scale and oxide:

1. 1 part Nitric acid
2. 1 part Hydrofluoric acid, 48%
3. 1 part water

**WARNING:** Hydrofluoric acid is extremely hazardous to human health. It does not burn on contact with skin, and it can penetrate into ligaments and begin to ossify them. Due to a lack of proper hydrofluoric acid handling procedures, we used only a solution of nitric acid and water for this step. Rinse parts in tap water for 2 minutes.

After the above dip, repeat the Enbond cleaning step in the degreasing procedure, then rinse parts in tap water for 2 minutes.

Immerse parts in a 30% by volume solution of nitric acid for 2 minutes, then rinse in tap water for 2 minutes.

Immerse in MacDermid 629 Acid Dip (product of MacDermid Co., Waterbury, CT), 1lb/gallon of water, for 30 seconds; rinse in tap water for 2 minutes.

### B.2.3 Final Rinsing

Follow the final rinsing procedure for copper.

# Bibliography

[1] M. H. Anderson, J. R. Ensher, M. R. Matthews, C. E. Wieman, and E. A. Cornell. *Science* **269**, 198 (1995).

[2] K. B. Davis, M. O. Mewes, M. R. Andrews, N. J. vanDruten, D. S. Durfee, D. M. Kurn, and W. Ketterle. *Phys. Rev. Lett.* **75**, 3969 (1995).

[3] B. Verhaar, K. Gibble, and S. Chu. *Phys. Rev. A* **48**, R3429 (1993).

[4] E. Tiesinga, A. J. Moerdijk, B. J. Verhaar, and H. T. C. Stoof. *Phys. Rev. A* **46**, R1167 (1992); E. Tiesinga, B. J. Verhaar, and H. T. C. Stoof, *ibid.* **47**, 4114 (1993).

[5] A. Kastler. *J. Phys. Radium* **11**, 255 (1950).

[6] T. Hansch and A. Schawlow. *Opt. Commun.* **13**, 68 (1975).

[7] S. Chu, L. Hollberg, J. E. Bjorkholm, A. Cable, and A. Ashkin. *Phys. Rev. Lett.* 55, 48 (1985).

[8] H. Metcalf and P. van der Straten. *Phys. Rept.* 244, 203 (1994).

[9] C. Cohen-Tannoudji, J. Dupont-Roc, and G. Grynberg. *Atom-Photon Interactions: Basic Processes and Applications.* New York: John Wiley and Sons, 1992.

[10] J. Dalibard. Helsinki Workshop on Laser Manipulation of Atoms, unpublished.

[11] E. L. Raab, M. Prentiss, A. Cable, S. Chu, and D. Pritchard. *Phys. Rev. Lett.* 59, 2631 (1987).

[12] C. G. Townsend, N. H. Edwards, C. J. Cooper, K. P. Zetie, C. J. Foot, A. M. Steane, P. Szriftgiser, H. Perrin, and J. Dalibard. *Phys. Rev. A* **52**, 1423 (1995).

[13] P. Lett, R. Watts, C. Westbrook. W. PHillips, P. Gould, and H. Metcalf. *Phys. Rev. Lett.* **61**, 169, (1988).

[14] P. Ungar, D. Weiss, E. Riis, and S. Chu. *J. Opt. Soc. Am. B* **6**, 2058 (1989).

[15] J. Dalibard and C. Cohen-Tannoudji. *J. Opt. Soc. Am. B* **6**, 2023 (1989).

[16] J. Dalibard and C. Cohen-Tannoudji. *J. Opt. Soc. Am. B* **2**, 1707 (1985).

[17] J. Luiten. *Lyman-$\alpha$ Spectroscopy of Magnetically Trapped Atomic Hydrogen.* Doctoral thesis, University of Amsterdam, 1993, unpublished.

[18] W. Wing. *Prog. Quantum Electron.* **8**, 181 (1984).

[19] K. B. Davis, M. O. Mewes, M. A. Joffe, M. R. Andrews, and W. Ketterle. *Phys. Rev. Lett.* **74**, 5202 (1995).

[20] W. Petrich, M. H. Anderson, J. R. Ensher, and E. A. Cornell. *Phys. Rev. Lett.* **74**, 3352 (1995).

[21] T. Bergeman, G. Erez, and H. J. Metcalf. *Phys. Rev. A* **35**, 1535 (1987).

[22] D. J. Griffiths. *Introduction to Electrodynamics.* Englewood Cliffs: Prentice-Hall, 1981.

[23] O. J. Luiten, H. G. C. Werij, I. D. Setija, M. W. Reynolds, T. W. Hijmans, and J. T. M. Walraven. *Phys. Rev. Lett.* **70**, 544 (1993); J. M. Doyle, J. C. Sandberg, I. A. Yu, C. L. Cesar, D. Kleppner, and T. J. Greytak. *Phys. Rev. Lett.* **67**, 603 (1991), and references therein.

[24] K. Helmerson, A. Martin, and D. E. Pritchard. *J. Opt. Soc. Am. B* **9**, 483 (1992).

[25] C. J. Myatt, private communication.

[26] C. C. Bradley, C. A. Sackett, J. J. Tollet, and R. G. Hulet. *Phys. Rev. Lett.* **75**, 1687 (1995).

[27] C. Kittel, H. Kromer. *Thermal Physics.* New York: W. H. Freeman, 1980.

[28] P. A. Willems. Studies of Magneto-Optically and Magnetostatically Trapped Cesium in a Cryogenic Vacuum Apparatus. Doctoral thesis, California Institute of Technology, 1995, unpublished.

[29] J. J. Tollet, C. C. Bradley, C. A. Sackett, R. G. Hulet. *Phys. Rev. A* **51**, R22 (1995).

[30] G. K. White. *Experimental Techniques in Low-Temperature Physics.* Bristol: Oxford University Press, 1968.

[31] P. Kittel, A. L. Spivak, and L. J. Salerno. *Advances in Cryogenic Engineering* **37**, 241, 1992.

[32] Product of Yardley Products Corp., Yardley, Pennsylvania.

[33] R. P. Reed, A. F. Clark, eds. *Materials at Low Temperatures.* Metals Park: American Society for Metals, 1983.

[34] K. B. MacAdam, A. Steinbach, and C. Weiman. *Am. J. Phys.* **60**, 1098 (1992).

[35] K. G. Libbrecht and J. L. Hall. *Rev. Sci. Instrum.* **64**, 2133 (1993).

[36] O. Schmidt, K. M. Knaak, R. Wynands, and D. Meschede. *Appl. Phys. B* **59**, 167 (1994).

[37] J. L. Hall, L. Hollberg, T. Baer, and H. G. Robinson. *Appl. Phys. Lett.* **39**, 680 (1981).

[38] P. D. Lett *et al. J. Opt. Soc. Am.* B **6**, 2084 (1989).

[39] I. S. Gradshteyn and I. M. Ryzhik. *Table of Integrals, Series, and Products.* San Diego: Academic Press, 1994.

[40] W. H. Press, S. A. Teukolsky, W. T. Vetterling, and B. P. Flannery. *Numerical Recipes in C.* New York: Cambridge University Press, 1988.

[41] R. Vyas and S. Singh, *Phys. Rev. A* **45**, 8095 (1992).

[42] Z. Hu and H. J. Kimble, *Opt. Lett.* **19**, 1888 (1994).

[43] L. D. Landau and E. M. Lifshitz. *Quantum Mechanics.* Oxford: Pergamon Press, 1965.

[44] C. R. Monroe, E. A. Cornell, C. A. Sackett, C. J. Myatt, and C. E. Wieman. *Phys. Rev. Lett.* **70**, 414 (1993).

[45] C. R. Monroe. *Experiments with Optically and Magnetically Trapped Cesium Atoms.* Doctoral thesis, University of Colorado at Boulder, 1992, unpublished.

[46] C. Cohen-Tannoudji, B. Diu, and F. Laloe. *Quantum Mechanics.* New York: John Wiley and Sons, 1977.

[47] K. Tang, J. Norbeck, and P. Certain. *J. Chem. Phys.* **64**, 3063 (1976).

[48] H. F. Hess. *Phys. Rev. B* **34**, 3476 (1986).

[49] H. F. Hess, G. P. Kochanski, J. M. Doyle, N. Masuhara, D. Kleppner, and T. Greytak. *Phys. Rev. Lett.* **59**, 672 (1987).

[50] J. T. M. Walraven, in *Quantum Dynamics of Simple Systems*, Proceedings of the 44th Scottish Universities Summer School in Physics, 1994, Stirling, Scotland (1996).

[51] O. J. Luiten, M. W. Reynolds, and J. T. M. Walraven. *Phys. Rev. A* **53**, 381 (1996).

[52] D. L. Goodstein. *States of Matter.* New York: Dover, 1985.

[53] D. J. Griffiths. *Introduction to Elementary Particles.* New York: John Wiley and Sons, 1987.

[54] L. D. Landau and E. M. Lifshitz. *Statistical Physics.* Tarrytown: Elsevier, 1980.

[55] J. E. Bjorkholm. *Phys. Rev. A* **38**, 1599 (1988).

[56] W. Phillips and H. Metcalf. *Phys. Rev. Lett.* **48**, 596 (1982); J. Prodan, W. Phillips, and H. Metcalf. *Phys. Rev. Lett.* **49**, 1149 (1982).

[57] R. N. Watts and C. E. Wieman. *Opt. Lett.* **11**, 291 (1986).

[58] C. Salomon, J. Dalibard, W. D. Phillips, A. Clairon, and S. Guellati. *Europhys. Lett.* **12**, 683 (1990).

[59] D. Jin and C. Myatt, private communication.

[60] D. E. Pritchard, K. Helmerson, and A. G. Martin, in *Atomic Physics 11*, edited by S. Haroche, J. C. Gay, and G. Grynberg. Singapore: World Scientific, 1989.

[61] T. Hijmans, private communication.

[62] N. Sagna, G. Dudle, and P. Thomann. *J. Phys. B* **28**, 3213 (1995).

[63] P. A. Ruprecht, M. J. Holland, K. Burnett, and M. Edwards. *Phys. Rev. A* **51**, 4704 (1995); F. Dalfovo and S. Stringari, *Phys. Rev. A* **53**, 2477 (1996); Y. Kagan, G. V. Shlyapnikov, and J. T. M. Walraven, *Phys. Rev. Lett.* **76**, 2670 (1996).

[64] H. T. C. Stoof. *Phys. Rev. A* **49**, 3824 (1994).

[65] M. A. Joffe, W. Ketterle, A. Martin, and D. E. Pritchard. *J. Opt. Soc. Am. B* **10**, 2257 (1993).